

**Experimental investigation of inertial sphere, rod, and
disk particles in a turbulent boundary layer**

**A DISSERTATION
SUBMITTED TO THE FACULTY OF THE GRADUATE SCHOOL
OF THE UNIVERSITY OF MINNESOTA
BY**

Lucia J. Baker

**IN PARTIAL FULFILLMENT OF THE REQUIREMENTS
FOR THE DEGREE OF
DOCTOR OF PHILOSOPHY**

Filippo Coletti

June, 2021

© Lucia J. Baker 2021
ALL RIGHTS RESERVED

Acknowledgements

I am immensely grateful to the many people who supported me throughout my time in graduate school, without whom the work contained in this thesis would not have been possible. First and foremost, I want to thank my advisor, Dr. Filippo Coletti, without whom this research would not have happened. It has been a privilege working with Filippo, and I am extremely grateful for his mentorship, ideas, and energy. I credit him with instilling in me a passion for doing research, as well as helping me become a better scientist, experimenter, communicator, and problem-solver through our countless meetings, conversations, and brainstorming sessions. Thank you for giving me your support and guidance while encouraging me follow my own ideas, too.

I would also like to thank my committee members, Dr. Ellen Longmire, Dr. Krishnan Mahesh, and Dr. Michele Guala. They have taught me so much and given me valuable insight and feedback on my research.

I also want to express my gratitude to the many staff members at the University who were instrumental to this work: Molly Schmidt and Hanna Pahr for their administrative support, Kale Hedstrom for his assistance with lab hardware development and problem-solving, and Charles Nguyen and Dr. Evan Bollig for their advice on high-performance computing. In addition, I want to thank Dr. Jess Kozarek for her immense help in performing experiments in the Outdoor StreamLab, and Dr. Sina Ghaemi for his assistance with our non-Newtonian fluid-particle experiments.

I am incredibly grateful for the support of the exceptional individuals I have had as lab mates and classmates: Dr. Deepak Adhikari, Dr. Omid Amili, Dr. Diogo Barros, Dr. Tim Berk, Dr. Ankur Bordoloi, Dr. Doug Carter, Dr. Yanchong Duan, Dr. Kee Onn Fong, Dr. Roumaissa Hassaini, Dr. Sahar Jalal, Yinghui Li, Dr. Andras Nemes, Sagnik Paul, Dr. Alec Petersen, Merin Prince, Kurtis Rahkola, Henri Sanness

Salmon, Nick Sloan, Dr. Yan Ming Tan, Dr. Yi Hui Tee, Amy Tinklenberg, Tristan Van de Moortele, and Dr. Kyle Winters, as well as everyone in the Women in Aerospace group. Thank you for helping me in the lab and in classes, answering my questions, sharing equipment, and for giving me a sense of community and belonging in what can sometimes be an isolating endeavor. I am lucky to have known all of you.

I would also like to acknowledge my funding source, the National Defense Science and Engineering Graduate Fellowship, which gave me freedom to choose the direction of my research.

Finally, I am deeply grateful to my family who always supported and believed in me, and without whom I would not have made it to this point. Thank you to my partner, Dr. Kee Onn Fong, for your constant patience, encouragement, and support. And especially, thank you to my parents, Martha and Ken Baker, for always encouraging my curiosity and for supporting my education in every way.

Dedication

To my parents, Martha and Ken, for all their support, encouragement, and love.

Abstract

Turbulent, particle-laden flows are ubiquitous in nature and industry. Particles in many of these flows have finite size and inertia, which cause them to interact with the fluid turbulence in complex ways. They are also commonly non-spherical in shape, which adds further richness to the particle-fluid interplay. In this thesis, the dynamics of dilute, slightly negatively buoyant particles, fully suspended in a smooth-wall open channel flow, are investigated experimentally. Spheres, disks, and rods are studied in order to examine the effects of particle shape on their distribution and interaction with the fluid turbulence. The friction Reynolds number of the flow is $Re_\tau \sim 600$, and the particle Stokes number based on the friction velocity is $St^+ \sim O(10)$. Particle image velocimetry (PIV) and particle tracking velocimetry (PTV) are used to obtain simultaneous, time-resolved flow fields and particle trajectories. Their translational and rotational motion, as well as their concentration and dispersion, are investigated.

Disks and rods are both found to oversample high-speed fluid near the wall, in agreement with particle-resolved DNS studies. The spherical particle Reynolds stresses exceed those of the fluid due to particle trajectories crossing fluid streamlines; this effect is not observed for rods and disks. Spherical particle transport is strongly linked to ejections, while the role of sweeps is marginal, and there is no evidence of turbophoresis. The mean concentration profile of the spheres follows a power-law with a shallower slope than predicted by equilibrium theories that neglect particle inertia. However, rod and disk mean concentration profiles follow Rouse-Prandtl theory over a large portion of the boundary layer. Particle diffusivity is shown to be well-approximated by the fluid eddy diffusivity.

A detailed investigation of sphere behavior near the wall is carried out. Upward-/downward-moving particles display positive/negative mean streamwise acceleration due to the particle-fluid slip. The particles that contact the wall are faster than the local fluid both before reaching the wall and after leaving it. Therefore, they are decelerated by drag and pushed downward by shear-induced lift. The durations of wall contact follow exponential distributions with characteristic timescale close to the particle response time. Lift-offs coincide with particles meeting a fluid ejection. These

observations emphasize the competing effects of inertia and gravity.

The orientation and rotation of rod and disk particles are also measured. Rods tend to orient mostly in the streamwise direction, while disks strongly prefer to align their symmetry axis mostly normal to the wall. This alignment is much more stable for disks than for rods. Rods undergo strong tumbling near the wall and tend to tumble freely in response to the mean shear and turbulent fluid velocity fluctuations, whereas disks tend to wobble about their preferential wall-normal orientation, resulting in much weaker tumbling rates close to the wall. Wall contact is also implicated as a significant tumbling-inducing mechanism. Many of these results have not been previously confirmed experimentally.

Contents

Acknowledgements	i
Dedication	iii
Abstract	iv
List of Tables	viii
List of Figures	ix
1 Introduction	1
1.1 Spherical particles	1
1.2 Non-spherical particles	4
2 Experimental methods	10
2.1 Experimental facility	10
2.2 Particles	11
2.2.1 Spheres	11
2.2.2 Rods and Disks	15
2.3 Fluid velocity measurements	18
2.4 Particle detection and tracking	18
2.5 Particle orientation measurement	22
2.6 Measurement uncertainty	27
3 Results: spherical particles	30
3.1 Fluid and particle velocity	30

3.2	Slip velocity	33
3.3	Reynolds stresses	36
3.4	Quadrant analysis	38
3.5	Particle diffusion	41
3.6	Particle concentration and flux	43
3.7	Particle acceleration	46
3.8	Particle–wall interactions	50
4	Non-spherical particle results	60
4.1	Fluid and particle velocity and acceleration	60
4.1.1	Velocity statistics	60
4.1.2	Particle acceleration statistics	64
4.2	Particle orientation and tumbling	66
4.2.1	Orientation statistics	66
4.2.2	Statistics of tumbling rate and tumbling acceleration	67
4.2.3	Temporal coherence	71
4.2.4	Wall interactions	73
4.3	Particle spatial distribution and dispersion	76
4.3.1	Particle concentration profiles	76
4.3.2	Particle flux and diffusivity	78
5	Conclusions	81
5.1	Spheres	81
5.2	Rods and disks	84
	References	86

List of Tables

2.1	Properties of the PS particles	15
2.2	Properties of the rod and disk particles	16
2.3	Non-dimensional properties of the rod and disk particles	17
2.4	Imaging and PIV processing parameters	19
2.5	Orientation formulas	25
2.6	Bias uncertainties	28
3.1	Physical parameters of the water channel and boundary layer properties	31
4.1	Rouse numbers	77

List of Figures

2.1	Water channel diagram - sphere configuration	11
2.2	Water channel diagram - rod and disk configuration	12
2.3	Instantaneous realization of the particle laden flow	12
2.4	PS particle diameters	13
2.5	Kolmogorov scales	14
2.6	PS particle diameters	16
2.7	Kolmogorov scales - rods and disks	17
2.8	Particle detection - spheres	19
2.9	Instantaneous realizations - rods and disks	20
2.10	Particle detection - rods and disks	20
2.11	Streamwise acceleration variance as a function of smoothing kernel width	21
2.12	Particle orientation vector	22
2.13	Particle orientation vector	23
2.14	Orientation-dependent correction of apparent major axis length	24
2.15	Rod and disk trajectories	26
3.1	Mean streamwise velocity profile of the particle-laden and unladen fluid	32
3.2	Profiles of particle-laden and unladen Reynolds stresses	32
3.3	Wall-normal profiles of streamwise and wall-normal particle velocity . .	33
3.4	Wall-normal profiles of mean streamwise and wall-normal particle slip velocity	35
3.5	Profiles of mean instantaneous particle Reynolds number	36
3.6	Profiles of mean streamwise and wall-normal particle velocity conditioned on ascending and descending particles	37
3.7	Wall-normal profiles of the particle Reynolds stresses	38

3.8	Wall-normal profiles of the Reynolds shear stress of the fluid velocity at particle locations and the particle velocity, conditioned on ascending and descending particles	39
3.9	Joint PDFs of streamwise and wall-normal fluctuating fluid velocities . .	40
3.10	Lagrangian autocorrelations of streamwise and wall-normal particle velocity	42
3.11	Wall-normal profiles of streamwise and wall-normal diffusivity	44
3.12	Wall-normal profile of mean particle concentration	45
3.13	Wall-normal profile of particle streamwise mass flux	46
3.14	Profiles of mean streamwise and wall-normal particle acceleration	47
3.15	Wall-normal profiles of streamwise and wall-normal particle r.m.s. acceleration	49
3.16	PDFs of streamwise and wall-normal particle acceleration	50
3.17	Lagrangian autocorrelation of streamwise particle acceleration	51
3.18	An example of an interaction between a particle and the wall	52
3.19	PDF of duration of particle-wall interactions	53
3.20	PDF of the angle of trajectories for near-wall particles	54
3.21	Lagrangian means of particle wall-normal coordinate, streamwise velocity, and wall-normal velocity averaged over all identified touch-down events and lift-off events	55
3.22	Lagrangian means of streamwise and wall-normal fluid velocity at particle location averaged over all identified touch-down events and lift-off events	57
3.23	Lagrangian means of particle tangential acceleration and normal acceleration averaged over all identified touch-down events and lift-off events .	59
4.1	Mean velocity profiles of fluid and particles	61
4.2	Slip velocity profiles	62
4.3	Particle Reynolds stress profiles	63
4.4	Lagrangian autocorrelations of u_p and v_p	65
4.5	Particle acceleration profiles	66
4.6	PDFs of particle orientation components	67
4.7	Profiles of mean squared tumbling rate and mean square tumbling acceleration	68
4.8	Profiles of mean and RMS tumbling rate components	69

4.9	PDFs of particle squared tumbling rate and squared tumbling acceleration	69
4.10	PDFs of tumbling angular velocity components	70
4.11	PDFs of tumbling angular velocity components	71
4.12	Lagrangian autocorrelations of p_x and p_y	72
4.13	Lagrangian autocorrelations of $\omega_{t,z}$	73
4.14	PDFs of squared tumbling rate and acceleration within $D_p/2$ of the wall	74
4.15	PDFs of tumbling rate and acceleration components within $D_p/2$ of the wall	75
4.16	Profiles of mean particle concentration	77
4.17	Profiles of the particle flux terms	78
4.18	Profiles of fluid and particle diffusivities	80

Chapter 1

Introduction

1.1 Spherical particles

Particles in turbulent flows are ubiquitous in natural and industrial systems. A few examples of particle-laden turbulent systems include combustion engines, dust storms, rainclouds, sediment in rivers and coastal zones, and many manufacturing processes. Describing and predicting the behavior of inertial particles in turbulent boundary layers has been a major goal in fluid dynamics since the work of Shields (1936), Bagnold (1936), Rouse (1937), and Prandtl (1952), who first began quantifying the transport of sediment in air and water flows. The experiments of Shields (1936) revealed a relationship predicting the initiation of motion of the sediment from the particle inertia and the fluid shear stress on the wall. Bagnold (1936) observed the saltation of sand grains in air and developed an empirical relationship quantifying their flux as a function of the fluid flow parameters. Rouse (1937) analytically derived an expected concentration profile of suspended sediment as a function of wall-normal height, under equilibrium between turbulent resuspension and gravitational settling. Under the same assumption, Prandtl (1952) used a linear diffusivity model to derive a parabolic concentration profile which is still the de facto standard. These models are effective at describing the observed bulk transport properties but do little to shed light on the underlying physical mechanisms at the particle scale.

More recently, thanks to non-intrusive measurement techniques, several researchers used detailed experiments to further understand the interaction between the inertial

particles and the wall turbulence. Due to its relevance to sediment transport in water bodies, many studies in the geophysical research literature focused on the case in which the suspension is eroded from and deposited to a bed of particles. For example, Hurther & Lemmin (2003) investigated the transport of suspended particles in a turbulent open channel flow by comparing statistics of particle mass flux with turbulent momentum flux and concluded that coherent structures are a dominant mechanism of particle transport. Lajeunesse *et al.* (2010) used imaging to investigate the relation between the flow turbulence and the intermittent motions of the particles alternating rest and flight. Heyman *et al.* (2016) empirically determined closure equations for particle bed load transport in terms of known flow conditions, such as particle diffusivity and suspension/deposition rates.

The presence of a changing wall roughness and the mobilization of a polydisperse bed complicate the task of isolating the particle-fluid dynamics. Somewhat surprisingly, the smooth-wall case has been considered in a limited number of experimental studies. Kaftori *et al.* (1995*a*) measured velocity and concentration profiles of sub-millimeter polystyrene particles in a horizontal water flume and found that particles preferentially concentrate in regions of low fluid velocity associated with near-wall streaks. Niño & Garcia (1996) confirmed that particles in a smooth-wall flume arranged themselves in long streaks generated by streamwise vortices in the inner layer. Tanière *et al.* (1997) looked at solid particles in a wind tunnel and reported large fluctuations of the dispersed phase velocity, attributing them to saltation at the wall. Kiger & Pan (2002) found evidence that particles congregate in specific structures in the turbulent boundary layer, and showed a difference between ascending and descending particles: upward-moving particles were concentrated in ejections (events with negative streamwise fluctuation and positive wall-normal fluctuation of the fluid velocity); whereas downward-moving particles showed a weaker association to sweeps (events with positive streamwise fluctuation and negative wall-normal fluctuation). This was later confirmed by detailed time-resolved measurements, e.g., van Hout (2011, 2013); Rabencov *et al.* (2014). Righetti & Romano (2004) studied glass particles in water at a volume fraction of 10^{-3} and observed significant modulation of the fluid turbulence, which they attributed to the inter-phase momentum exchange during entrainment from and deposition to the wall.

Gerashchenko *et al.* (2008) measured the acceleration of inertial particles in a turbulent boundary layer and found that acceleration variance increased with particle inertia, contrary to what happens in isotropic turbulence (Bec *et al.*, 2006). Ebrahimian *et al.* (2019) investigated in detail the particle acceleration and its relation to turbulent events and showed that particles may slide along the wall for considerable time. Tee *et al.* (2020) performed detailed, three-dimensional measurements on a single large spherical particle interacting with the wall in a turbulent boundary layer and found that spheres underwent minimal rotation while lifting off the wall, and that spanwise forces on the particles can be important. Berk & Coletti (2020) considered microscopic glass beads in a wind tunnel. They highlighted how the particle inertia is responsible for discrepancies from the concentration profile predicted by the Rouse–Prandtl theory (Rouse, 1937; Prandtl, 1952), and investigated the roots of the relative particle-fluid velocity. Due to the limited accuracy in locating the small particles, they could not measure the settling velocity, which is known to be strongly altered by turbulence (Wang & Maxey, 1993; Nielsen, 1993; Sabban & van Hout, 2011; Petersen *et al.*, 2019).

The numerical studies of inertial particles in smooth-wall turbulence have been much more numerous and have allowed in-depth analysis of the problem, especially using direct numerical simulation of the fluid flow coupled with advection of point-particles, e.g., Rouson & Eaton (2001); Marchioli & Soldati (2002); Zhao *et al.* (2010); Zamansky *et al.* (2011); Sardina *et al.* (2012); Bernardini (2014); Richter & Sullivan (2014); Lee & Lee (2015). Typically, a simplified version of the particle transport equation was used, which is only valid in the limit of vanishingly small particle Reynolds number (Maxey & Riley, 1983). Also, in the majority of these cases (included the ones mentioned above) gravity was neglected; this isolates the effect of particle inertia but prevents the direct application of the results to practical settings. The few studies that considered wall-normal gravity (among others, Lavezzo *et al.*, 2010; Lee & Lee, 2019) underscored its importance and interplay with the mean shear. In particular, Lee & Lee (2019) indicated that gravity greatly reduced turbophoresis, i.e., the tendency of the particles to drift down the gradient of Reynolds stresses (hence towards the wall) due to the interaction with streamwise vortices (Marchioli & Soldati, 2002).

The limitations of the point-particle approach may be exacerbated in particle-laden turbulent boundary layers where wall-normal gravity is important: the assumption of

negligible particle-size effects is particularly limiting near the wall, where the flow scales are the smallest and the number density the highest. Forces which are normally considered negligible for microscopic particles (e.g., added mass, Saffman and Magnus lift; see Crowe *et al.* (2011)) may be important, and advanced methods are especially needed to account for the flow distortion by the particles. While effective point-particle strategies to address the latter issue have recently been proposed (Capecelatro & Desjardins, 2013; Gualtieri *et al.*, 2015; Horwitz & Mani, 2016; Ireland & Desjardins, 2017; Balachandar *et al.*, 2019), numerical advances and ever-growing computational resources have enabled particle-resolved direct numerical simulations (Kidanemariam *et al.*, 2013; Picano *et al.*, 2015; Lin *et al.*, 2017; Wang *et al.*, 2017). Still, these studies are mostly limited to small Reynolds numbers and relatively large particles. Importantly, it is hard to validate these simulations against the scarce experimental studies focused on the detailed particle-wall-fluid dynamics, especially considering that most of the experimental literature is concerned with geophysical flows including particle polydispersity, bed roughness, and mobile beds.

In this thesis we consider the fundamental case of highly dilute, mono-dispersed, spherical particles suspended by a turbulent boundary layer over a horizontal smooth wall, where particles interact with the wall but do not deposit on it. We perform laboratory experiments and leverage simultaneous time-resolved imaging of both phases to explore the details of the particle-fluid interaction across the boundary layer.

1.2 Non-spherical particles

Particle-laden turbulence studies have often considered spherical particles, treating them as an idealized case for particles with compact geometries. However, systems in which particles are non-spherical and extended in one or more dimensions are myriad: for example, paper-making pulp consists of suspensions of fibers; microplastics are often fibers or flat fragments; diatoms take rotationally-symmetric prolate or oblate shapes; ice crystals in atmospheric clouds are often disk-like. In addition, even in applications where particles are treated as spheres, there is often a distribution of shapes present in the real particles, which can include particles that differ significantly from spherical.

Anisotropic particle dynamics differ from spherical particle dynamics in a few key respects: their drag coefficient is dependent on their orientation, resulting in a resistance tensor rather than a drag vector acting on particles, and they are subject to different torques than spherical particles, resulting in more complex modes of solid-body rotation. Modulated by the instantaneous orientation of the particle, the drag and torque components feed back on each other, resulting in rich and complex translational and rotational particle motion in turbulent flows.

Because of this richness, the behavior of anisotropic particles is less well understood than that of spheres. In addition to the complexity of the dynamics, there are additional challenges in experimentally or numerically studying anisotropic particles. Many simulations rely on point-particle models due to computational constraints, losing some fidelity in the simulation; those that fully resolve the particle boundary gain fidelity, but are constrained by limitations on the particle count or the Reynolds number of the flow. Experimentally measuring anisotropic particle kinematics is difficult due to the 3D nature of the system. Experimental studies typically either use planar imaging experiments which capture 2D projections of the particles, or tomographic or holographic set-ups which capture the particle behavior in 3D. Both types of imaging can typically only capture tumbling motion, i.e., the rotation of the particle symmetry axis, and lack the ability to measure particle spin about the symmetry axis, except in special cases where different points on the particle can be marked. In addition, particle and fluid inertia complicate their interactions. The motion of ellipsoidal particles (i.e., those that possess an axis of rotational symmetry) is mostly controlled by three parameters: fluid inertia, particle inertia, and particle aspect ratio. The inertia of a fluid flow is quantified with the Reynolds number, $Re = UL/\nu$, where U is the fluid velocity scale, L is a length scale characterizing the fluid flow, and ν is the fluid kinematic viscosity. Particle inertia is quantified with the Stokes number $St = \tau_p/\tau_f$, where τ_p is the response time of the particle and τ_f is a characteristic time scale of the flow. Finally, the particle aspect ratio of axisymmetric particles is defined as $\lambda = a/b$, where a is the length of particle's axis of rotational symmetry, and b is the length of the perpendicular axes. Prolate (rod-like) particles have $\lambda > 1$; oblate (disk-like) particles have $\lambda < 1$.

The study of anisotropic particles in fluid flows was pioneered by Jeffery (1922), who derived an analytical prediction for inertia-less (tracer) elliptical particle rotation in

laminar 2D simple shear flow and concluded that their motion is completely determined by their aspect ratio, λ . This was followed by Taylor (1923), who experimentally verified Jeffery’s predictions. Bretherton (1962) later generalized these so-called Jeffery orbits to any rigid body of rotation. Jeffery orbits only describe particle motion for negligible St and Re , however. Significant work has been done over the past two decades on inertial particles in fully turbulent flows, which is summarized in the review by Voth & Soldati (2017). Some of the key literature most relevant to our experiment is summarized in the following.

Point-particle simulations have frequently been used to understand many aspects of anisotropic particle-laden flows due to the relative simplicity of the models. The orientation and modes of rotation are found by point-particle simulations to depend on particle inertia, aspect ratio, and whether they are in proximity to a wall. Marchioli *et al.* (2010) studied orientation, distribution, and deposition of inertial fibers in channel flow and found that the fibers have a preferred, but unstable, streamwise orientation. Zhao *et al.* (2015) explored particle rotation rates as a function of St and λ . They found that modes of rotation depend strongly on both variables: in the high-shear, near-wall region, low- St disks tend to align orthogonal to the local fluid vorticity vector, and high- St disks align parallel with it, resulting in a tumbling mode of rotation for low- St disks and a spinning mode for high- St disks. On the other hand, the orientation and rotation of rods became more isotropic with increasing inertia. This study was extended by Zhao *et al.* (2019), who examined covariances between particle orientation \mathbf{p} (i.e., the unit vector parallel to the symmetry axis of the ellipsoid), particle rotation $\boldsymbol{\omega}$ and fluid rotation $\boldsymbol{\Omega}$. They determined that the co-variance between \mathbf{p} and $\boldsymbol{\omega}$ tends to explain the mode of rotation, e.g. spinning versus tumbling, while the co-variance between \mathbf{p} and $\boldsymbol{\Omega}$ primarily contributes to the rotation rate. The orientation and rotation of inertial disk particles in wall turbulence was explored by Challabotla *et al.* (2015), who showed that disk λ has only minor effects on particle translation motion, especially for high St . For low St particles, orientation as well as spin showed a strong dependence on λ in the near-wall region. The flattest particles were unable to achieve a rotation rate comparable to that of the fluid, which was attributed to their high rotational inertia. Inertial disks were found to preferentially align with the vorticity vector (oriented spanwise on average), producing significant spinning. Simulations of inertial fiber orientation in turbulent

channel flow were performed by Njobuenwu & Fairweather (2016), finding that long fibers align themselves parallel to the flow direction, and orthogonal to the vorticity and flow velocity gradient directions.

The dynamics and mechanisms of particle rotation and preferential orientation have been studied as well. Ni *et al.* (2015) performed measurements of the coupling between the tumbling of rods and the velocity gradient tensor in turbulence, determining that rods preferentially align with the extensional eigenvector of the velocity gradient tensor, which itself is usually (but not always) aligned with the vorticity vector. Marchioli *et al.* (2016) investigated the relative rotational motion between rigid fibers and fluid in turbulent channel flow and found that fiber rotation lags fluid rotation, except due to history effects for very high- St particles. For $St \sim 0$, slip spin does not go to zero because fluid strain contributes to fiber rotation. Fibers also tend to spin relative to the fluid when entrained in turbulent sweep/ejection events. The dynamics of disk-like particles in turbulent vertical channel flow were investigated by Yuan *et al.* (2017). They found that particle velocity fluctuations are mostly dependent on particle inertia, and depend very little on particle shape or gravity; the presence of gravity also has a negligible effect on the disks' orientation and rotation. Ouchene *et al.* (2018) studied the acceleration statistics of prolate spheroidal particles in turbulent channel flow and found that, as with spheres, particle acceleration RMS decreases with increasing inertia, and showed from particle acceleration autocorrelations that a global St is inappropriate, as the zero-crossing time of the autocorrelations increases with increasing distance from the wall.

The deposition and wall-normal flux of nonspherical particles has also been investigated by point-particle simulations. Marchioli *et al.* (2010) found that coupling between the translation motion and the rotational motion of elongated fibers changes their wall-ward flux significantly by changing the mean fiber wall-normal velocity. This effect adds to that due to their inertia and, compared to the case of spherical particles, modifies the build-up of fibers at the wall and their deposition rates. Yuan *et al.* (2018a) used Voronoi analysis to study the preferential concentration of spheroidal particles in wall turbulence and found that particle flux towards the wall is primarily influenced by particle inertia. Intermediate λ enhanced drift towards the wall for the most inertial particles, while particles with the most extreme λ exhibited the most even distribution

across the channel. Yuan *et al.* (2018b) then found that inertial spheroids moving toward or away from the channel walls tend to correlate with sweeps and with ejections, respectively, which supports the interpretation that sweeps and ejections are the mechanisms by which inertial particles are carried toward the wall and re-entrained into the outer flow.

Particle-resolved direct numerical simulations (PR-DNS) have been employed to obtain a more accurate understanding of the effects of finite particle size and inertia on their dynamics. Several of the above point-particle studies find that ellipsoidal particles accumulate in low-speed streaks near the wall; however, this finding has been called into question by PR-DNS studies. Do-Quang *et al.* (2014) used PR-DNS to simulate finite-size fibers in a turbulent channel flow and found that particles congregate in high-speed streaks near the wall rather than in low-speed streaks. They explained that when finite-size fibers move towards the wall in turbulent sweeps, contact forces with the wall hinder the fibers from passively following the fluid towards low-speed flow regions and tend to keep them in high-speed flow regions. Eshghinejadfard *et al.* (2017) performed PR-DNS of prolate spheroids in turbulent channel flows without gravity. They found that although spheres show a local peak of volume fraction near the wall, this is not the case for spheroids; local volume fraction of spheroids increases gradually before reaching a plateau far from the wall. Spheroids show a preferential alignment along the streamwise direction, which is stronger close to the walls and increases with particle aspect ratio. They infer that tumbling (off-axis rotation), as opposed to spinning (along-axis rotation), is the most frequent rotation mode of spheroids near the wall. Wang *et al.* (2018) studied the effects of particle shape and inertia on the transport of finite-size particles in a turbulent Couette flow. The symmetry axis of their oblate particles is almost parallel to the wall-normal direction and the major axis of prolate particles tends to align in the flow direction. Near the walls, the particles rotate predominantly along the spanwise direction due to the mean shear.

Finally, a small number of experiments have been performed in this regime. Earlier experimental work focused on particle orientation Bernstein & Shapiro (1994) and deposition Zhang *et al.* (2001) in laminar flows. Experiments on inertial anisotropic particles in turbulent shear flows are scarce. van Hout (2013) presented a method using a combination of planar PIV and two-orthogonal-view holography in fiber suspension flows to

experimentally measure 3D fiber orientation and the 2D fluid velocity field surrounding the particle. Shaik *et al.* (2020) then performed measurements of length effects on the dynamics of rigid fibers in a turbulent channel flow using this holography technique. They found that fibers accumulate in high-speed streaks, but lagged the fluid farther from the wall due to increased drag. Although these authors did not directly measure the fluid velocity fields, longer fibers were inferred to interact more frequently with large, energetic turbulent structures, resulting in increased probabilities of extreme transverse and wall-normal velocities. Longer fibers were also found to tumble significantly more strongly than shorter fibers.

From this review, it is clear that many open questions remain in understanding the behavior of inertial anisotropic particles in turbulence which can be addressed through experimental measurements, including: do inertial prolate and oblate particles accumulate in low-speed or high-speed streaks? What are their relative rates and axes of tumbling motion? How do the concentration and wall-normal flux of anisotropic particles compare to those of spheres? In order to address these gaps, we consider a dilute suspension of rod and disk particles fully suspended in a turbulent horizontal boundary layer, with $St \sim O(10)$ and major axis dimensions D_p much larger than the Kolmogorov and viscous length scales of the flow. Laboratory measurements are performed to measure simultaneous fluid velocity fields and particle position, velocity, acceleration, orientation, and tumbling rate.

This thesis is organized as follows: the experimental facility and data processing methods are described in Chapter 2; results and discussion for the spherical particles are presented in Chapter 3; results and discussion for the non-spherical particles are presented in Chapter 4 and conclusions are summarized in Chapter 5.

Chapter 2

Experimental methods

2.1 Experimental facility

A recirculating open channel with water as the working fluid is used for this experiment. The channel walls and floor are made of transparent acrylic. The channel width is 15 cm, with the water filled to a depth $H = 15$ cm. Guide vanes are placed in each of the four corners to reduce secondary flows produced at the turns. The test section is located 1.4 m downstream of a corner, allowing the flow to reach a developed state, which was verified by comparing fluid velocity statistics from the upstream and downstream ends of the test section. A diagram of the channel is shown with the configuration for the spherical particle experiment (figure 2.1) and its configuration for the rod and disk particle experiment (figure 2.2). The flow is provided by a paddlewheel with 16 paddles driven by a 1/4 HP permanent magnet motor (Leeson, USA) at a constant angular speed of 10 revolutions per minute. This is used instead of a centrifugal pump to avoid damaging the particles and the pump. In the spherical particle experiment, two wire screens with a grid spacing of 4 mm and one honeycomb with a cell size of 7 mm and a depth of 25 mm are placed upstream of the test section, as shown in figure 2.1. In the non-spherical particle experiment, due to the large size of the particles, two 3D-printed grids are used for flow conditioning instead of the screens and honeycombs, each with a streamwise depth of 250 mm. The first has a cell size of 40 mm and is placed downstream of the first bend after the paddlewheel to dampen swirl and large flow structures from the paddles; the second has a cell size of 30 mm and is positioned upstream of the

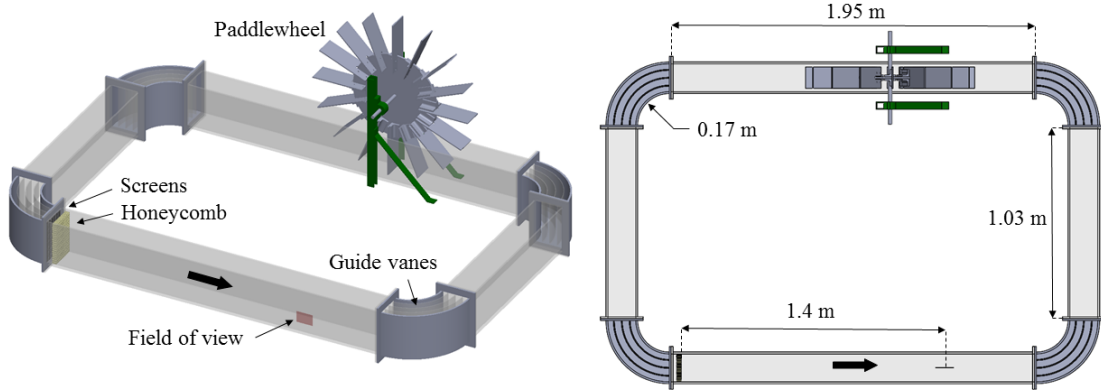


Figure 2.1: Diagram of the water channel configured for the spherical particle experiment, showing key components and dimensions. The bold arrow indicates the direction of the flow.

test section, as shown in figure 2.2. The large cell sizes are necessary to avoid the disk and rod particles becoming stuck and blocking the flow. In the sphere configuration, the freestream velocity is 0.42 m/s, which is measured to be constant in time within experimental uncertainty. The rod and disk configuration results in a freestream flow velocity of 0.43 m/s due to the slightly lower pressure drop through the coarser flow conditioning.

2.2 Particles

2.2.1 Spheres

Spherical polystyrene (PS) particles (Composition Materials Co., USA) are used. The particles are transparent, but their index of refraction causes significant scattering of the illumination light, and they appear as shown in figure 2.3. Because polystyrene is hydrophobic, the particles are first mixed in a dilute solution of water and a surfactant (dish soap) before introducing them into the channel to allow them to disperse.

The physical properties of the particles are listed in table 2.1. The diameter D_p is measured by imaging about 230 particles placed on a tray in a single layer. Their detection and sizing are performed via a circle-finding function based on the Hough

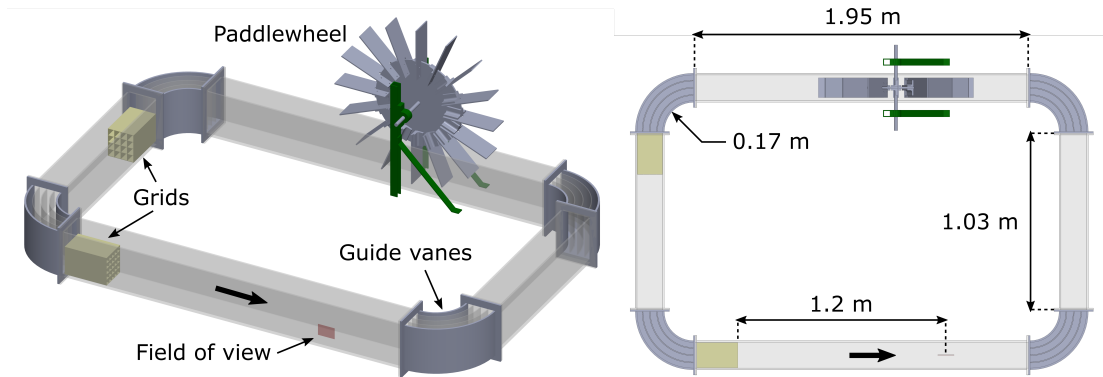


Figure 2.2: Diagram of the water channel configured for the non-spherical particle experiment, showing key components and dimensions. The bold arrow indicates the direction of the flow.



Figure 2.3: Instantaneous realization of the particle laden flow. Both the mm-sized spherical PS particles and the microscopic silver-coated glass tracer particles are visible.

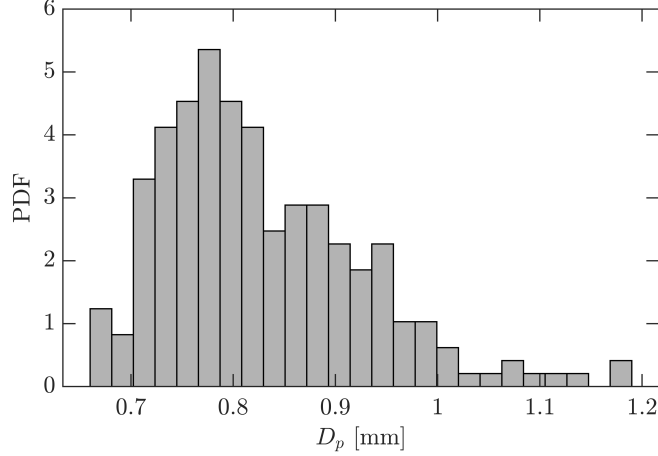


Figure 2.4: Probability density function of PS particle diameters. The standard deviation is 12% of the mean value.

transform. The probability density function (PDF) of the particle diameters is plotted in figure 2.4. For completeness, we also report the value of the Galileo number $Ga = [(\rho_p/\rho_f - 1)gD_p^3/\nu^2]^{1/2}$ and the Shields number $Sh = u_\tau^2/[(\rho_p/\rho_f - 1)gD_p]$. These indicate that the effect of gravity is significant (as also indicated by the ratio V_t/u_τ , of order one), although the particles are in a continuous transport (full suspension) regime.

The terminal velocity V_t is measured by dropping individual particles from rest in a large tank of quiescent water and recording 60 frame-per-second (fps) videos. Particles are tracked using the same method used for the particle-laden flow measurements, which will be described in the next section. The tank is deep enough (0.3 m) for the particles to reach a steady-state velocity before touching the bottom. The nominal particle Reynolds number is computed based on the terminal velocity, $Re_{p,V_t} = \rho_f V_t D_p / \mu$, where ρ_f and $\mu = \rho_f \nu$ are the water density and dynamic viscosity, respectively. This Reynolds number is used to correct the Stokes drag coefficient according to the Schiller & Naumann correction (Clift *et al.*, 2005), which in turn is used to estimate the particle density ρ_p from the measured terminal velocity.

To quantify particle inertia, we refer to the Stokes number, i.e., the ratio between the particle response time and a relevant fluid time scale. As for the particle response time, we consider the characteristic time scale with which the particle exponentially approaches the steady state velocity of the surrounding fluid, $\tau_p = \rho_p D_p^2 / (18\mu)$. We

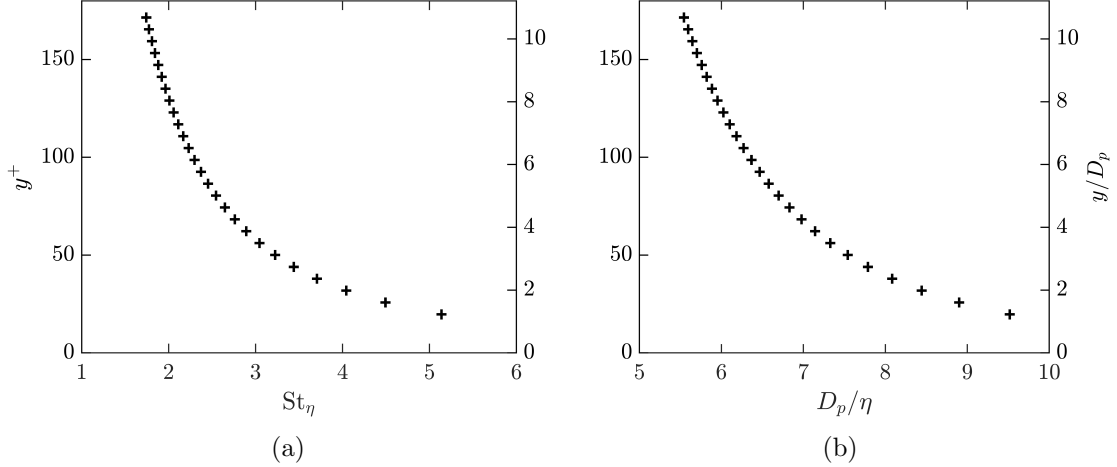


Figure 2.5: Wall-normal profiles of (a) the particle Stokes number based on the Kolmogorov scale and (b) the particle diameter normalized by the Kolmogorov scale.

favour this definition over the other commonly used response time, $(\rho_p - \rho_f)D_p^2/(18\mu)$, which describes the exponential approach to terminal velocity of a particle settling in a still fluid. As for the fluid, both the viscous time scale τ^+ and the Kolmogorov time scale τ_η are relevant. τ^+ is based on the friction velocity u_τ , estimated from fitting the log-law to the measured velocity profile (see §3.1), from which we define $St^+ = \tau_p/\tau^+$ (the superscript ‘+’ denoting, here and in the following, normalization by wall units). τ_η varies with the wall normal distance and is estimated from the production-dissipation balance in the turbulent boundary layer (Pope, 2000). This gives a range for the Stokes number $St_\eta = \tau_p/\tau_\eta$ and for the ratio of particle diameter to Kolmogorov length D_p/η , both reported in figure 2.5.

The volume fraction of the particles in the system, Φ_v , is about 10^{-4} . Thus, at the present particle-to-fluid density ratio, the momentum two-way coupling effects are expected to be localized and have a minimal impact on the fluid statistics. This is verified in §3.1 by showing that the unladen and laden fluid velocity profiles overlap within experimental uncertainty.

D_p (mm)	D_p^+	ρ_p (kg/m ²)	V_t (mm/s)	V_t/u_τ	Re_{p,V_t}	τ_p (ms)	St^+	Ga	Sh
0.83	16	1018.6	13.9	0.75	13	43.3	15	11.3	2.0

Table 2.1: Properties of the PS particles. D_p is the mean particle diameter, D_p^+ is the diameter normalized by the viscous length scale of the flow, ρ_p is the density, V_t is the terminal velocity in still water, Re_{p,V_t} is the Reynolds number based on V_t , τ_p is the particle response time, St^+ is the particle Stokes number based on the viscous time scale of the flow, Ga is the Galileo number, and Sh is the Shields number.

2.2.2 Rods and Disks

Disk particles with a nominal diameter of 2 mm and rod particles with a nominal length of 3 mm are also used in the experiments. Circular, white-colored glitter (Etsy.com) is used for disks. Rods are produced by cutting lengths of translucent white, non-elastic beading wire (Beadalon) to size. Both rods and disks are stiff enough to be practically rigid in the water flow. Because the particles are hydrophobic, they are first mixed in a dilute solution of water and a surfactant (dish soap) before introducing them into the channel to allow them to disperse.

The key physical properties of the three particle types are summarized in table 2.2. Because the disks are die-cut, there is no measurable scatter in their diameter. However, there is more scatter in the lengths of the rods because they are manually cut. Their lengths are measured by imaging about 200 particles placed on a tray in a single layer; they are then sized from the images using an automated intensity-threshold-based detection method. The probability density function (PDF) of the rod lengths is plotted in figure 2.6. In the following, the major axis lengths of particles (i.e., the disk diameter and the rod length, as well as the sphere diameter) will be denoted by D_p .

The terminal velocity V_t of the disks and rods is measured by dropping individual particles from rest in a large tank of quiescent water and recording 60 fps videos. Particles are tracked using the same threshold-based method as is used for the particle sizing (see section 2.4). The tank is deep enough (0.3 m) for the particles to reach a steady-state velocity before touching the bottom. The nominal particle Reynolds number is then computed based on the terminal velocity, $Re_{p,V_t} = \rho_f V_t D_{p,eq} / \mu$, where ρ_f and $\mu = \rho_f \nu$ are the water density and dynamic viscosity, respectively, and $D_{p,eq}$ is the particle's equivalent diameter, i.e., the diameter of a sphere with the same volume as

Particle type	a (mm)	b (mm)	Material	ρ_p (kg/m ³)	V_t (mm/s)
Spheres	0.84	–	Polystyrene	1018.6	13.9
Rods	2.9	0.25	Nylon	1150	10.5
Disks	0.088	2.0	PET	1380	13.5

Table 2.2: Properties of the non-spherical particle types used in the experiment compared with the sphere properties: a , the mean length of the particle axis of rotational symmetry; b , the mean length of the other two axes; the particle material; ρ_p , the material density; and V_t , the terminal velocity.

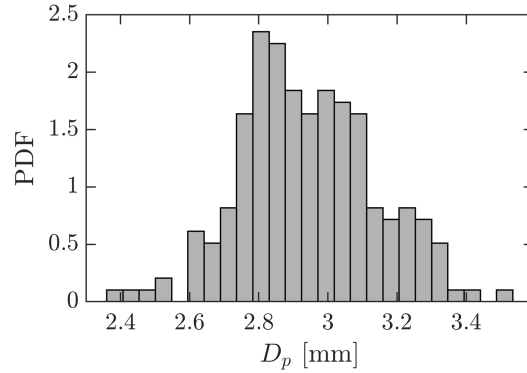


Figure 2.6: Probability density function of the rod lengths. The standard deviation is 7% of the mean value.

the disk or rod particle.

In the case of anisotropic particles, the estimation of the particle response time and Stokes number is more complex than for spheres. An expression for the response time of prolate spheroids is given by Shapiro & Goldenberg (1993) as

$$\tau_p = \frac{2}{9} \frac{\rho_p (b/2)^2}{\mu} \frac{\lambda \ln(\lambda + (\lambda^2 - 1)^{1/2})}{(\lambda^2 - 1)^{1/2}}. \quad (2.1)$$

For oblate spheroids, the response time is given by

$$\tau_p = \frac{2}{9} \frac{\rho_p (b/2)^2}{\mu} \frac{\lambda [\pi - 2 \tan^{-1}(\lambda(1 - \lambda^2)^{-1/2})]}{2(\lambda^2 - 1)^{-1/2}} \quad (2.2)$$

(Zhao *et al.*, 2015). Both of these formulas are derived for particles with an isotropic orientation distribution; this is generally not the case in anisotropic shear flows, but

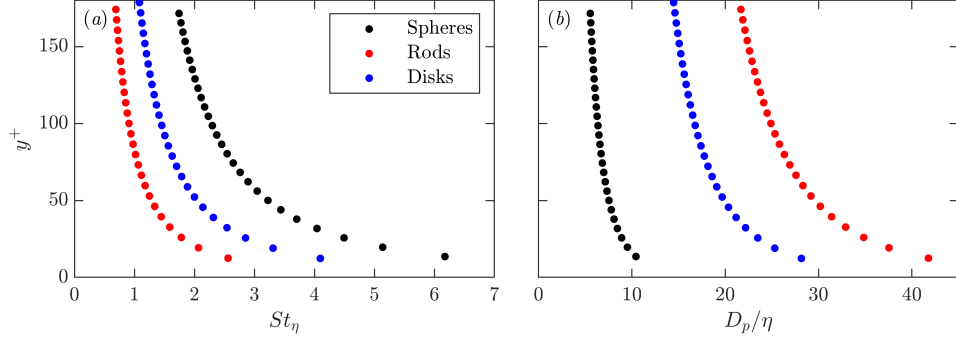


Figure 2.7: Wall-normal profiles of (a) the particle Stokes numbers based on the Kolmogorov scale and (b) the particle major axis lengths normalized by the Kolmogorov scale.

Particle type	D_p^+	λ	ρ_p/ρ_f	V_t/u_τ	Re_{p,V_t}	St^+
Spheres	16	1	1.02	0.75	13	15
Rods	66	11.8	1.15	0.52	8	6
Disks	45	0.044	1.38	0.67	12	11

Table 2.3: Properties of the particles. D_p^+ is the mean particle major axis length in viscous units, λ is the aspect ratio, ρ_p/ρ_f is the particle-to-fluid density ratio, V_t is the terminal velocity in still water, Re_{p,V_t} is the Reynolds number based on V_t and the particle equivalent diameter, and St^+ is the particle Stokes number based on the viscous time scale of the flow.

these formulas can be considered a nominal estimate. In addition, the Kolmogorov Stokes number $St_\eta = \tau_p/\tau_\eta$ and the ratio of particle major axis length to Kolmogorov length D_p/η are both reported in figure 2.7, compared to those of the spheres.

The volume fraction of the particles in the system is about 10^{-4} . Thus, at the present particle-to-fluid density ratio, the momentum two-way coupling effects are expected to be localized and have a minimal impact on the fluid statistics. The physical properties of the particles are summarized in table 2.3.

2.3 Fluid velocity measurements

Time-resolved planar particle image velocimetry (PIV) is used to measure the velocity of the fluid. The water is seeded with 13-micron silver-coated glass bubbles (Potters Industries) to act as tracers. A 300 W near-infrared pulsed laser with a wavelength of 808 nm (Oxford Lasers, Firefly 300W) is used for illumination. The laser is positioned above the channel and emits a 1 mm light sheet perpendicular to the floor and parallel to the streamwise direction, illuminating the channel symmetry plane. A 15 cm square acrylic plate is fixed at the water surface to avoid distortion of the laser sheet. This results in a shear layer below the plate less than 1 cm deep, which does not affect our region of interest. Images are captured with a high-speed, 4-megapixel CMOS camera (Phantom VEO 640L) viewing through one of the side walls. The camera mounts a 105 mm lens, capturing the bottom 6 cm of the channel. For optimal tracking, a frame rate of 500 Hz is chosen to obtain typical displacements of about one particle diameter (approximately 20 pixels). The recording time amounts to about 1900 boundary-layer turnover times.

The image processing routine is similar to what is described in Petersen *et al.* (2019). First the particles are identified (using the method described in §2.4) and substituted with Gaussian noise having the same mean and standard deviation as the background image. The resulting tracer-only images are used for PIV processing performed with a custom-written software. A minimum-intensity background subtraction is then performed which removes consistent bright spots caused by reflections and glare off the wall. Multi-pass cross-correlation with an overlap of 75% between interrogation windows is used to compute fluid displacement fields. Initial, intermediate, and final interrogation window sizes of 128^2 , 64^2 , and 32^2 pixels are used, respectively. A signal-to-noise ratio criterion and a universal outlier detection (Westerweel & Scarano, 2005) are used to reject spurious velocity vectors. The imaging and PIV processing parameters are summarized in table 2.4.

2.4 Particle detection and tracking

To locate the spherical particles, a convolution method using a particle template image is used, similar to van Hout *et al.* (2013) (figure 2.8). First, a low-pass median filter

f_s (Hz)	N	w (mm)	h (mm)	w_i (mm, wall units)	δx (mm, wall units)
500	65 700	95	63	1.26, 24.3 ⁺	0.31, 6.1 ⁺

Table 2.4: Imaging and PIV processing parameters: f_s is the imaging frequency; N is the number of images; w and h are the field of view width and height, respectively; w_i is the final-pass PIV interrogation window size; and δx is the PIV vector spacing.

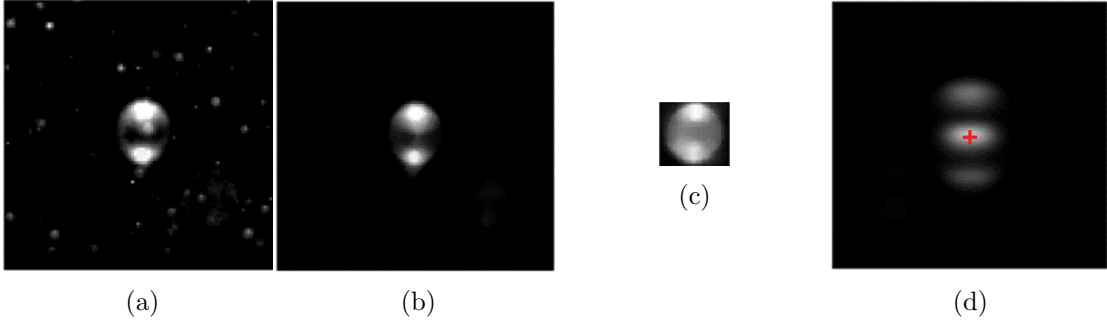


Figure 2.8: Convolution method for particle detection: (a) original image, (b) median filtered image, (c) particle template image to be convolved with the filtered image, and (d) convolution peak, the red cross indicating the detected particle centroid.

with a width of nine pixels is applied to the original images (figure 2.8a) to remove the tracers (figure 2.8b). Then, images are convolved with a particle template image (figure 2.8c). The particle centroids are then identified as convolution peaks which surpass a specified threshold (figure 2.8d), whose exact value is verified to have negligible impact on the results.

The disk and rod particles have good contrast with the background (figure 2.9), allowing detection using an image segmentation method based the particles' intensity (figure 2.10). First, a low-pass median filter with a width of nine pixels is applied to the original images to remove the tracers (figure 2.10a, d). Then, images are segmented into inertial particles and background based on an intensity threshold (figure 2.10b, e). Because the particles generally have strong contrast with the background, the detection was not sensitive to the exact value of the intensity threshold. The centroids of the particles are then located by computing the centroid of the identified particle image (figure 2.10c, f).

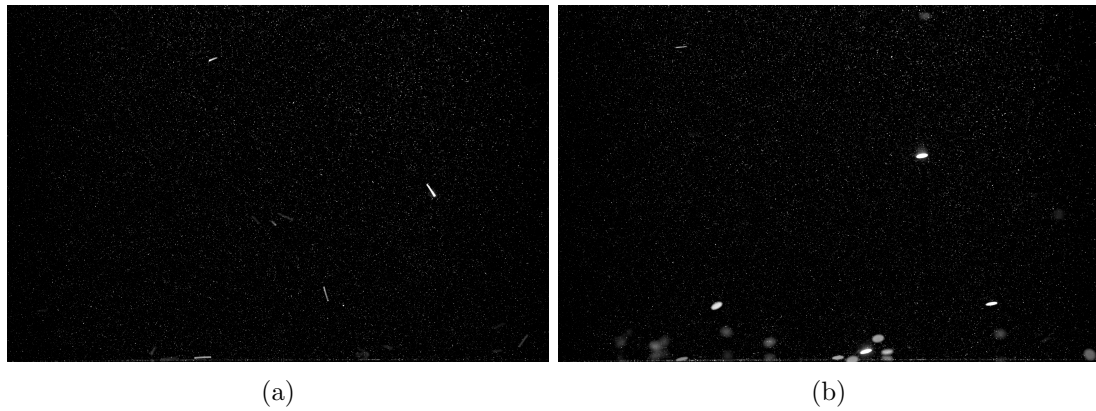


Figure 2.9: Instantaneous realization of the particle-laden flow with rods (a) and disks (b).

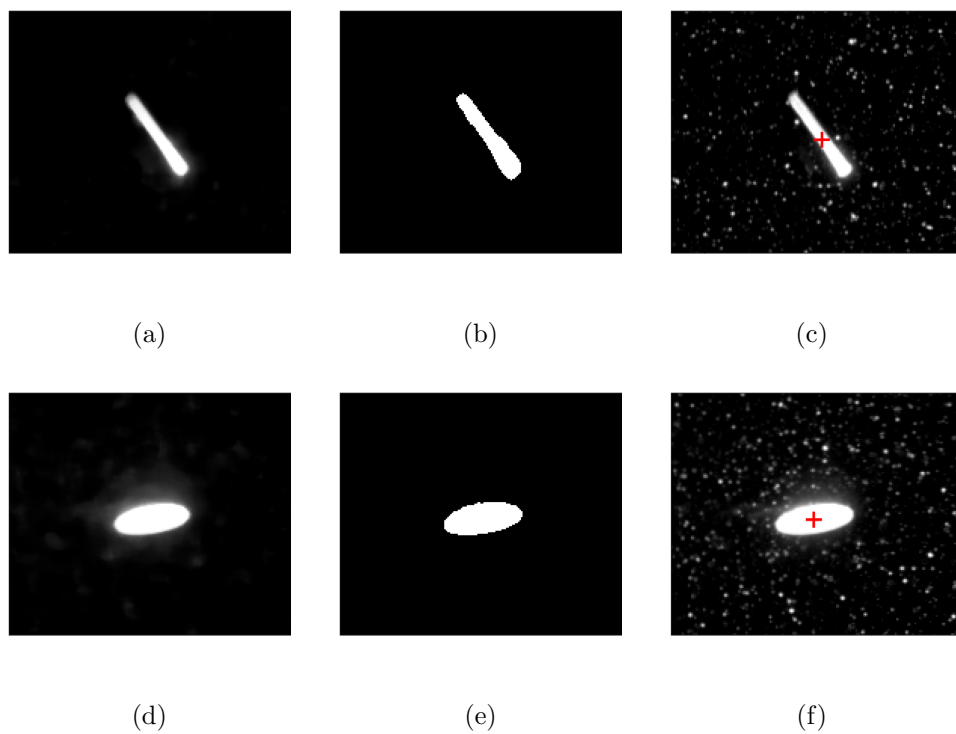


Figure 2.10: Intensity-based segmentation method for particle detection for a rod (a-c) and disk (d-f) particle: (a, d) median filtered image, (b, e) segmented image, and (c, f) identified particle in original image, with the red cross indicating the detected particle centroid.

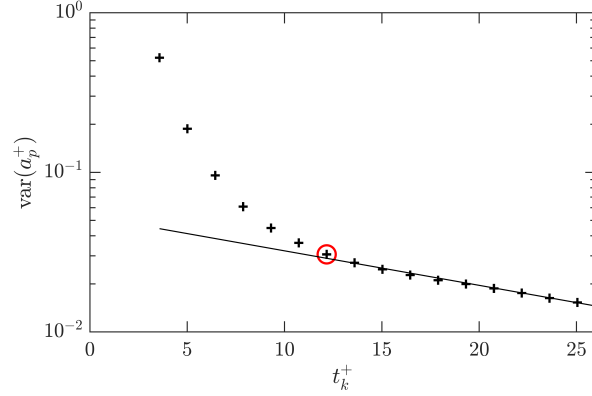


Figure 2.11: Streamwise acceleration variance as a function of smoothing kernel width. The solid line indicates the fit of the acceleration variance over its exponential range, and the optimal kernel width is denoted by the open circle.

The centroids are tracked between successive image pairs using a PIV-based predictor: a first-guess displacement is estimated from the mean fluid velocity profile interpolated at the wall-normal location of each particle centroid and subtracted from the second frame in the pair. Then, a nearest-neighbor search with a search radius of one particle diameter is used to match particle centroids in the first frame with the shifted centroids in the second one. As the inter-frame particle displacement is about one particle diameter, there is no ambiguity in matching particle images. Approximately 2500 particles were tracked within the image set. To obtain particle velocities and accelerations, the particle trajectories are convolved with the first and second derivative of a Gaussian kernel, respectively. This method, introduced for fluid tracers (Voth *et al.*, 2002; Mordant *et al.*, 2004), has been used in several studies of inertial particles in turbulence (Gerashchenko *et al.*, 2008; Nemes *et al.*, 2017; Ebrahimian *et al.*, 2019). The optimal width of the kernel t_k is determined from the variance of the particle acceleration magnitude in the data set: the latter is calculated for a range of kernel widths, and the smallest value for which the variance start decaying exponentially is adopted (figure 2.11). This corresponds to a duration of 17 successive snapshots, or about $12\tau^+$, where $\tau^+ = \nu/u_\tau$ is the time scale based on wall units.

In the data analysis, we will consider the fluid velocity at the particle-location, $u_{f|p}$. For spheres, this is obtained by interpolating the PIV vectors onto the instantaneous

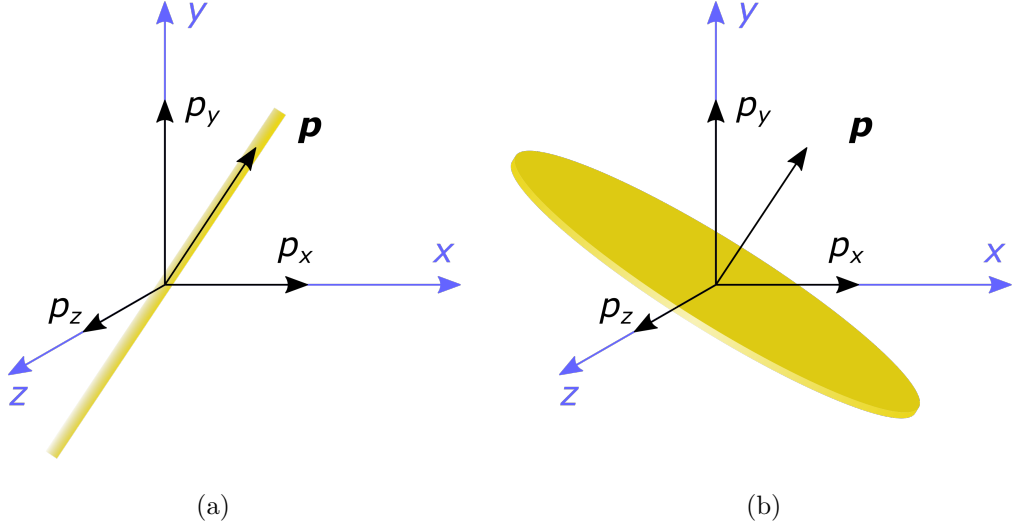


Figure 2.12: Definition of the particle orientation vector \mathbf{p} and its components shown for rods (a) and disks (b) relative to the water channel reference frame shown in blue.

particle centroid location using an inverse-distance-weighted average of the fluid velocity in the 4×4 vector neighborhood surrounding each particle (a 2×2 neighborhood is used for $y^+ < 25$ to account for the greater shear). For rods and disks, this is obtained by averaging the fluid velocity vectors within a distance of $D_p/4$ from the edge of particle. As the particles have finite size, this definition does not accurately represent an undisturbed fluid velocity at the particle location (as used in the correct definition of the drag force, Horwitz & Mani, 2016), but it will serve the purpose of investigating the fluid flow events experienced by the particles.

2.5 Particle orientation measurement

The three-dimensional particle orientation vector, \mathbf{p} , was computed for the disk and rod particles. The vector \mathbf{p} is defined as the unit vector passing through the particle's axis of symmetry, and thus, each component of \mathbf{p} is the cosine of the angle between the particle's axis of symmetry and the respective coordinate axis in the water channel reference frame (figure 2.12).

Calculation of the anisotropic particle orientation is complicated by the limitation

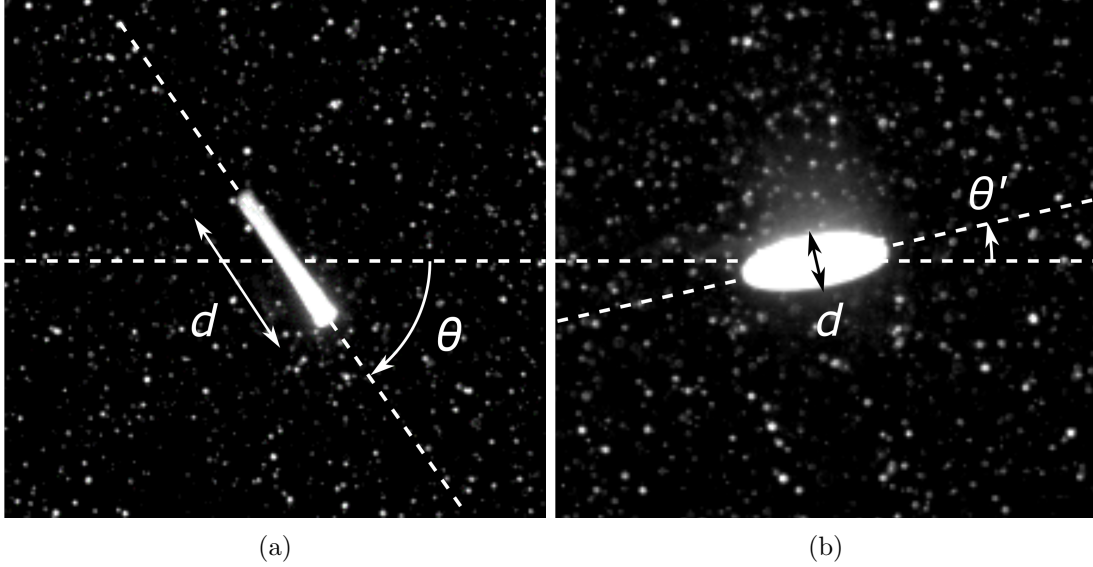


Figure 2.13: Diagram defining (a) the apparent pitch θ and apparent length d of rod particles and (b) the pitch θ' and apparent diameter d of the disk particles.

that only the two-dimensional projection of the rods and disks is seen in the images. However, with the caveat that the sign of p_z cannot be determined, the particle orientation can be reconstructed from the apparent pitch (θ , θ') and apparent major axis length (d) of the rod and disk particle projections, respectively, illustrated in figure 2.13, using trigonometry.

Before the orientation can be calculated, the apparent major axis length of the particles must be corrected for the finite thickness of the particles, which artificially increases the minimum apparent major axis length when a particle is seen at an angle (figure 2.14a). This minimum is taken to be the first-percentile apparent major axis length; that is, the value of d below which 1% of the observations are found (denoted $d_{1\%}$). However, more of the particle thickness is seen as a particle tilts closer to an “edge-on” orientation, so the correction value that must be subtracted depends on the orientation itself. The correction value is scaled linearly with the apparent major axis length, so that the corrected major axis length is given by $d_{corr} = d - d_{1\%} \frac{D_p - d}{D_p}$. When the resulting shifted major axis length is negative, it is set to zero. The PDFs of the original d and corrected d_{corr} are shown in figure 2.14b (rods) and c (disks).

The set of formulas to compute the correction to the apparent major axis length and

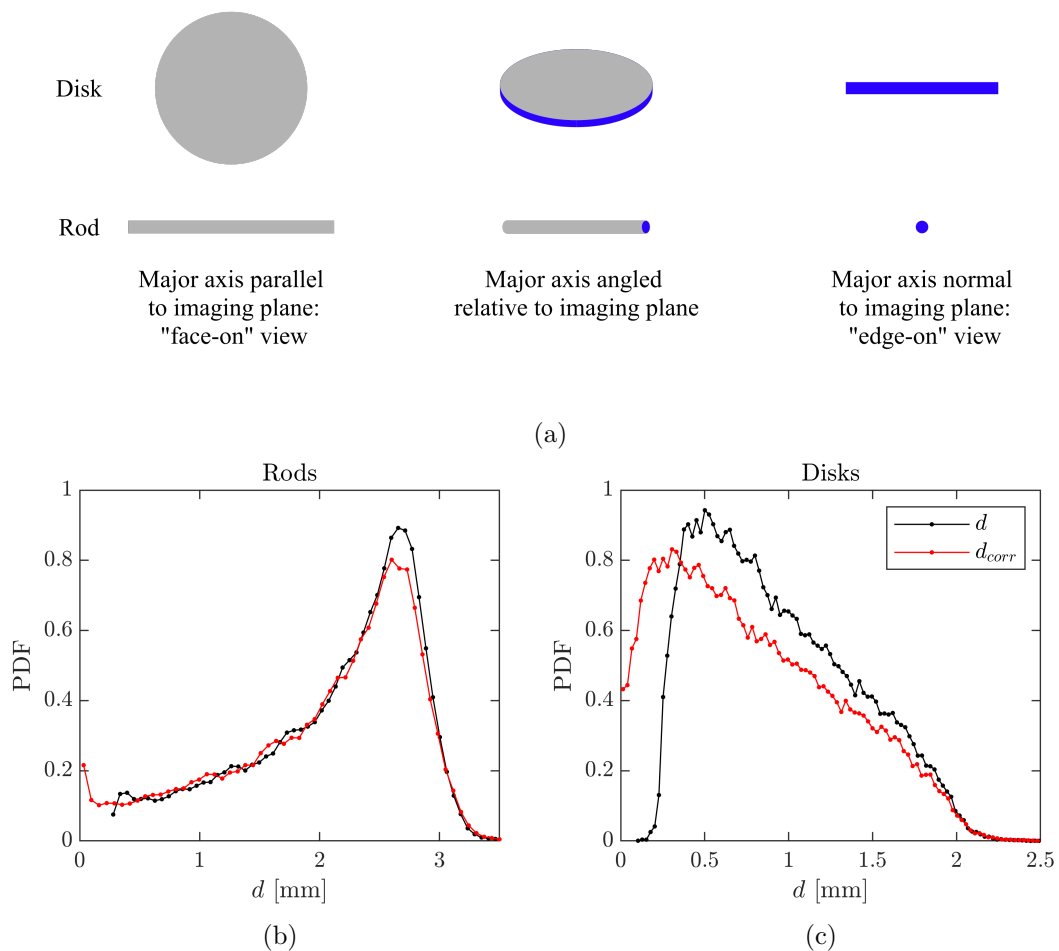


Figure 2.14: (a) Schematic of the finite particle thickness when a particle is seen at an angle. The edge of the particle is shown in blue (thickness exaggerated), illustrating how the edge becomes more visible as the particle tilts from a “face-on” to an “edge-on” view. (b, c) PDFs of the original and corrected apparent major axis length d and d_{corr} , respectively, for rods (b) and disks (c).

Quantity	Rods	Disks	Range
d_{corr}	$\max \left[d - d_{1\%} \frac{D_p - d}{D_p}, 0 \right]$		
p_x	$\frac{d_{corr}}{D_p} \cos(\theta)$	$\sin(\theta') \left(1 - \left(\frac{d_{corr}}{D_p} \right)^2 \right)^{1/2}$	$[0, 1]$
p_y	$\frac{d_{corr}}{D_p} \sin(\theta)$	$\cos(\theta') \left(1 - \left(\frac{d_{corr}}{D_p} \right)^2 \right)^{1/2} (-\text{sign}(\theta'))$	$[-1, 1]$
p_z	$\left(1 - \left(\frac{d_{corr}}{D_p} \right)^2 \right)^{1/2}$	$\frac{d_{corr}}{D_p}$	$[0, 1]$

Table 2.5: Formulas to compute the particle orientation vector for rod and disk particles, as well as the range of each component.

the components of the particle orientation vector are given in table 2.5. Once calculated, the components of \mathbf{p} are convolved with a Gaussian smoothing kernel of width 17 frames (the same as was done to obtain particle linear velocity and acceleration) to reduce measurement noise. The unit length of \mathbf{p} is then checked. If $|1 - |\mathbf{p}|| > 0.05$, then that orientation observation is rejected and not considered when computing statistics (however, the particle position and velocity values are preserved). This criterion results in the rejection of about 1.5% of rod and disk observations. Finally, due to the spread in lengths of the rod particles, p_z will be imaginary if $d_{corr} > D_p$. All three components of \mathbf{p} are rejected if p_z is imaginary, removing about 6% of rod particle observations.

Particle angular velocity and angular acceleration are also of interest. A particle's solid-body rotation rate $\boldsymbol{\Omega}$ can be decomposed into a spinning component and a tumbling component, $\boldsymbol{\Omega} = \Omega_p \mathbf{p} + \mathbf{p} \times \dot{\mathbf{p}}$, where spinning is rotation about the symmetry axis ($\Omega_p \mathbf{p}$) and tumbling is rotation of the symmetry axis ($\mathbf{p} \times \dot{\mathbf{p}}$). Spinning motion is inaccessible to our optical imaging; we therefore focus on tumbling rates exclusively. The tumbling rate is then given by $\boldsymbol{\omega}_t = \mathbf{p} \times \dot{\mathbf{p}}$, and the tumbling component of angular acceleration is given by $\boldsymbol{\alpha}_t = \mathbf{p} \times \ddot{\mathbf{p}}$. The first and second derivatives of particle orientation, $\dot{\mathbf{p}}$ and $\ddot{\mathbf{p}}$, are computed again by convolving the components of \mathbf{p} with first and second derivatives, respectively, of a Gaussian smoothing kernel of width 17 frames.

Before $\dot{\mathbf{p}}$ and $\ddot{\mathbf{p}}$ are computed, and before \mathbf{p} is smoothed, ambiguities on the signs of the components of \mathbf{p} must be resolved in order to ensure that \mathbf{p} is differentiable.

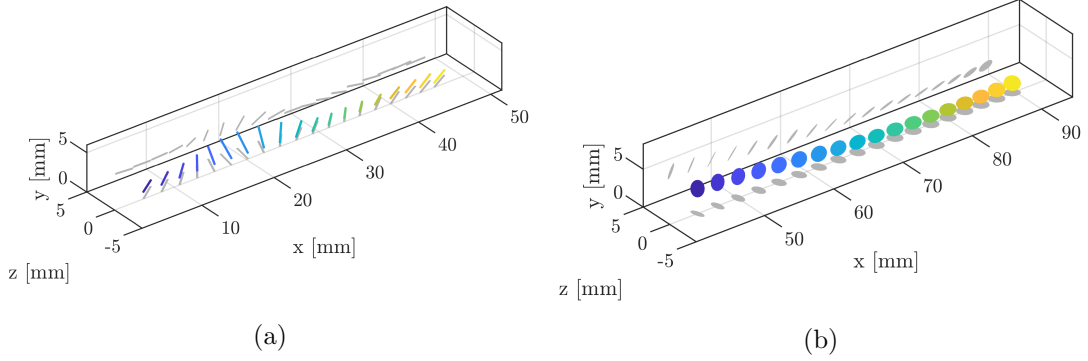


Figure 2.15: Example reconstructed trajectories of a rod (a) and a disk (b) moving in space and time. Snapshots are shown every 5 frames ($3.6\tau^+$).

Sign ambiguities occur when the components of \mathbf{p} reach the bounds of their range. For example, since the range of p_y is $[-1, 1]$, p_y of a particle which is tumbling end-over-end in the x - y plane will eventually reach a value just above -1 as it passes through the vertical orientation and jump to just under 1 in the next realization, while the value of p_x remains positive throughout. In order to differentiate \mathbf{p} , the signs of p_y and p_x must be flipped as the particle passes through this orientation. Sign ambiguities are resolved by enforcing a minimum angular acceleration condition on the raw (unsmoothed) \mathbf{p} values. First, observations where any of the components of \mathbf{p} change sign or approach 0 , 1 , or -1 , and are also a local temporal minimum or maximum, are flagged. Three sets of sign changes are applied to the flagged observations: (1) flip only p_x and p_y , (2) flip only p_z , and (3) flip p_x , p_y and p_z . The unsmoothed tumbling angular acceleration magnitude $\dot{\mathbf{p}}\dot{\mathbf{p}}$ is computed for each case, as well as the original case where no signs are changed. The case with the minimum $\dot{\mathbf{p}}\dot{\mathbf{p}}$ is chosen, and the sign change is propagated forward in time along the remainder of that particle's track. In general, the $\dot{\mathbf{p}}\dot{\mathbf{p}}$ value associated with the correct set of sign changes will be at least an order of magnitude lower than the other three, so it is trivial to make the choice. After the sign changes are applied, the smoothed \mathbf{p} , $\dot{\mathbf{p}}$ and $\ddot{\mathbf{p}}$ values are computed as described above. Example reconstructed trajectories for a rod and a disk particle are shown in figure 2.15.

2.6 Measurement uncertainty

Uncertainty in the particle statistics is estimated by considering both random uncertainty (due to the finite sample size) and bias uncertainty (due to imperfect centroid and orientation detections). The random uncertainty is estimated by computing 95% confidence intervals on the statistics (Bendat & Piersol, 2011). To evaluate the random uncertainty of particle statistics, we assume a number of independent realizations equal to the number of recorded trajectories. When statistics are computed within wall-normal bins, we assume a number of independent realizations equal to the number of trajectories in each bin.

The bias uncertainty is estimated using synthetic particle templates created from actual particle images. Sphere templates are generated from a sphere image in which one quadrant of the image is mirrored over the horizontal and vertical axes, creating a synthetic particle template for which the centroid is known precisely. Rod and disk templates are generated from images that are stretched so that $d = D_p$, then mirrored over each axis as for the spheres. The synthetic particle templates are translated and superimposed upon a tracer-filled PIV background to create synthetic particle trajectories with known centroids. The imposed centroids are chosen to be sinusoids so that the measured derivatives of position and orientation can be compared with their analytical values. A time-series of 3D rod and disk orientations are defined in which all components of \mathbf{p} vary sinusoidally. These orientations are projected onto the plane of the image, and particle templates are stretched and rotated according to the projections to simulate what the camera would capture. Then, detection, tracking, and (for disks and rods) orientation measurements are performed on the synthetic images. The associated uncertainties on the centroid location, velocity, acceleration, orientation, tumbling rate, and tumbling acceleration are estimated as the root mean square (RMS) difference between measured and actual values. These bias uncertainties are reported in table 2.6.

There is an additional uncertainty on the orientation of rod particles and derivatives thereof owing to the spread in rod lengths. The uncertainty is estimated as $w_{D_{p,rods}} = \sigma_{D_{p,rods}}/D_{p,rods}$, where $\sigma_{D_{p,rods}}$ is the standard deviation of the rod lengths. This uncertainty is propagated through the orientation and tumbling rate calculations to obtain the additional uncertainty on those quantities; it has the greatest effect on

Bias uncertainty	Spheres	Rods	Disks
w_{x_p}, w_{y_p}	0.03 mm, 0.7 ⁺	0.02 mm, 0.5 ⁺	0.03 mm, 0.5 ⁺
w_{u_p}, w_{v_p}	1 mm/s, 0.06 ⁺ , 0.1%	2 mm/s, 0.1 ⁺ , 0.5%	4 mm/s, 0.2 ⁺ , 1%
$w_{a_{x,p}}, w_{a_{y,p}}$	20 mm/s ² , 0.003 ⁺ , 3%	27 mm/s ² , 0.003 ⁺ , 3%	55 mm/s ² , 0.006 ⁺ , 6%
w_{p_x}	–	0.01, 1%	0.03, 12%
w_{p_y}	–	0.02, 8%	0.02, 2%
w_{p_z}	–	0.05, 10%	0.05, 10%
$w_{\omega_{t,x}}$	–	0.7 s ⁻¹ , 0.002 ⁺ , 13%	0.9 s ⁻¹ , 0.002 ⁺ , 10%
$w_{\omega_{t,y}}$	–	0.7 s ⁻¹ , 0.002 ⁺ , 8%	1.2 s ⁻¹ , 0.003 ⁺ , 25%
$w_{\omega_{t,z}}$	–	1.4 s ⁻¹ , 0.003 ⁺ , 17%	0.5 s ⁻¹ , 0.001 ⁺ , 7%
$w_{\alpha_{t,x}}$	–	90 s ⁻² , 0.0005 ⁺ , 25%	100 s ⁻² , 0.0006 ⁺ , 17%
$w_{\alpha_{t,y}}$	–	90 s ⁻² , 0.0005 ⁺ , 12%	250 s ⁻² , 0.001 ⁺ , 50%
$w_{\alpha_{t,z}}$	–	180 s ⁻² , 0.001 ⁺ , 50%	50 s ⁻² , 0.0003 ⁺ , 15%

Table 2.6: Bias uncertainties on the particle centroid location, velocity, acceleration, orientation, tumbling rate, and tumbling acceleration for each particle type in SI units, wall units, and as a percentage of characteristic values of the quantities.

the uncertainty on rod particle p_z , $\omega_{t,x}$, $\omega_{t,y}$, $\alpha_{t,x}$, and $\alpha_{t,y}$. Error bars on the plots in the following sections represent the root sum of squares (RSS) of random and bias uncertainties as well as the rod length uncertainty.

Uncertainty on the fluid velocities consists of random error and PIV bias error; the random error is dominant. Following Adrian & Westerweel (2011), the bias error on the PIV correlation peak is estimated as 0.1 px, or 2 mm/s ($0.1u_\tau$). To calculate the random uncertainty on statistics, the number of independent samples in the fluid velocity data is estimated as the number of temporally independent realizations (i.e., the number of boundary layer turnover times in the recording) multiplied by the number of spatially independent samples in each realization (i.e., w/d_{99} , where d_{99} is the boundary layer thickness).

For the fluid velocity evaluated at the particle location, the interpolation also contributes to the uncertainty. This uncertainty is estimated by applying a synthetic particle mask to images where the actual velocity vectors are known, performing PIV analysis on the masked images, then interpolating the resulting fluid velocity at the location of the synthetic particles. The actual fluid velocity is then compared with the interpolated values. The resulting interpolation error on the fluid velocity, again defined as the RMS

difference between the actual and calculated values, is approximately 1 mm/s ($0.05u_\tau$) for both rods and disks, significantly smaller than the random error. To avoid cluttering in the plots, in the following error bars are added only where significant.

Chapter 3

Results: spherical particles

The contents of this chapter were published in the Journal of Fluid Mechanics in December, 2020 under the title “Particle–fluid–wall interaction of inertial spherical particles in a turbulent boundary layer”, 908, p. A39. Reprinted with permission.

3.1 Fluid and particle velocity

Here and in the following, the streamwise and wall-normal coordinates are indicated by x and y , respectively, and u and v indicate the respective velocity components. These are Reynolds-decomposed as $u = \langle u \rangle + u'$ and $v = \langle v \rangle + v'$, where angle brackets denote the time average and the prime denotes the fluctuating part. Subscripts f and p denote quantities referring to fluid and particles, respectively, and the subscript $f|p$ denotes fluid quantities interpolated at the particle location. In figures 3.1 and 3.2, the particle-laden and unladen fluid velocity statistics are compared to turbulent boundary layer measurements by De Graaff & Eaton (2000) at a similar Reynolds number ($Re_\theta = 1430$). The particle-laden and unladen fluid velocity profiles overlap within experimental uncertainty, indicating that significant two-way momentum coupling between the particles and fluid is not present. From the mean velocity profile, the friction velocity is determined by iterative fitting, with the von Kármán constant $\kappa = 0.41$ and the additive constant $B = 5.5$. The Reynolds stress profiles show some discrepancies in the magnitudes of the peak stresses due to the non-canonical features of the channel design (unconventional forcing, limited channel width) and limited spatial resolution.

U_∞ (m/s)	H (mm)	W (mm)	δ_{99} (mm)	u_τ (mm/s)	Re	Re_τ	Re_θ
0.42	150	150	29	18.5	66 000	570	1270

Table 3.1: Physical parameters of the water channel and boundary layer properties. U_∞ is the freestream velocity, H is the water depth, W is the channel width, δ_{99} is the boundary layer thickness, and u_τ is the shear velocity. The boundary thickness is defined such that $u(\delta_{99}) = 0.99U_\infty$. $Re = U_\infty H/\nu$, $Re_\tau = u_\tau \delta_{99}/\nu$, and $Re_\theta = U_\infty \theta/\nu$ are the freestream, friction, and momentum thickness Reynolds numbers, respectively. Standard water properties at 22°C are used in the calculations.

Physical parameters of the water channel and the boundary layer properties are reported in table 3.1.

Profiles of particle velocity are obtained by defining wall-normal layers (bins) and taking the mean of particle velocities within each. Particles are more numerous near the wall and sparser in the outer region (approximately following a power law, see §3.6), thus the bins are logarithmically spaced to equalize the numbers of particles in each, as well as to capture the high shear in the near-wall region. The mean streamwise and wall-normal particle velocity profiles are shown in figure 3.3. In the freestream, the particle streamwise velocity is very similar to the fluid’s (figure 3.3a), as expected since there the particles are in equilibrium with a steady flow having negligible fluctuations. Closer to the wall ($y^+ \lesssim 200$) the particles generally lag the fluid, due to their inertia in responding to turbulence. Past experiments found that mean velocity of inertial particles exceeded that of the fluid in the viscous sublayer; see Kaftori *et al.* (1995a); Righetti & Romano (2004); Ebrahimian *et al.* (2019). The present PIV resolution does not allow reliable measurements at such small heights, but the canonical shape of the boundary layer profile suggests that the lag is vanishing approaching the wall. We remark that those previous studies considered smaller particles (in wall units) whose centroid could reach closer to the wall.

The vertical velocity profile (figure 3.3b) shows that in the freestream the particles settle through the fluid at a speed close to the still-fluid terminal velocity. This is again consistent with the fact that particles at those heights fall through a quasi-laminar flow. For $y^+ \lesssim 200$ (the same range for which particles lag the fluid streamwise velocity), the vertical velocity decays in magnitude, but remains negative. We note that a downward

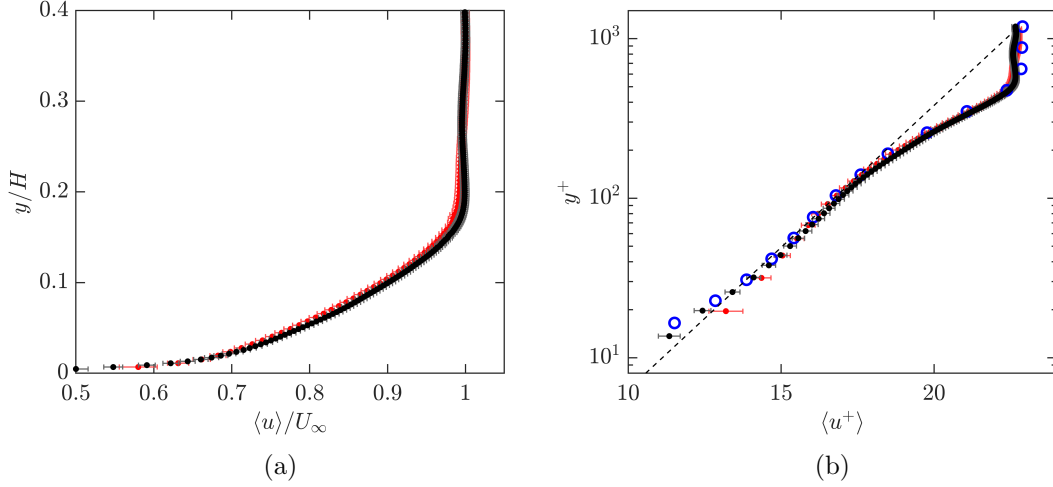


Figure 3.1: Mean streamwise velocity profile of the particle-laden (black dots) and unladen (red dots) fluid, in (a) outer units and (b) wall units. The dashed line in (b) indicates the logarithmic law fit. The profile is compared with De Graaff & Eaton (2000) in (b), shown in blue open circles.

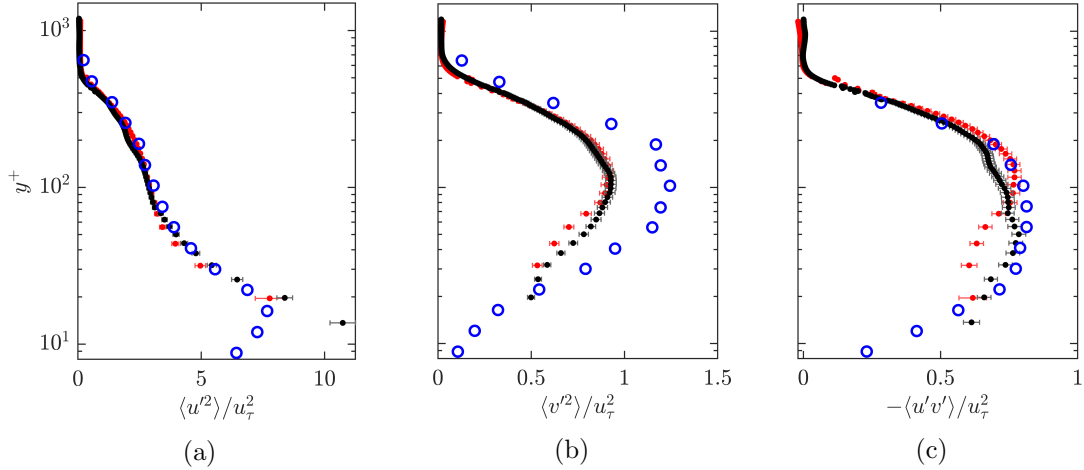


Figure 3.2: Profiles of particle-laden (black dots) and unladen (red dots) streamwise turbulent normal stress (a), wall-normal normal stress (b), and shear stress (c) of the fluid in wall units. The profiles are compared with De Graaff & Eaton (2000) shown in blue open circles.

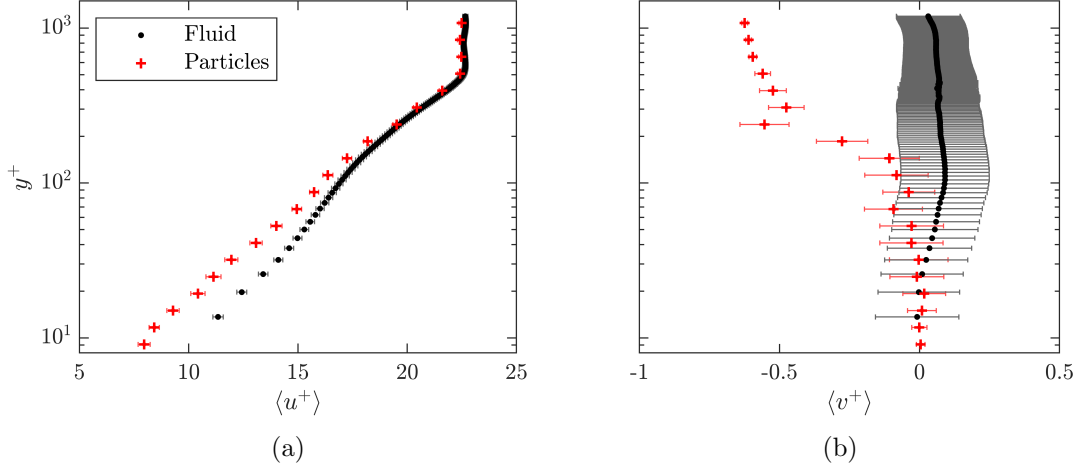


Figure 3.3: Wall-normal profiles of streamwise (a) and wall-normal (b) mean particle velocity (red crosses) compared with the mean fluid velocity (black dots).

mean particle velocity is expected under equilibrium conditions, i.e., when the wall-normal turbulent flux balances the gravitational settling (Rouse, 1937; Prandtl, 1952). Using the concentration measurements (see §3.6), we estimate the total vertical flux to be several orders of magnitude smaller than the streamwise flux, confirming approximate equilibrium conditions. The Rouse–Prandtl theory, however, assumes a constant settling velocity (generally taken to be equal to the still-fluid terminal velocity) throughout the boundary layer, while here it shrinks to vanishingly small values approaching the wall. We investigate the roots of this effect, as well as the streamwise velocity lag, in the following.

3.2 Slip velocity

The reduced streamwise velocity of the particles has been often attributed to the preferential sampling of slow fluid regions (Kaftori *et al.*, 1995*a*; Kiger & Pan, 2002). We investigate this issue first by separating the mean slip velocity ($\langle u_p \rangle - \langle u_f \rangle$) in two separate contributions: the ‘particle-conditioned’ slip velocity, i.e., the mean slip velocity at the particle location, $\langle u_p - u_{f|p} \rangle$, and the ‘apparent’ slip velocity due to the oversampling

of fluid regions faster or slower than the average, $\langle u_{f|p} \rangle - \langle u_f \rangle$ (Kiger & Pan, 2002):

$$\langle u_p \rangle - \langle u_f \rangle = \langle u_p - u_{f|p} \rangle + \langle u_{f|p} \rangle - \langle u_f \rangle. \quad (3.1)$$

Figure 3.4a displays both contributions. (We only report the slip velocity down to the location of the PIV vector closest to the wall, to avoid extrapolation.) It indicates that, for $y^+ > 20$, the particles do oversample fluid regions with negative streamwise fluctuations ($\langle u_{f|p} \rangle - \langle u_f \rangle < 0$). Closer to the wall, however, the particle-conditioned slip plays a dominant role in determining the particle lag from the fluid: the term $\langle u_p - u_{f|p} \rangle$ becomes larger in magnitude than $\langle u_{f|p} \rangle - \langle u_f \rangle$. This is consistent with the recent findings of Berk & Coletti (2020) who considered solid particles in air at much larger Re_τ and a broad range of St^+ .

A similar decomposition can be carried out for the vertical velocity component, noting that $\langle v_f \rangle = 0$:

$$\langle v_p \rangle = \langle v_p - v_{f|p} \rangle + \langle v_{f|p} \rangle \quad (3.2)$$

which highlights the separate contributions of the particle-conditioned slip and the vertical fluid velocity at the particle location. Figure 3.4b shows that the first term on the right-hand side dominates in the freestream and decreases approaching the wall. The second term, representing the preferential sampling of upward/downward fluid fluctuations, is negligible in the freestream and it becomes comparable to the first term as the wall is approached. In particular, particles near the wall oversample upward fluid motions ($\langle v_{f|p} \rangle > 0$). This is consistent with their tendency of favouring negative streamwise fluctuations, which are correlated with upward fluctuations in a turbulent shear flow. This point will be further discussed in §3.4. In general, throughout the boundary layer, the effect of the turbulence on the particle settling is opposite to what one would expect from homogeneous turbulence studies, where the predominant effect is the enhancement of settling speed by preferential sweeping (Wang & Maxey, 1993; Petersen *et al.*, 2019).

The mean particle-conditioned slip velocity can be used to define profiles of particle Reynolds numbers, $Re_{p,u_{slip}} = \langle u_p - u_{f|p} \rangle D_p / \nu$ and $Re_{p,v_{slip}} = \langle v_p - v_{f|p} \rangle D_p / \nu$, shown in figure 3.5. Given the observed ranges, the particle wakes are likely to extend for less than one diameter (Rimon & Cheng, 1969). At the present volume fraction, particles

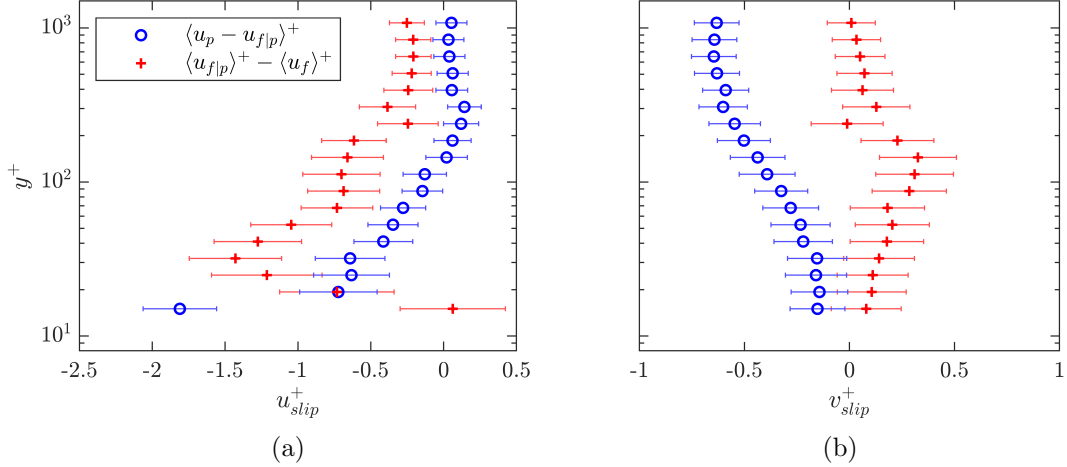


Figure 3.4: Wall-normal profiles of mean streamwise (a) and wall-normal (b) particle slip velocity, separated into the particle-conditioned mean slip (blue circles) and the apparent mean slip (red crosses).

are hardly ever found so close to each other, indicating that the momentum coupling between particles can be assumed to be negligible. However, the Reynolds numbers are well into the non-linear drag regime, especially in the near-wall region. While drag corrections are available (Clift *et al.*, 2005), those are developed for steady/quiescent flows. In a turbulent flow laden with particles at finite Re_p , the non-linearities undermine the use of superposition (assumed in the derivation of the particle equation of motion, Maxey & Riley, 1983), making the particle-fluid dynamics challenging to capture with point-particle simulations (Wang *et al.*, 2019).

The instantaneous slip experienced by the particles with respect to the surrounding fluid is related to their ability to retain memory of the flow events experienced at previous times. Thus, one might infer that the gravitational drift plays a major role in determining the streamwise slip velocity, as the settling particles cross flow trajectories and attain large relative velocities with respect to the fluid. This view is certainly valid in homogeneous turbulence (e.g., Csanady, 1963; Elghobashi & Truesdell, 1992). In a turbulent boundary layer, however, the tendency of the particles to sample slow flow regions, combined with the mean wall-normal velocity gradient, leads to a different outcome. Let us consider separately the mean streamwise velocity profile for ascending

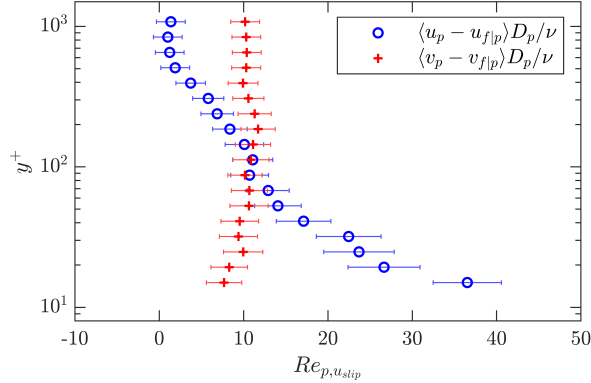


Figure 3.5: Profiles of mean instantaneous particle Reynolds number based on the particle-conditioned streamwise (blue circles) and wall-normal (red crosses) slip velocity.

and descending particles; that is, particles with positive and negative instantaneous vertical velocity, respectively. Figure 3.6a shows that ascending particles, on average, move slower than the fluid and account for most of the mean slip velocity reported above; while descending particles roughly match the mean fluid velocity in the outer layer. This trend, in agreement with Kiger & Pan (2002) and van Hout (2011), is explained by the fact that ascending particles come from slower-moving regions of the flow nearer to the wall, and therefore have lower streamwise velocities. Therefore, unlike in homogeneous flows, it is the ascending particles suspended by the turbulence that determine the large slip velocity, rather than the descending ones that settle due to gravity. Remarkably, the vertical velocity of the ascending particles is comparable in magnitude to that of the descending ones, both being the order of the friction velocity. As the descending particles near the wall are more numerous, their contributions dominate the statistics and the mean vertical velocity of the dispersed phase is negative.

3.3 Reynolds stresses

Profiles of particle and fluid Reynolds stresses are compared in figure 3.7. The streamwise normal stress of the particles are comparable to that of the fluid, while the particle wall-normal normal stress and shear stress exceed that of the fluid by in the range $20 \lesssim y^+ \lesssim 200$. Qualitatively similar results were reported for particles in water

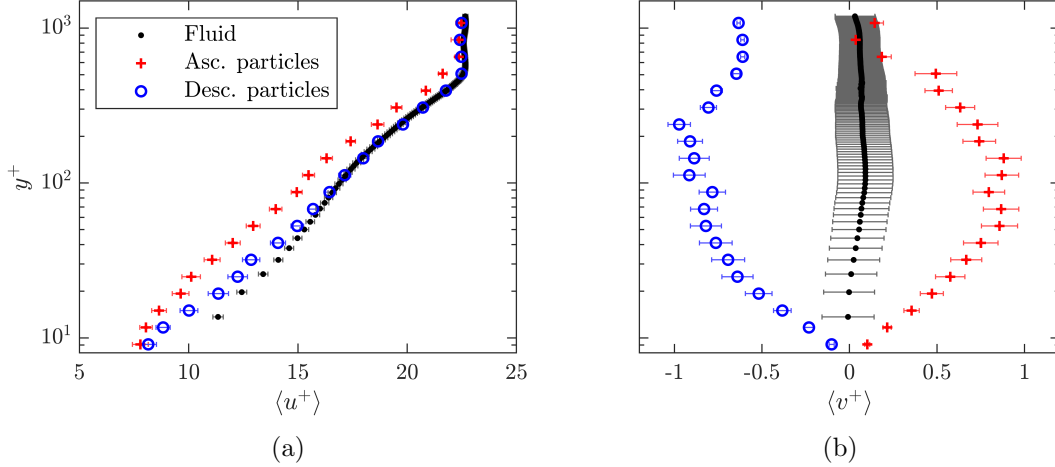


Figure 3.6: Profiles of mean streamwise (a) and wall-normal (b) particle velocity conditioned on ascending (red crosses) and descending (blue circles) particles compared to the fluid velocity (black dots).

(Kaftori *et al.*, 1995*b*; van Hout, 2011) and in air (e.g., Tanière *et al.*, 1997; Fong *et al.*, 2019). The relatively large particle velocity fluctuations are interpreted as a consequence of the spread in momentum of particles with different pathways, retaining memory of their interactions with disparate flow structures. This in turn results in particles often being surrounded by fluid with velocity different from their own, contributing to the instantaneous slip reported above.

To explore the particle-turbulence interaction, we can again condition the fluid statistics on the location of ascending and descending particles. The Reynolds shear stresses are of special interest: they feature in the turbulence production and represent the statistical signature of the instantaneous sweep and ejection events that are believed to play a crucial role in the particle transport (Marchioli & Soldati, 2002). Figure 3.8a displays the fluid Reynolds shear stress evaluated at the locations of ascending and descending particles, while figure 3.8b shows the ‘particle Reynolds shear stress’ associated to ascending and descending particles. The ascending particles appear to sample regions with much larger fluid shear stress magnitudes compared to the descending particles, while the shear stress magnitudes of ascending and descending particles themselves are nearly the same. That suggests that the motion of the former is strongly driven by

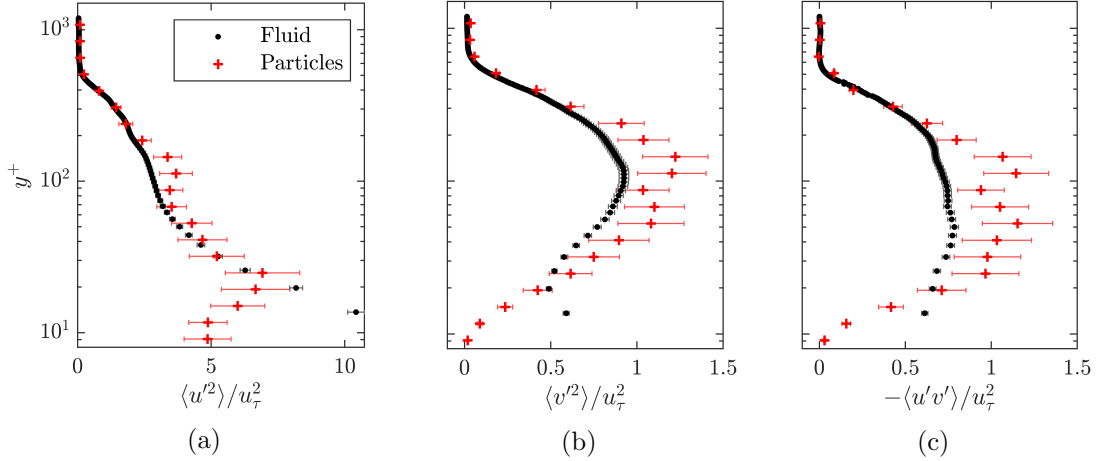


Figure 3.7: Wall-normal profiles of the Reynolds stresses of the particles (red crosses) and fluid (black dots) normalized by the squared shear velocity.

turbulent ejection events, while the latter have a weaker relation to sweep events.

3.4 Quadrant analysis

Previous work (e.g., Niño & Garcia, 1996; Kiger & Pan, 2002; Marchioli & Soldati, 2002; van Hout, 2011) found evidence that inertial particles are strongly affected by sweep and ejection events in the turbulent boundary layer. Sweeps are identified as simultaneous $u'_f > 0$ and $v'_f < 0$ events (fourth quadrant of the u'_f - v'_f plane, or Q4) and ejections as simultaneous $u'_f < 0$ and $v'_f > 0$ (second quadrant, or Q2). They are often associated with coherent structures in wall turbulence, such as streamwise rollers and hairpin vortices (Robinson, 1991). We first plot in figure 3.9 the joint PDF of streamwise and wall-normal fluid velocity fluctuations: for the near-wall region ($y^+ < 100$, figure 3.9a) and farther away from the wall ($y^+ > 100$, figure 3.9b). As expected, sweeps and ejections are dominant near the wall, whereas away from the wall the fluctuations are weaker and there are no dominant quadrants. We then consider the quadrant events at the location of ascending and descending particles, in the near-wall and outer regions. Near the wall, ascending particles are found to strongly oversample ejection events (figure 3.9c), supporting the view that ejections are a major mechanism driving particle

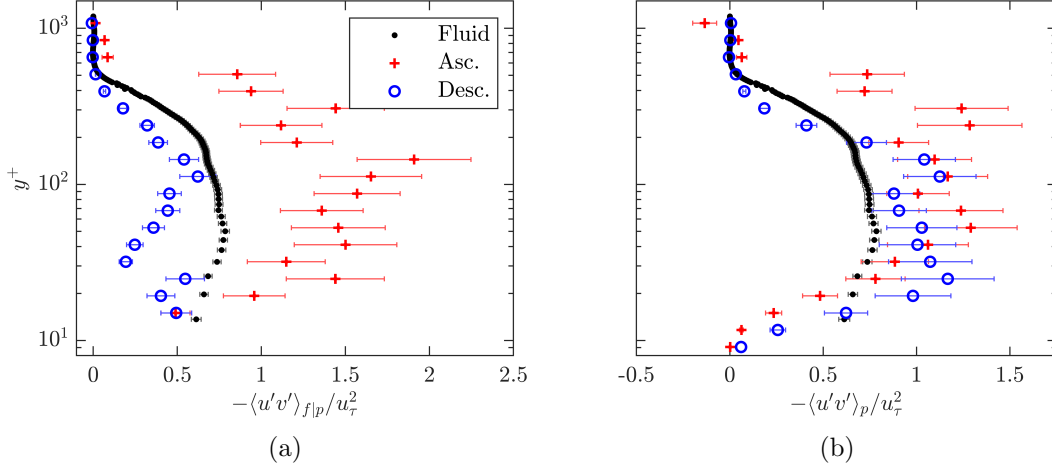


Figure 3.8: Wall-normal profiles of the Reynolds shear stress of (a) the fluid velocity at particle locations and (b) the particle velocity, conditioned on ascending and descending particles (red crosses and blue circles, respectively). The profiles are compared to the overall fluid shear stress profile (black dots).

resuspension. Even in the outer region, although the ejections themselves are weaker, ascending particles still occupy the second quadrant almost exclusively (figure 3.9d). In contrast, descending particles are found to oversample sweep events near the wall, but the preference is weaker (figure 3.9e), and in the outer region, descending particles do not preferentially sample any quadrant (figure 3.9f). This indicates that sweeps weakly influence the descent of particles towards the wall, while ejections are a key factor in lifting the particles away from the wall.

The prevalence of fluid ejection over sweeps in influencing particle transport was reported by previous studies focused on heavy particles suspended in horizontal wall-bounded flows over a wide range of physical parameters (Kiger & Pan, 2002; Li *et al.*, 2012; van Hout, 2011; Zhu *et al.*, 2019; Berk & Coletti, 2020). This is in contrast with configurations in which gravity does not participate to the wall-normal transport: in no-gravity simulations (e.g., Marchioli & Soldati, 2002) and in vertical channel flow experiments (e.g., Fong *et al.*, 2019) sweep events crucially contribute to the turbophoretic drift that produces a multi-fold increase in near-wall concentration. In horizontal particle-laden flows, by contrast, the near-wall concentration has been found to be smaller than what predicted by the Rouse–Prandtl equilibrium theory (Kiger & Pan, 2002; Zhu *et al.*,

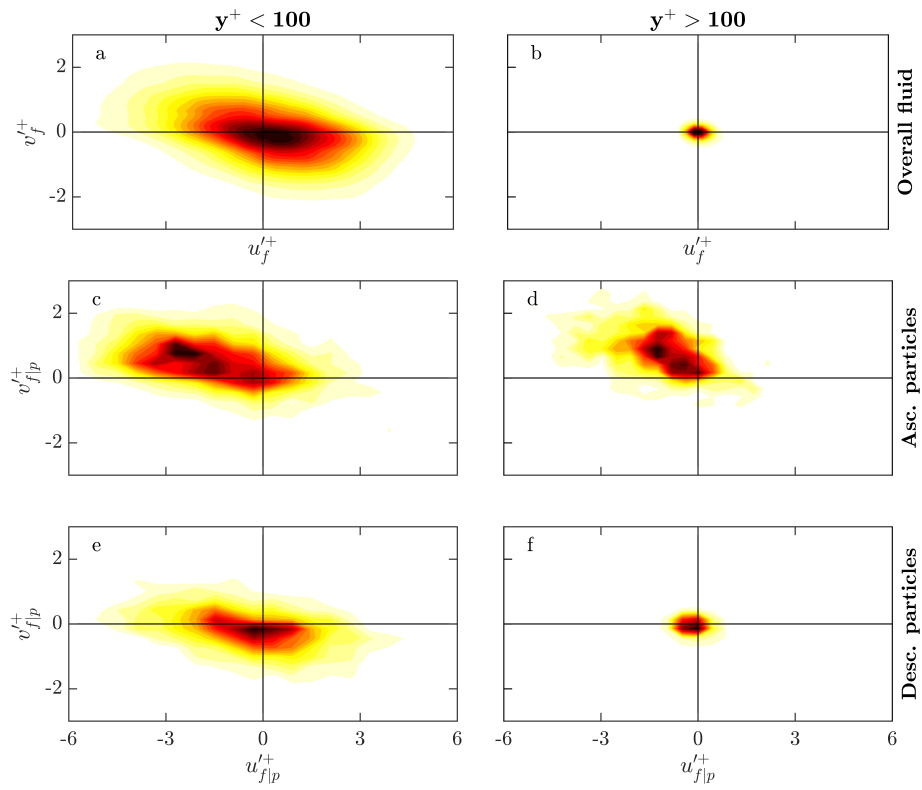


Figure 3.9: Joint PDFs of streamwise and wall-normal fluctuating fluid velocities for $y^+ < 100$ (a) and $y^+ > 100$ (b). Joint PDFs of streamwise and wall-normal fluctuating fluid velocities at particle locations for $y^+ < 100$ (c, e) and $y^+ > 100$ (d, f) conditioned on whether the particle is ascending (c, d) or descending (e, f).

2019; Berk & Coletti, 2020). In §3.6 we will show this to be the case also in the present configuration. Because the Rouse–Prandtl theory does not account for turbophoresis, we deduce the latter is not playing a significant role in the particle transport for the present conditions, despite St^+ being in the turbophoretic regime according to point-particle simulations without gravity (see, e.g., Bernardini, 2014). This could be partly due to the relatively large size of our particles, which influences the ability of inner-layer streamwise vortices to accumulate them at the wall. However, considering the findings of previous studies with much smaller particles (e.g., Berk & Coletti, 2020), the more likely reason is that gravitational drift disrupts the particle interaction with coherent turbulent motions.

3.5 Particle diffusion

The question of dispersion is central in particle-laden flows. A large body of experimental and numerical work in homogeneous turbulence has established that heavy particles disperse differently from tracers due to two distinct and competing effects. Particle inertia increases the integral time scale of their Lagrangian velocity autocorrelation, and hence their diffusivity, due to the finite response time (Squires & Eaton, 1991; Wang & Stock, 1993; Jung *et al.*, 2008). Meanwhile, particle drift due to gravity or other body forces causes them to cross fluid trajectories with consequent decorrelation of motion and reduction of diffusivity compared to tracers (Csanady, 1963; Squires & Eaton, 1991; Elghobashi & Truesdell, 1992; Wang & Stock, 1993). In wall-bounded flows, Lagrangian stochastic models have been proposed in order to predict dispersion of inertial particles (Tanière & Arcen, 2016; Marchioli, 2017) but have been mostly tested against point-particle numerical simulations, usually without gravity.

To address the issue of dispersion, we first consider the temporal coherence of particle motion by computing Lagrangian autocorrelations of the particle velocity (in these definitions we only refer to u_p for brevity, but all definitions apply to v_p as well):

$$\rho_{u_p}(\Delta t, y_0) = \frac{\langle u'_p(t_0, y_0)u'_p(t_0 + \Delta t, y_0) \rangle}{\langle u'^2_p(t_0, y_0) \rangle^{1/2} \langle u'^2_p(t_0 + \Delta t, y_0) \rangle^{1/2}}. \quad (3.3)$$

The subscript ‘0’ denotes the origin of a trajectory, so that t_0 and y_0 are the initial time

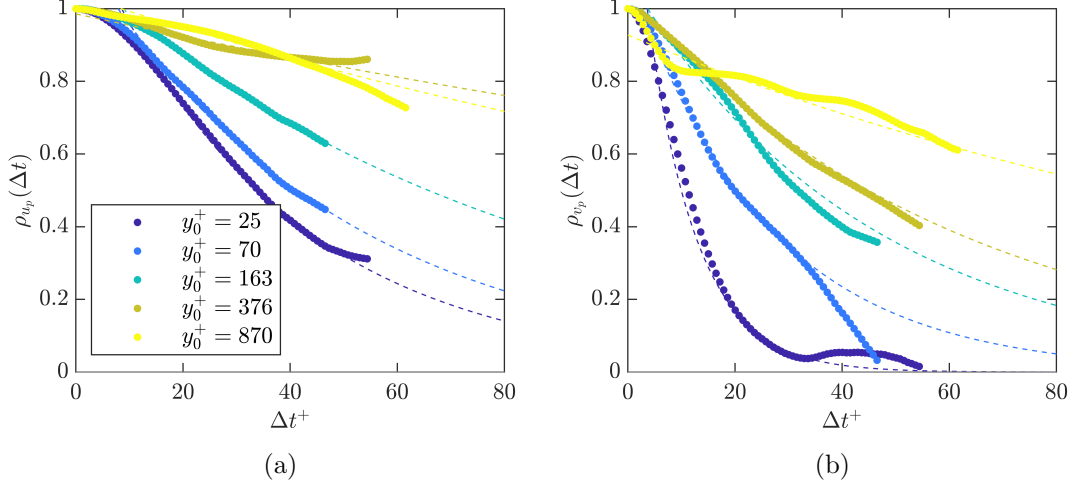


Figure 3.10: Lagrangian autocorrelations of streamwise (a) and wall-normal (b) particle velocity for five wall-normal bins (dots) shown with their respective exponential fits (dashed lines). The wall-normal locations listed in the legend correspond to the center of each bin.

and wall-normal location of each trajectory, respectively. Here the fluctuating velocities, u'_p , are determined by subtracting the Lagrangian mean velocity from each trajectory, $\langle u_p(\Delta t, y_0) \rangle_L$:

$$u'_p(t_0 + \Delta t, y_0) = u_p(t_0 + \Delta t, y_0) - \langle u_p(\Delta t, y_0) \rangle_L. \quad (3.4)$$

The Lagrangian autocorrelation is computed within five logarithmically spaced wall-normal bins, such that each contains a comparable number of samples. The autocorrelations of streamwise and wall-normal particle velocities are plotted in figure 3.10a and b, respectively. They both drop off more steeply near the wall, and the streamwise particle velocity remains correlated over a longer length of time than the wall-normal velocity. These trends are consistent with results for fluid tracers in channel flow simulations (Choi *et al.*, 2004). They are attributed to the smaller flow scales affecting the particle motion near the wall, and the streamwise-elongated structures that characterize the boundary layer, contributing to the turbulence anisotropy.

The integral time scale of the particle motions in streamwise and wall-normal directions can be defined as $\tau_{L,x} = \int_0^\infty \rho_{u_p}(\Delta t) d\Delta t$ and $\tau_{L,y} = \int_0^\infty \rho_{v_p}(\Delta t) d\Delta t$, respectively. Since in practice the integral can only extend to finite values, and recognizing that

ρ_{u_p} and ρ_{v_p} approximately follow an exponential decay, we fit an exponential function to the autocorrelations and consider the time lag that results in an e -fold drop of the exponential fit. Applying the theory of Taylor (1921) on the Lagrangian statistics of particle displacements, we evaluate the long-time particle diffusivities in both directions, $\varepsilon_{p,x} = \tau_{L,x} \langle u_p'^2 \rangle$ and $\varepsilon_{p,y} = \tau_{L,y} \langle v_p'^2 \rangle$. In figure 3.11 this is shown for the five wall-normal bins and for both velocity components, computed using the variance of the particle velocity within the respective bins. For comparison, we also plot the classic estimate for the fluid momentum diffusivity in the log-law region, $\varepsilon_f = \kappa y u_\tau$ (Prandtl, 1952), and that for the defect layer ($y > 0.2\delta_{99}$), estimated as $\varepsilon_f = 0.09\delta_{99}u_\tau$ (Pope, 2000). In the log-law region, the turbulence causes the particles to disperse much faster in the streamwise direction, greatly exceeding the momentum diffusivity. This indicates that the effect of particle inertia (which increases particle dispersion) is dominating over the effect of gravitational drift (which reduces it), at least in what pertains streamwise dispersion. This agrees with theoretical arguments of Reeks (1977) which predicted particles to disperse faster than tracers when the settling velocity $V_s < \langle u_f'^2 \rangle^{1/2}$, as it is the case here. Laboratory observations had confirmed this in homogeneous turbulence (Wells & Stock, 1983; Sabban & van Hout, 2011), and to our knowledge the present results are the first experimental observation of this effect in wall turbulence. On the other hand, $\varepsilon_{p,y}$ is equal to or smaller than the momentum diffusivity across the boundary layer, indicating that, in the vertical direction, the effect of gravity in decorrelating the particle motion slightly dominates.

3.6 Particle concentration and flux

Mean particle relative concentration as a function of wall-normal distance is plotted in figure 3.12. This is obtained by counting particles within logarithmically spaced wall-normal bins and normalizing by the mean concentration in the lowest bin, C_0 . The observed power-law behavior prompts a comparison with the concentration profile predicted by the theory of Rouse (1937) and Prandtl (1952). This follows from the balance between gravitational settling and wall-normal turbulent flux:

$$\langle C \rangle V_s - \varepsilon \frac{\partial \langle C \rangle}{\partial y} = \Phi \quad (3.5)$$

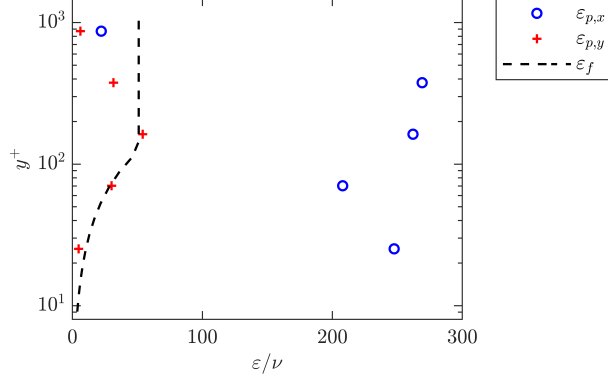


Figure 3.11: Wall-normal profiles of streamwise and wall-normal diffusivity (blue circles and red crosses, respectively) compared to the theoretical profile of fluid momentum diffusivity (black dashed line).

where V_s is the particle settling velocity and Φ is the net wall-normal flux of particles. Assuming equilibrium conditions ($\Phi = 0$), the particles falling at $V_s = V_t$ and having the same diffusivity as the momentum in the turbulent boundary layer ($\varepsilon = \kappa y u_\tau$), leads to the well-known concentration profile (Prandtl, 1952):

$$\frac{\langle C \rangle}{\langle C \rangle_{ref}} = \left(\frac{y}{y_{ref}} \right)^{-Ro} \quad (3.6)$$

where the subscript denotes an arbitrary reference height and the corresponding concentration. $Ro = -V_t/(\kappa u_\tau)$ is the Rouse number, which quantifies the relative strength of gravitational settling and turbulent resuspension of the particles. Equation 3.6 is also plotted in figure 3.12 for comparison, which shows a much steeper drop in concentration with height than the measurements. A departure from Rouse–Prandtl theory is expected, notably because the latter does not account for particle inertia. In particular, Berk & Coletti (2020) recently carried out a wind tunnel study of particle transport in turbulent boundary layers, and also reported a reduced slope of the concentration profile compared to the Rouse–Prandtl theory for a wide range of Stokes numbers. They hypothesized this to be due to a near-wall settling rate below the terminal velocity but could not accurately measure the particle vertical velocity. The present measurements corroborate their hypothesis (see figure 3.3b).

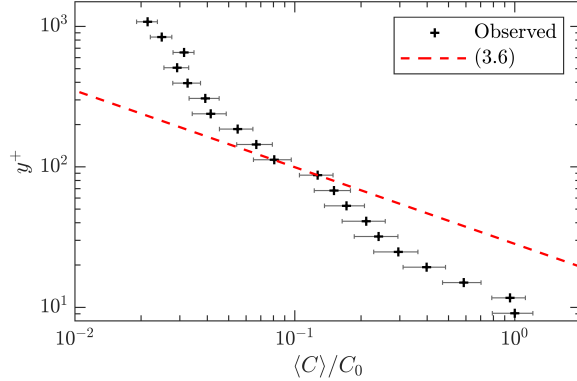


Figure 3.12: Wall-normal profile of mean particle concentration normalized by the concentration at the lowest wall-normal bin (black crosses). The power-law profile predicted by Rouse–Prandtl theory (red dashed line) is calculated from 3.6, where the arbitrary reference height is taken at $y_r^+ = 90$.

The particle streamwise mass flux Q_x is often of interest, especially in geophysical flows. Assuming advection dominates on the turbulent transport, the mean flux can be approximated from the mean concentration and mean velocity profiles, i.e. $\langle Q_x \rangle \approx \langle C \rangle \langle u_p \rangle$. Here we compute the flux directly by counting particles crossing wall-normal planes, and verify that it does not vary with streamwise location within the imaging window, and that it is indistinguishable from the mean advective flux $\langle C \rangle \langle u_p \rangle$. The profile in figure 3.13, albeit with experimental scatter, suggests a power-law behavior. In sediment transport and aeolian transport studies, the flux is often observed to decay exponentially with wall-normal height, thus identifying a characteristic length scale (e.g., Bagnold, 1941; Nishimura & Hunt, 2000; Guala *et al.*, 2008; Kok *et al.*, 2012). However, those processes are inherently different from the present one: they are characterized by beds of particles mobilized by the impact of other particles, with their transport largely concentrated in a ‘saltation layer’. The present case instead is governed by suspension, and as such it does not possess a specific length scale beyond those associated to the fluid turbulence.

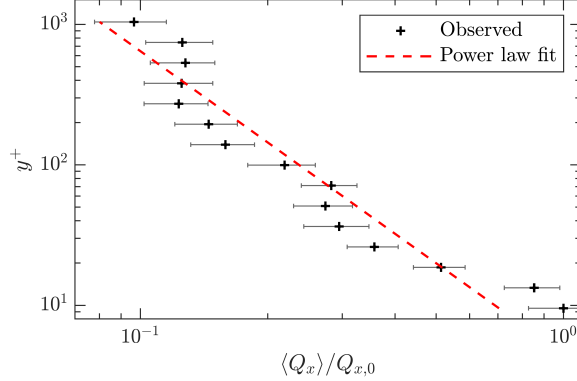


Figure 3.13: Wall-normal profile of particle streamwise mass flux normalized by the mass flux at the lowest wall-normal bin (black crosses), compared with a power law fit (red dashed line).

3.7 Particle acceleration

The statistics of the particle acceleration provide insight not only on the kinematics but also on the forces at play. In figure 3.14a we present the profiles of mean and r.m.s. acceleration for both in-plane components. The mean acceleration profiles are in close agreement with the recent experiments of Ebrahimian *et al.* (2019), who considered particles with $St^+ = 3.9$ and $D_p^+ = 6.8$ in a channel flow at $Re_\tau = 410$. The mean acceleration is negligible in the freestream, as expected in a fully developed flow. The streamwise acceleration increases to a positive maximum at $y^+ \sim 50$, and then rapidly decays to become negative near the wall. When expressed in wall units, the negative mean streamwise acceleration we observe near the wall is significantly smaller in magnitude compared with the experiments of Gerashchenko *et al.* (2008). These authors considered microscopic water droplets, and therefore the discrepancy is likely rooted in the larger size of our particles compared to the viscous length scale, and the consequent effect of forces other than drag and gravity (Maxey & Riley, 1983). The difference could also be related to particle interactions with the wall (addressed in §3.8), which were likely inconsequential for the statistics of Gerashchenko *et al.* (2008).

The mean wall-normal acceleration shows a qualitatively opposite trend compared to the streamwise component. At first, this would appear consistent with sweep and ejection being at the root of the acceleration profiles: upward vertical fluid fluctuations

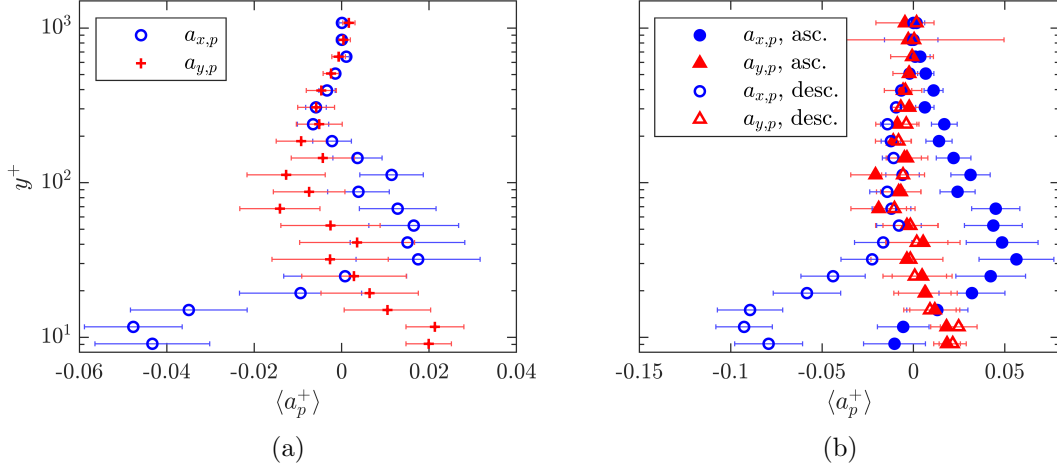


Figure 3.14: (a) Profiles of mean streamwise and wall-normal particle acceleration. (b) Profiles of mean streamwise and wall-normal particle acceleration conditioned on whether particles are ascending (filled symbols) or descending (open symbols).

lifting the particles away from the wall also tend to decelerate them in streamwise direction, and vice versa for downward fluctuations. This view, however, does not consider the fact that the mean velocity of the particles is downward: thus, negative wall-normal accelerations are mostly associated to a decrease in magnitude of the negative velocity, i.e., hindering of the settling. We shall come back to this point shortly, when considering the fluid events associated to these particle statistics.

In Gerashchenko *et al.* (2008) and Lavezzo *et al.* (2010) it was argued that the gravitational settling of particles through the shear flow plays a crucial role in determining the streamwise acceleration. To explore this issue, we condition again the statistics on ascending and descending particles (figure 3.14b). It becomes apparent that the regions of positive and negative streamwise acceleration can be attributed to the ascending and descending particles, respectively. This is in line with arguments presented by Gerashchenko *et al.* (2008) and Ebrahimian *et al.* (2019): particles that fall vertically find themselves surrounded by slower fluid, which decelerates them; and vice versa for particles moving vertically upward. The mean vertical acceleration is instead unaffected by conditioning on ascending/descending particles.

We present profiles of r.m.s. particle acceleration in figure 3.15. The streamwise

component is quantitatively close to what is reported by Gerashchenko *et al.* (2008), Zamansky *et al.* (2011), and Ebrahimiyan *et al.* (2019). The wall-normal component instead reaches a peak 30-60% larger than in those studies, being comparable to the streamwise component. We believe this to be mainly caused by gravitational effects. Already Gerashchenko *et al.* (2008) found that the particle r.m.s. acceleration of inertial particles was larger than that of tracer particles, in contrast with known trends in homogeneous turbulence (Bec *et al.*, 2006; Ayyalasomayajula *et al.*, 2006). Our particles are more inertial than those considered by Gerashchenko *et al.* (2008) (who had maximum $St^+ = 5.3$) and have larger settling velocity ($V_t/u_\tau = 0.75$, versus $V_t/u_\tau = 0.38$ in that study). In laboratory experiments it is not possible to conclusively disentangle inertia from gravity to determine what drives the higher vertical r.m.s. acceleration, but we can find hints in previous numerical studies where gravity could be suppressed. Lavezzo *et al.* (2010) demonstrated that gravity was the cause of increased r.m.s. acceleration in streamwise direction. This appears to be the case also for the wall-normal component, enhanced because the falling particles encounter rapidly changing flow structures. In further support of this view, the zero-gravity simulations of Zamansky *et al.* (2011) found a decrease of both components of r.m.s. acceleration with increasing St^+ , while the recent simulations of Lee & Lee (2019) that included gravity showed the opposite trend, in agreement with Gerashchenko *et al.* (2008). Taken together, the above indicates that it is gravitational drift that causes heavy particles to have large r.m.s. accelerations, in both streamwise and wall-normal directions.

The acceleration of fluid tracers and inertial particles in turbulence are known to be intermittent, with super-Gaussian probabilities of high-acceleration events that strongly depend on the particle inertia. When gravity is absent or has negligible influence, it is established that increasing Stokes number leads to reduced intermittency (Bec *et al.*, 2006; Gerashchenko *et al.*, 2008; Zamansky *et al.*, 2011). We present the PDF of streamwise and wall-normal accelerations in figure 3.16. We plot separately the distributions for particles below and above $y^+ = 100$, which helps in better understanding the observed behavior. The stretched exponential tails indicate significant intermittency, with relatively large probability of extreme events. This is, however, much stronger for the particles far from the wall than for those close to it: the flatness of the distributions for $y^+ > 100$ and $y^+ < 100$ is 5.5 and 20.5 for the streamwise component, and 6.4 and

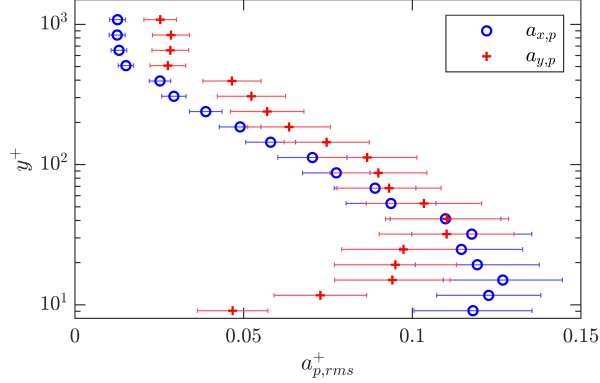


Figure 3.15: Wall-normal profiles of streamwise (blue circles) and wall-normal (red crosses) particle r.m.s. acceleration.

10.4 for the wall-normal component, respectively. This is because the particles closer to the wall interact with turbulent eddies of smaller time scales, and therefore have an effectively larger Stokes number (see figure 2.5a), which in turn causes them to ‘filter out’ intense fluid flow events (Bec *et al.*, 2006). The crossing-trajectory effect, on the other hand, is weaker for the near-wall particles, that have small mean vertical velocity (figure 3.3b). Combined with the results for the r.m.s. accelerations, these results underscore the competing influence of gravity and inertia: the first enhances the variance and intermittency of the particle accelerations, while the second damps them, the net result depending on the relative importance of both effects.

The particle trajectories are influenced not only by the instantaneous values of their accelerations, but also by their temporal coherence. This is explored by calculating the Lagrangian autocorrelation of streamwise particle accelerations, defined analogously to the velocity autocorrelations and presented in figure 3.17 for various wall distances. The wall-normal acceleration (not shown) follows similar trends, but less clearly so due to experimental uncertainty on measuring quantities of smaller magnitude. Close to the wall ($y^+ \lesssim 100$), the acceleration has significant temporal coherence, with the autocorrelation showing e -folding time of the order of the response time of the particles, before decaying monotonically to zero. This suggests that near-wall particles move in and out of streamwise-coherent turbulent structures and behave as if responding to step changes in the surrounding fluid velocity. We will show in §3.8 that this picture is

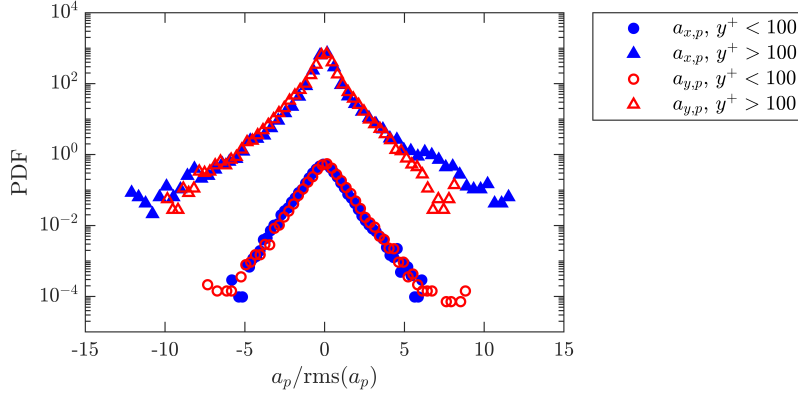


Figure 3.16: PDFs of streamwise (blue filled symbols) and wall-normal (red open symbols) particle acceleration conditioned on $y^+ < 100$ (circles) and $y^+ > 100$ (triangles). The PDFs for $y^+ > 100$ are shifted upward by a factor of 10^3 for clarity.

consistent with the behavior of the particles that directly interact with the wall. At larger heights, the temporal coherence is greatly reduced and the oscillations around zero suggest a quick alternation of positive and negative accelerations. This is likely caused by settling with significant speed (close to the particle terminal velocity for $y^+ \gtrsim 100$, see figure 3.3b), which cause the particles to move in a less coherent fashion. This is in line with the above-mentioned drop in streamwise diffusivity with increasing distance from the wall (figure 3.11).

3.8 Particle–wall interactions

In order to analyze the direct interactions with the wall, we consider the trajectories of particles that come in contact with it. An example of one such trajectory is shown in figure 3.18. Actual physical contact cannot be ascertained by the present imaging, and a lubrication layer is possibly maintained during those events. Still, we will use the word ‘contact’ to indicate the instances with no measurable wall-particle separation. More precisely, considering the variance of the particle diameters and the uncertainty in locating both the particles and the wall, we record contact when particle centroids are within 1.3 mean particle radii from the wall, i.e., when their wall-normal height is $y^+ \leq 10.4$. The results below are robust to small modifications of this threshold.

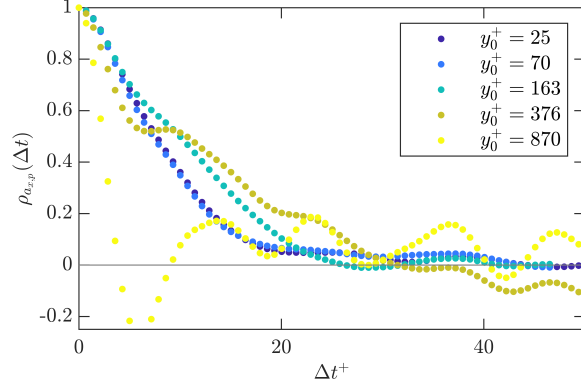


Figure 3.17: Lagrangian autocorrelation of streamwise particle acceleration for five wall-normal bins. The wall-normal locations listed in the legend correspond to the center of each bin.

We define ‘touch-down’ and ‘lift-off’ events when this threshold is crossed by particles approaching and leaving the wall, respectively. In figure 3.18, touch-down occurs at about $\tau^+ = 15$ and lift-off at about $\tau^+ = 40$; in between, the particle is considered to be in continued contact with the wall. Below we present results from averaging 241 trajectories leading to a touch-down and 151 trajectories following a lift-off.

First, particle-wall interactions are characterized in terms of duration of contact, t_{wall} . Figure 3.19 presents the PDF of t_{wall} in viscous units, which is well described by an exponential distribution. This is reminiscent of the distribution of ‘waiting times’ between touch-down and lift-off of the particles mobilized by the flow over a sediment bed (Einstein, 1950; Ancy *et al.*, 2006; Fan *et al.*, 2016). In the case of bedload transport, an exponential distribution follows from assuming that touch-down and lift-off are time- and space-invariant Markovian processes (Ancy *et al.*, 2006), i.e., independent events that are influenced only by the present and local state. Accordingly, waiting times have often been modelled as induced by a random (Poissonian) distribution of turbulent fluctuations having sufficient strength to mobilize the particles (e.g., Papanicolaou *et al.*, 2002). There are obvious differences between bedload transport and the present case: most notably, our particles are never at rest, as the wall shear stress exerted by the flow is much larger than the critical value for mobilizing them (Shields, 1936). Still,

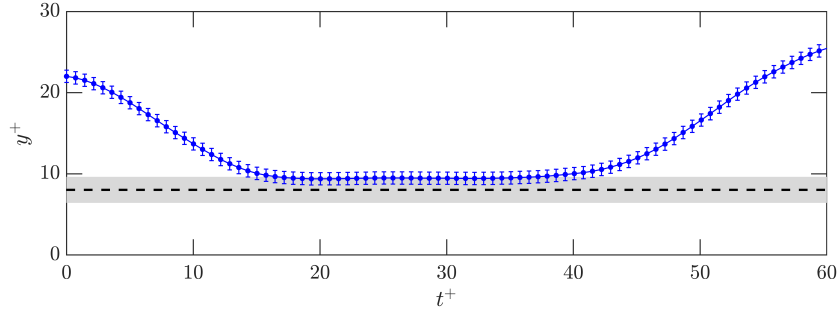


Figure 3.18: An example of an interaction between a particle and the wall. The blue curve shows the wall-normal distance of the particle centroid vs. time, with error bars representing the uncertainty in particle position. The dashed line represents a height of one particle radius above the wall, with the grey shaded region indicating the uncertainty in the particle radius and the wall location.

our distribution of contact times suggests these can be modelled by a similar stochastic process driven by randomly occurring fluid flow events above a certain threshold. We note that Cameron *et al.* (2020) recently showed the importance of very-large-scale motions (non-random, spatially correlated turbulent events) for sediment entrainment. While this points to the limitations of considering turbulent fluctuations to be random, their study was conducted at much higher Reynolds numbers for which very-large-scale motions are more prominent than in our case (Smits *et al.*, 2011).

The exponential distribution of t_{wall} suggests a characteristic time τ_{wall} , such that its duration probability can be approximated as $\text{PDF}(t_{wall}) \propto \exp\left(\frac{-t_{wall}}{\tau_{wall}}\right)$. A least-squares fit returns $\tau_{wall} = 13.5\tau^+$, which is remarkably close to the particle response time $\tau_p/\tau^+ = St^+ = 15$. This suggests that both particle inertia and the fluid fluctuations play a role in determining the duration of the wall contact, and one may hypothesize a scaling $\tau_{wall}^+ \sim St^+$. This is indeed consistent with the results reported by Ebrahimian *et al.* (2019), whose particles had $St^+ = 3.9$ and a mean wall contact time around $4\tau^+$. Because that is the only previous study reporting contact times for suspended particles, further research is warranted to corroborate this ansatz. We note that, in sediment transport, the waiting time was originally suggested by Einstein (1950) to be inversely proportional to the particle settling velocity, but it was later recognized that an inverse proportionality with fluid velocity showed better agreement with observations, and with

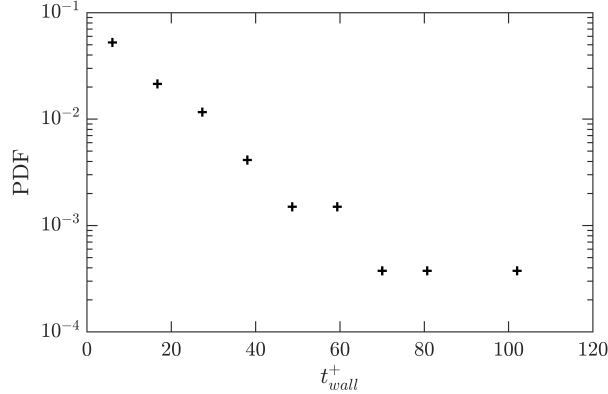


Figure 3.19: PDF of duration of particle-wall interactions, defined as the length of time particles spend continuously within 1.3 mean particle radii of the wall.

the view that the particle entrainment rate depends on the strength of the turbulent fluctuations (Ancy *et al.*, 2006, 2008).

As the particles are never at rest, one may consider the possibility that the short contact times are associated with a rebound process. However, even assuming an incident velocity V_i equal to the maximum vertical velocity in the $20\tau^+$ preceding touchdown (see below), the impact Stokes number $\rho_p V_i D_p / (9\mu)$ is of order unity—well below the threshold for a non-zero restitution coefficient (Joseph *et al.*, 2001; Gondret *et al.*, 2002). Thus, in the present regime, the kinetic energy of the particle associated to its wall-normal motion is expected to be dissipated at contact, with no effective rebound.

The particle-wall interactions can also be characterized by the angle θ_p of near-wall particle trajectories as they approach or recede from the wall. The trajectory angle is defined as $\theta_p = \text{atan}(v_p/u_p)$, such that θ_p is negative for particles approaching the wall and positive for particles receding from it. The set of particles within one particle diameter of the wall ($y^+ < 16$) is considered. The PDF of θ_p is shown in figure 3.20; it displays stretched tails (with a flatness of 6.7), and measurable preference for positive values (with a skewness of 0.65). The distribution of angles is narrower than what reported by Ebrahimian *et al.* (2019). This is attributed to the larger inertia of the present particles ($St^+ = 15$ versus 3.9), resulting in a slower response time to fluid velocity fluctuations and thus shallower near-wall trajectory angles. The positive skewness indicates that, despite gravity, relatively sharp lift-offs may occur.

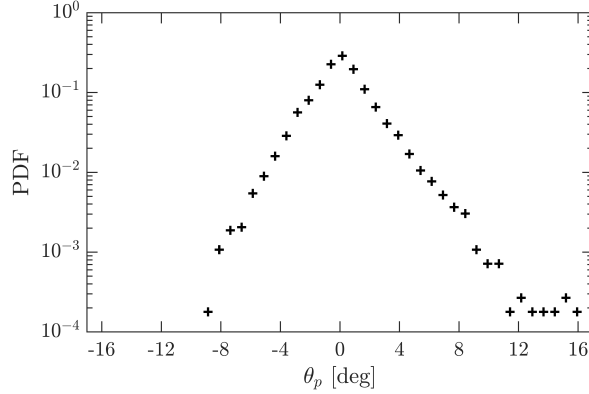


Figure 3.20: PDF of the angle of trajectories for near-wall ($y^+ < D_p^+$) particles.

The mechanisms behind particle touch-down and lift-off can be further understood by considering the Lagrangian averages along the particle trajectories. To this end, we first identify the moments of touch-down and lift-off (within the temporal resolution of $1/500 \text{ s} = 0.7\tau^+$), and then average over all trajectories leading to and following those events, respectively. Figure 3.21 displays the average particle wall-normal distance, streamwise velocity and vertical velocity during the $20\tau^+$ before touch-down and after lift-off. We do not report Lagrangian statistics during particle–wall contact, as the range of contact durations thwarts a consistent averaging process. However, we note that the wall-normal positions, velocities and accelerations at touch-down are very close to those at lift-off.

The Lagrangian averages of the wall-normal distance indicate that the particles descending to the wall follow a somewhat steeper trajectory than those ascending from it (figures 3.21a and b). This is confirmed by the plots of the vertical velocities (figures 3.21e and f) and is due to a combination of gravity and Saffman lift (which is directed downward, as demonstrated below). The streamwise velocity declines before touch-down (figure 3.21c), because the particles approaching the wall are surrounded by slower and slower fluid, which applies on them drag in the negative x-direction. After lift-off, although the particles ascend at a similar pace as they descended, they regain streamwise velocity much more slowly (figure 3.21d). This fits the view of particles being lifted from the wall by ejections, i.e., events with smaller streamwise fluid momentum compared to the local mean.

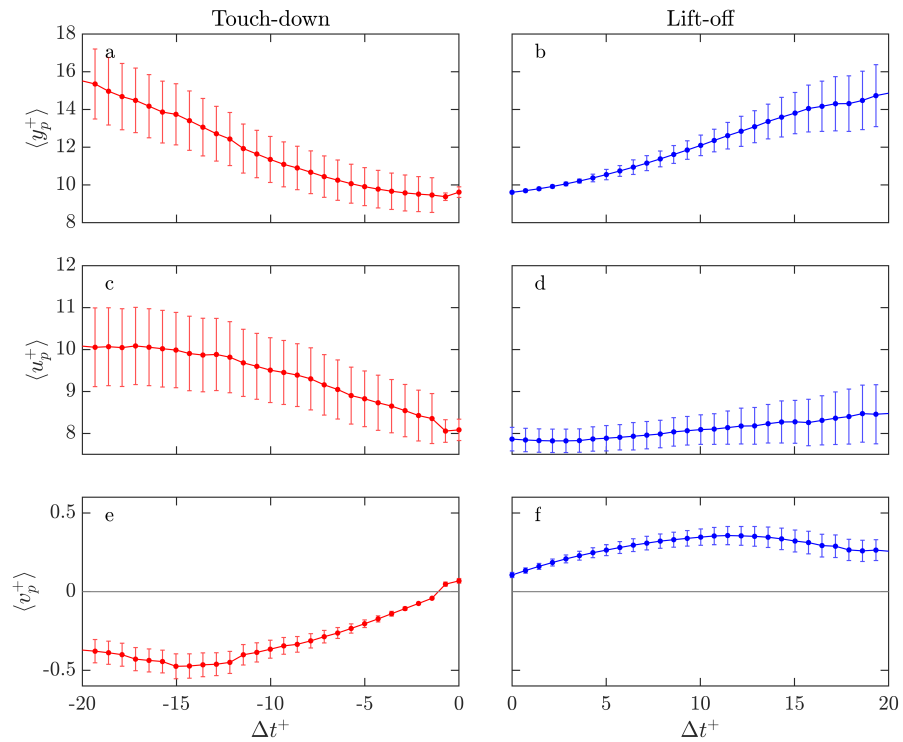


Figure 3.21: Lagrangian means of particle wall-normal coordinate (a, b), streamwise velocity (c, d), and wall-normal velocity (e, f) averaged over all identified touch-down events (a, c, e) and lift-off events (b, d, f). The time axis shows the time interval before or after lift-off or touch-down, respectively, and $\Delta t^+ = 0$ represents the moment of lift-off or touch-down.

The Lagrangian average of the fluid velocity experienced by the particles along their trajectory helps in the interpretation of the above trends. Figures 3.22a and b show that, before and after wall contact, the streamwise velocity of the fluid surrounding the particles is significantly lower than the local particle velocity (see figure 3.21c and d). (This is not captured by the unconditioned mean profiles presented §3.1 and §3.2. We remark that the particles coming in contact with the wall are a small fraction of the total in the corresponding bin.) The direction of the streamwise slip velocity implies that, close to wall contact, drag acts against the direction of motion and Saffman lift is directed downward (in consideration of the slip velocity and the fluid velocity gradient, Saffman, 1965). The streamwise fluid velocity along the trajectory is also significantly lower than the local mean fluid velocity (assuming a canonical boundary layer profile, see figure 3.1); therefore, the particles are in regions of negative streamwise fluctuations. Because the vertical fluid velocity is negative before touch-down (figure 3.22c) and positive after lift-off (figure 3.22d), particles approaching and leaving the wall experience Q3 events and Q2 events, respectively. This confirms once more that ejections (in Q2) are critical to lift particles from the wall, while the role of sweeps (in Q4) is not dominant near wall contact. Importantly, figure 3.22d indicates that the vertical fluid velocity becomes positive just as the particles leave the wall: that is, lift-off happens when the particle starts to experience a fluid ejection. This is in line with the view that the duration of the contact time is dictated by the occurring of turbulent events.

A material frame of reference attached to the particles is the most appropriate to investigate the forces acting on them, and thus we now consider the accelerations tangential and normal to the local trajectory, $a_{t,p}$ and $a_{n,p}$, respectively:

$$a_{t,p} = a_{x,p} \cos(\theta_p) + a_{y,p} \sin(\theta_p) \quad (3.7)$$

$$a_{n,p} = a_{y,p} \cos(\theta_p) - a_{x,p} \sin(\theta_p) \quad (3.8)$$

Note that since θ_p is relatively small, the tangential and normal accelerations are very similar in magnitude to the horizontal and vertical components, respectively. We can make inferences on the role and respective importance of drag, gravity, and Saffman lift. Other forces are expected to be important as well, such as added mass, fluid

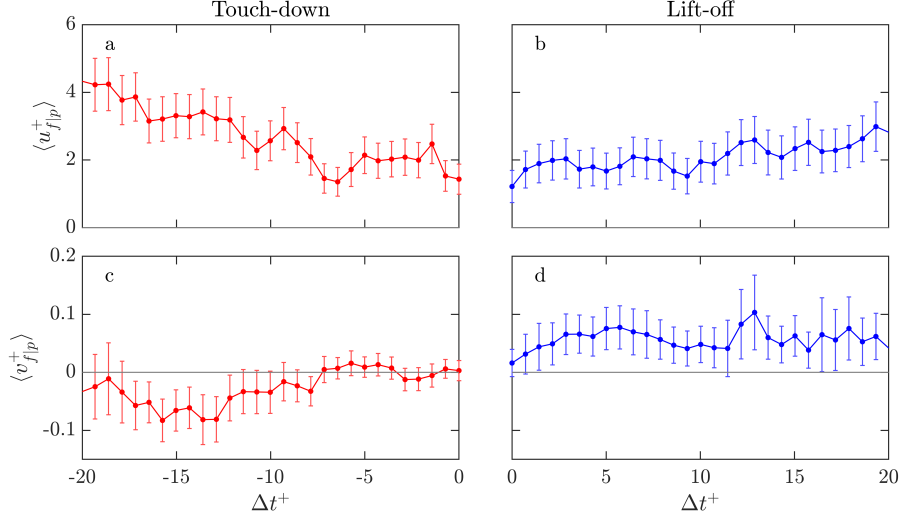


Figure 3.22: Lagrangian means of streamwise (a, b) and wall-normal (c, d) fluid velocity at particle location averaged over all identified touch-down events (a, c) and lift-off events (b, d). The time axis shows the time interval before or after lift-off or touch-down, respectively, and $\Delta t^+ = 0$ represents the moment of lift-off or touch-down.

acceleration, Basset history and Faxén corrections, and rotation-induced (Magnus) lift (Maxey & Riley, 1983; Crowe *et al.*, 2011; Mathai *et al.*, 2019); however, it is not trivial to infer their behavior from experimental data, so most of our qualitative considerations will not focus on these forces.

The Lagrangian averages of the accelerations before and after wall contact are plotted in figure 3.23. As the particles approach the wall before touch-down, they experience increasingly negative tangential acceleration (figure 3.23a), reflecting the drag force opposing their motion. Notice that, while we are outside the assumptions of viscous steady flow made to derive analytical results, we expect the wall proximity to enhance drag for a particle moving parallel to a solid boundary (Brenner, 1965). The negative streamwise acceleration peaks around $5\tau^+$ before touch-down and then decreases in magnitude. This is possibly due to lubrication effects, as the average particle is then only a fraction of its diameter away from the wall. Higher resolution measurements are needed to draw firm conclusions in this regard.

As the particles leave the wall and reach faster fluid layers, they at first experience

negative streamwise acceleration, but this shrinks in magnitude and eventually reaches a small positive plateau (figure 3.23b). This follows from the particles being entrained into faster fluid strata, which reduces the negative drag. However, because the particles are still faster than the surrounding fluid (see figures 3.21d and 3.22b), the drag is expected to remain negative. Thus, the positive streamwise acceleration must be a consequence of other forces. Added mass and fluid acceleration force are prime candidates, because the acceleration of the fluid along the particle trajectory is positive and larger than that of the particle (compare again figures 3.21d and 3.22b). Further studies to quantify these forces are warranted.

The normal acceleration becomes positive before touch-down (figure 3.23c) since the downward particle velocity is decreasing in magnitude as the wall is approached. This is qualitatively consistent with the increase in drag predicted in viscous flows when a particle travels towards a wall (Brenner, 1965). The interaction with a lubrication layer may also contribute to slowing down the descent. The downward-directed Saffman lift increases the magnitude of the downward particle velocity before touch-down and decreases the magnitude of the upward velocity after lift-off. Thus, Saffman lift (along with gravity) is the likely cause of the drop in positive normal acceleration after the particles have left the wall (figure 3.23d). Simulations of Lee & Balachandar (2010) suggested the Magnus force to be relatively small, but the estimates of Ebrahimian *et al.* (2019) suggested it could be sufficient to overcome gravity. Here the magnitude of the Magnus force cannot be estimated without knowing whether the particles are actually in contact with the wall, as this would dictate their rolling motion.

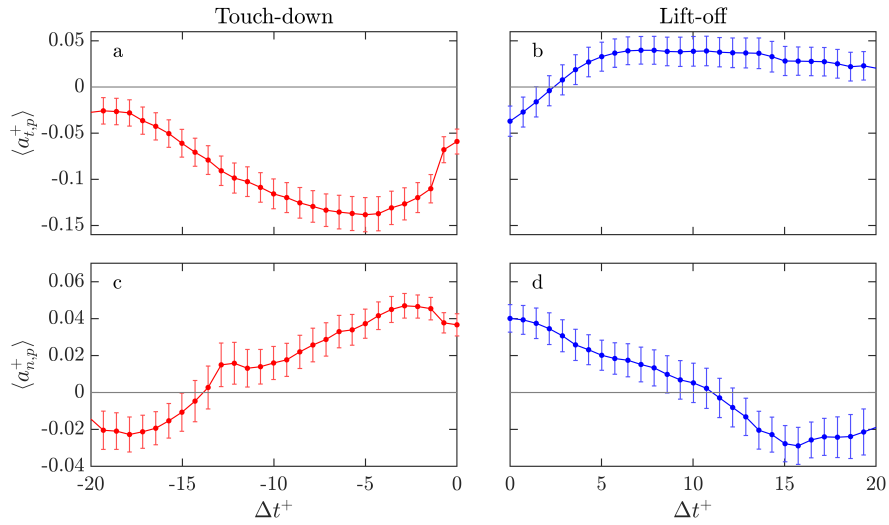


Figure 3.23: Lagrangian means of particle tangential acceleration (a, b) and normal acceleration (c, d) averaged over all identified touch-down events (a, c) and lift-off events (b, d). The time axis shows the time interval before or after lift-off or touch-down, respectively, and $\Delta t^+ = 0$ represents the moment of lift-off or touch-down.

Chapter 4

Non-spherical particle results

4.1 Fluid and particle velocity and acceleration

4.1.1 Velocity statistics

We first consider the translational statistics of the particles and fluid. Rod and disk results are compared with those of the spherical particles from Chapter 3.

Wall-normal mean profiles of streamwise and wall-normal particle and fluid velocities are shown in figure 4.1. The deviation of the streamwise velocity profiles of the sphere case in the freestream region is due to its slightly higher freestream velocity. Within the boundary layer, the mean velocities are not drastically different between the particle shapes, confirming point-particle simulation results (Challabotla *et al.*, 2015; Njobuenwu & Fairweather, 2016). In all cases, particles lag the fluid within the logarithmic layer due to their inertia. However, streamwise velocity does differ between particle types near the wall, with the disk velocity significantly larger than that of the rods.

We investigate the particle slip velocity to understand these trends. The total mean slip velocity can be decomposed into two components, as follows:

$$\langle u_p \rangle - \langle u_f \rangle = \langle u_p - u_{f|p} \rangle + \langle u_{f|p} \rangle - \langle u_f \rangle \quad (4.1)$$

where $\langle u_p - u_{f|p} \rangle$ is the mean of the local slip velocity, and $\langle u_{f|p} \rangle - \langle u_f \rangle$ is the apparent slip velocity. The local slip velocity quantifies the actual slip that each particle experiences relative to the surrounding fluid; the apparent slip velocity reflects preferential

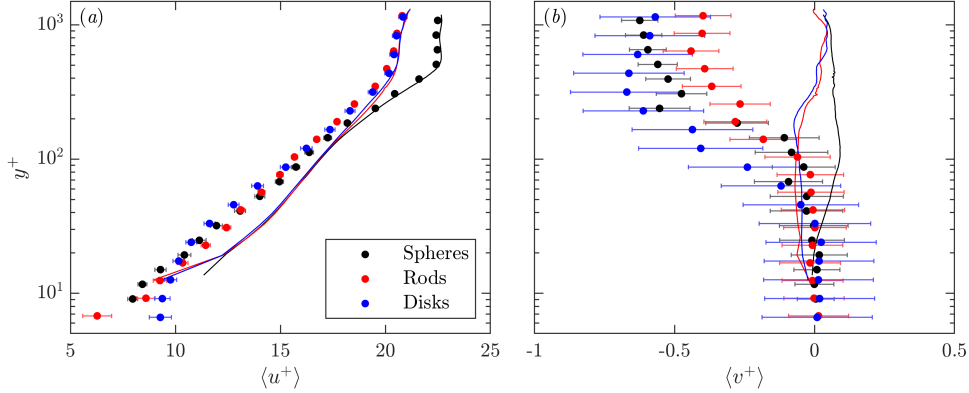


Figure 4.1: Wall-normal profiles of mean streamwise (a) and wall-normal (b) particle (circles) and fluid (lines) velocity, compared between sphere (black), rod (red), and disk (blue) particles.

sampling of slower- or faster-than-average fluid (Kiger & Pan, 2002). The streamwise and wall-normal slip velocities are shown in figure 4.2. Note that fluid velocity, and therefore slip velocity, is not available below $y^+ \approx 11$ due to the limited PIV resolution.

From the streamwise slip velocity (figure 4.2a), it is observed that disks and rods particles oversample faster-moving fluid regions, as evidenced by their positive apparent slip velocity, below $y^+ \approx 30$, suggesting that particles accumulate in high-speed streaks. This preferential sampling is stronger for the rods and disks than for the spheres, whose apparent slip only slightly exceeds zero at the wall. Oversampling of high-speed streaks confirms the findings of PR-DNS and experimental studies (Do-Quang *et al.*, 2014; Shaik *et al.*, 2020). In the outer region up to $y^+ \approx 400$, the apparent slip for spheres is negative, while for rods and disks it is much closer to zero. The local slip velocity for all three particle shapes is negative for the entire channel depth and becomes more negative as particles approach the wall, indicating that the particles lag the surrounding fluid on average. This is consistent with the expected behavior of inertial particles. Disks and rods lag the surrounding fluid by a greater amount than the spheres, possibly suggesting that they have a larger effective drag or inertia. This would not contradict the fact that the spheres have a larger nominal St^+ , because St^+ of the disks and rods is calculated assuming an isotropic orientation distribution; as we will see in §4.2.1, the

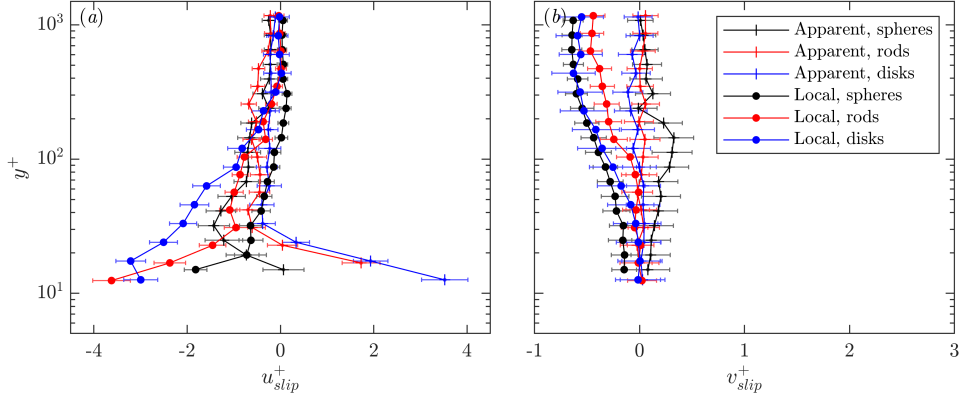


Figure 4.2: Wall-normal profiles of streamwise (a) and wall-normal (b) mean slip velocities for spheres (black), rods (red) and disks (blue). The apparent slip velocity component is shown in crosses, and local component is shown in circles.

actual orientation distribution is not isotropic.

The wall-normal slip velocity profiles (figure 4.2b) reveal further differences between the particle shapes. All three particle shapes have negative local slip velocities in the outer region due to gravitational settling, which decay as they approach the wall due to the effects of turbulent resuspension and the physical constraint of the wall. However, spheres slightly oversample upward-moving fluid on average, as evidenced by the positive apparent slip, but rods and disks do not show this behavior; their apparent slip is near zero throughout the channel depth. This may be attributed to the spheres oversampling negative streamwise fluid velocity fluctuations, which are correlated with positive wall-normal fluid velocities in a turbulent boundary layer; while these behavior is not exhibited by rods or disks, which in fact show a strong tendency to oversample regions for positive streamwise fluid velocity fluctuations.

The Reynolds stresses of the fluid and particles are compared in figure 4.3. Rods have slightly higher $\langle u'^2 \rangle$ near the wall than spheres or disks, and the non-spherical particles have slightly a lower $\langle v'^2 \rangle$ peak than spheres. The greatest differences show up in the profiles of $\langle u'v' \rangle$: the shape of the profile for the rods is similar to that of the spheres, but the magnitude is lower, following the shear stress of the fluid very closely. For the disks, the shape of the profile is significantly different: the shear stress is much

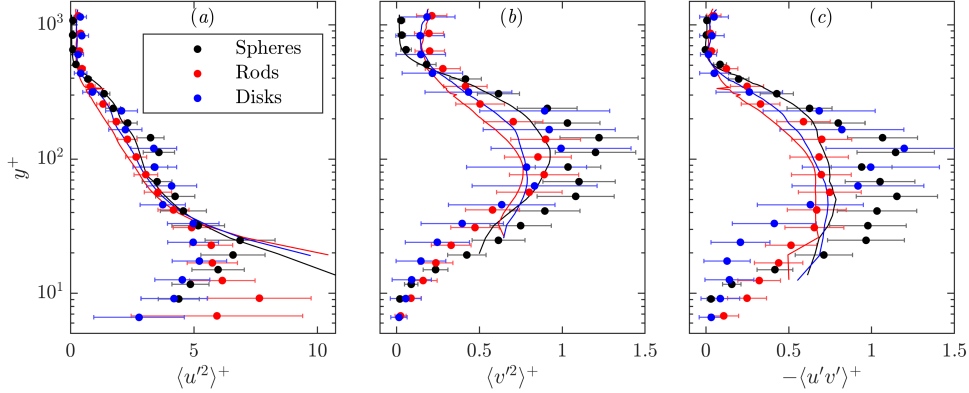


Figure 4.3: Wall-normal profiles of streamwise (a), wall-normal (b), and shear (c) stresses for particles (circles) and fluid (lines).

lower near the wall, and the peak is shifted higher in the boundary layer than either the rods or spheres. The increased particle stresses of the spheres was attributed to the effect of particle trajectories crossing fluid streamlines due to the particle inertia (Chapter 3). That the stress profiles of the rods largely match the shape of the spheres', but are lower in magnitude, may reflect reduced streamline crossing effects and therefore lower particle inertia of the rods. On the other hand, the disk Reynolds stress profiles differ in shape more than magnitude, suggesting a more complex interaction with the fluid turbulence.

The differences in velocity variance raises the question of shape effects on the temporal coherence of the particle velocity, which is explored using Lagrangian autocorrelations. Autocorrelations are calculated within four logarithmically-spaced wall-normal bins to capture trends in different parts of the boundary layer and freestream. Lagrangian autocorrelations of streamwise and wall-normal particle velocity for each particle shape are presented in figure 4.4. The streamwise velocity of the disks near the wall is found to be coherent for a much longer time than it is for either spheres or rods, but in the outer region the autocorrelations decay at similar rates for all three shapes. This observation is in line with the finding that disks have reduced $\langle u'v' \rangle$ near the wall, and seem to indicate that disks are less responsive to turbulent fluctuations, which would decorrelate the disks' motion, compared to rods or spheres. However, the

autocorrelations of wall-normal particle velocity decay at similar rates for all three particles throughout the boundary layer and freestream regions. If the disks’ insensitivity to turbulence was due to their inertia alone, we would expect the autocorrelations of v_p to decay slowly as well. Since they do not, we hypothesize that orientation-dependent resistance is the more likely cause. The patterns observed in the autocorrelations are consistent with disks that preferentially orient with $|p_y| \sim 1$, i.e., flat and level, which we will confirm to be the case in §4.2.1. Disks oriented this way sustain their streamwise momentum for much longer than their wall-normal momentum, because their streamwise drag is much lower than their wall-normal drag. Lower drag corresponds to both reduced damping and reduced sensitivity to high-frequency turbulent fluctuations, both of which would result in a longer time of coherent motion. That this behavior is not observed in rods may be a consequence of the rods’ geometry: due to their thin shape, the particle area on which drag acts does not change as much with particle orientation.

4.1.2 Particle acceleration statistics

Particle accelerations are considered to investigate the dynamics of particle motion. Wall-normal profiles of mean and RMS accelerations in the streamwise and wall-normal directions are shown in figure 4.5. No significant difference is observed in the mean acceleration profiles between particle shapes: near the wall, particles tend to have negative $\langle a_{x,p} \rangle$ as they fall into slower fluid, being occasionally slowed further down by direct contact with the wall; while the positive $\langle a_{y,p} \rangle$ near the wall is attributed to turbulent resuspension. On the other hand, the RMS accelerations show some shape effects. RMS accelerations for both x and y components are lowest for disks, with the RMS of $a_{x,p}$ in particular much lower than that of rods or spheres. It is established that the magnitude of particle RMS acceleration decreases with increasing particle inertia for spheres; this has also been confirmed for prolate ellipsoids using point-particle DNS (Ouchene *et al.*, 2018). The reduction of disks’ RMS acceleration further indicates that drag and/or inertia reduces the disks’ responsiveness to fluid motions, reducing their acceleration variability. Rods have a lower RMS of $a_{y,p}$ than spheres, but their RMS of $a_{x,p}$ is similar in magnitude to that of spheres, implying that the rods’ wall-normal RMS acceleration may be preferentially attenuated through the orientation dependence of fluid drag.

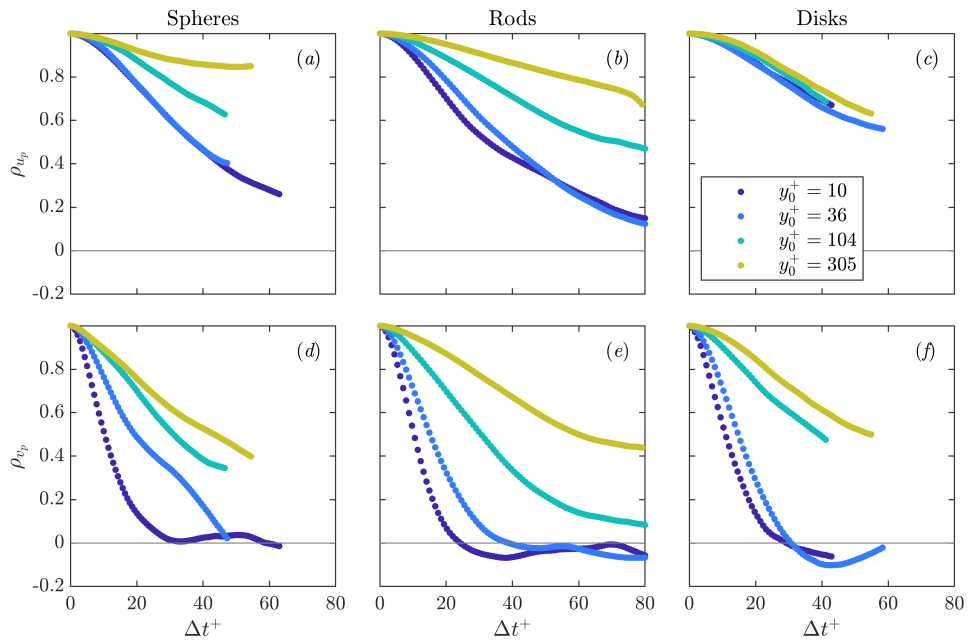


Figure 4.4: Lagrangian autocorrelations of u_p (a-c) and v_p (d-f) for spheres (a, d), rods (b, e) and disks (c, f) calculated within four wall-normal bins.

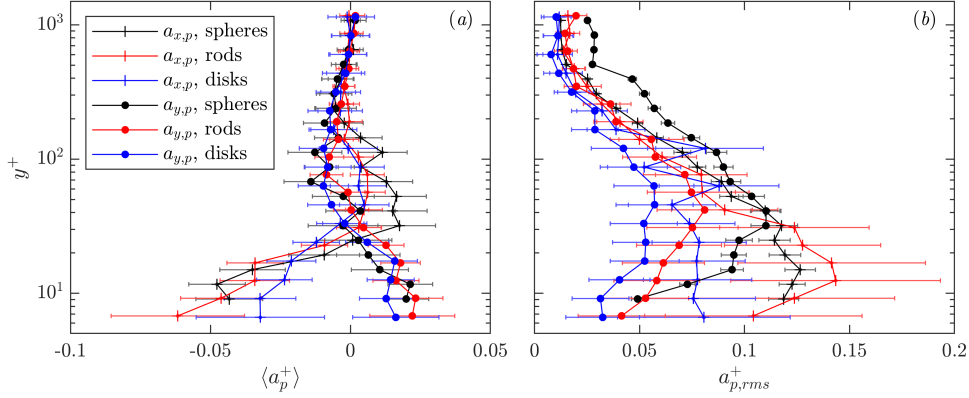


Figure 4.5: Wall-normal profiles of mean (a) and RMS (b) particle acceleration for spheres (black), rods (red), and disks (blue). Streamwise acceleration is shown in crosses, and wall-normal acceleration is shown in circles.

4.2 Particle orientation and tumbling

4.2.1 Orientation statistics

We then examine the distribution of particle orientations. PDFs of each component of the particle orientation vector, p_x , p_y and p_z , are shown in figure 4.6, separated by particle wall-normal position into two bins with $y_p^+ < 100$ and $y_p^+ > 100$. Recall that the range of p_x and p_z is $[0, 1]$, and the range of p_y is $[-1, 1]$. Disk and rod particles have generally opposite preferential orientations. For the near-wall set of particles, rods tend to align their symmetry axis \mathbf{p} with the streamwise direction (as signaled by the high probability of p_x being often close to unity), whereas disks align \mathbf{p} with the vertical axis (indicated by the high absolute values of p_y being often close to unity). Both particle types have some level of preferential alignment with the spanwise axis as well, as indicated by preferential values of $p_z > 0$. Disks show a preference towards p_y slightly greater than -1 and rods towards p_y slightly greater than 0, which both correspond to a slightly “nose-up” configuration. In the set of particles far from the wall, rods exhibit a much weaker alignment with the streamwise direction and a stronger alignment with the vertical and spanwise directions, indicating an increase in their isotropy. In contrast, disks in the outer region strongly align their symmetry axis with the vertical axis,

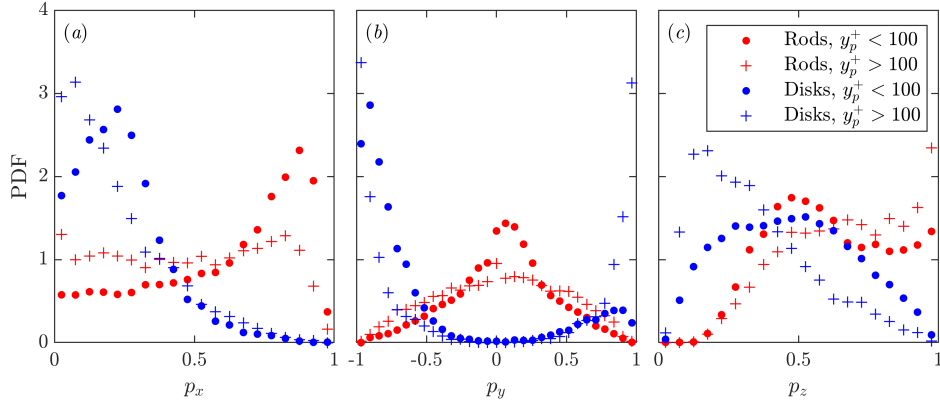


Figure 4.6: PDFs of particle orientation components p_x (a), p_y (b), and p_z (c) for rods (red) and disks (blue) with $y_p^+ < 100$ (circles) and $y_p^+ > 100$ (crosses).

corresponding to a strong preference for a flat and level orientation. The streamwise alignment of the rods and their return to isotropy in the outer region agrees with the results of several point-particle simulations (Zhao *et al.*, 2015; Yuan *et al.*, 2017; Zhao *et al.*, 2019). However, the alignment of the disks differs from what is found in the point-particle simulations of Challabotla *et al.* (2015) and Zhao *et al.* (2015), which found that inertial disk particles preferentially align with the spanwise axis near the wall.

4.2.2 Statistics of tumbling rate and tumbling acceleration

Mean profiles of the squared tumbling rate $\dot{\mathbf{p}}\dot{\mathbf{p}}$ and squared tumbling acceleration $\ddot{\mathbf{p}}\ddot{\mathbf{p}}$ as a function of wall-normal distance are plotted in figure 4.7. In the outer region of the channel, the profiles are nearly the same for disks and rods. However, the behavior of disks and rods diverge below $y^+ \sim 100$. The squared tumbling rate and squared tumbling acceleration for disks peak around $y^+ \sim 40$, below which both quantities drop off and approach zero. In contrast, rod particles are much more mobile: their squared tumbling rate and acceleration are much larger than that of disks as y^+ goes to zero.

Further insight can be gained by separating the tumbling rate components by component. Figure 4.8 shows mean profiles of $\omega_{t,z}$ and RMS profiles of all three tumbling

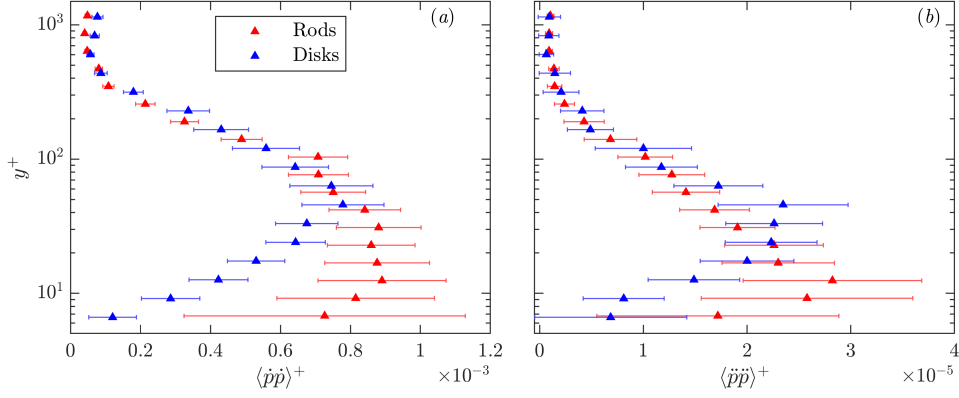


Figure 4.7: Wall-normal profiles of mean squared tumbling rate (a) and mean square tumbling acceleration (b) for rods (red) and disks (blue).

rate components. Rods have a greater negative $\langle \omega_{t,z} \rangle$ (matching the sense of the mean shear) than disks in the the boundary layer, which contributes to their larger squared tumbling rate. The RMS tumbling rate provides a better measure of the magnitude of the other two components, because their mean is zero due to the spanwise symmetry of the channel. Rods have high RMS values of $\omega_{t,y}$ in the inner region, which also contributes to their squared tumbling rate, especially very close to the wall. On the other hand, all components of disk tumbling rates approach zero near the wall.

PDFs of squared tumbling rate $\dot{\mathbf{p}}\dot{\mathbf{p}}$ and squared tumbling acceleration $\ddot{\mathbf{p}}\ddot{\mathbf{p}}$ are compared between particle types for near-wall and outer-region particles in Figure 4.9. The distributions of both $\dot{\mathbf{p}}\dot{\mathbf{p}}$ and $\ddot{\mathbf{p}}\ddot{\mathbf{p}}$ have very long tails, reflecting the high intermittency of tumbling events the particles experience. Rods are found to have higher frequencies of extreme $\dot{\mathbf{p}}\dot{\mathbf{p}}$ events than disks near the wall, but no difference is observed between rods and disks for $\ddot{\mathbf{p}}\ddot{\mathbf{p}}$ or particles far from the wall.

A more detailed picture is obtained by splitting the total tumbling rate into tumbling angular velocity components, $|\omega_{t,x}|$, $|\omega_{t,y}|$, and $\omega_{t,z}$ (the sign of the x and y tumbling components are ambiguous, so the absolute values are presented). PDFs of these are shown in figure 4.10. While all three components are larger for the near-wall particles, we observe that the excess tumbling events experienced by near-wall rods show up most strongly in $|\omega_{t,y}|$, whereas for near-wall disks the excess is mostly in $|\omega_{t,x}|$. $\omega_{t,z}$ is the

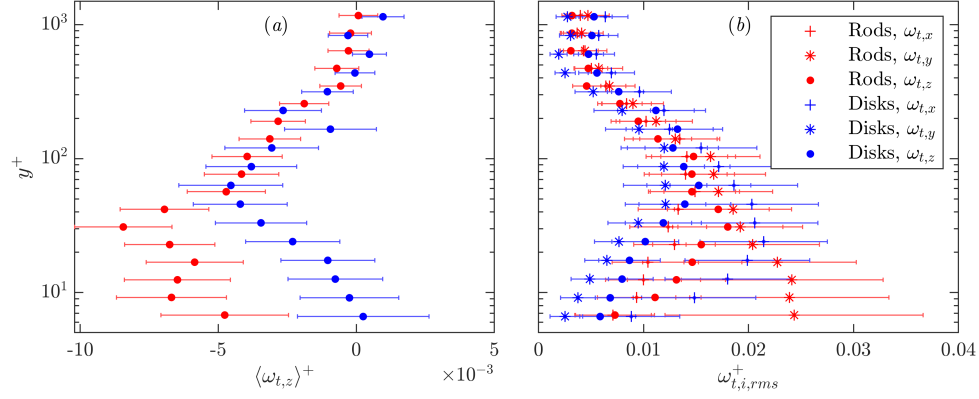


Figure 4.8: Wall-normal profiles of mean $\omega_{t,z}$ (a) and RMS tumbling rates of all three components (b) for rods (red) and disks (blue).

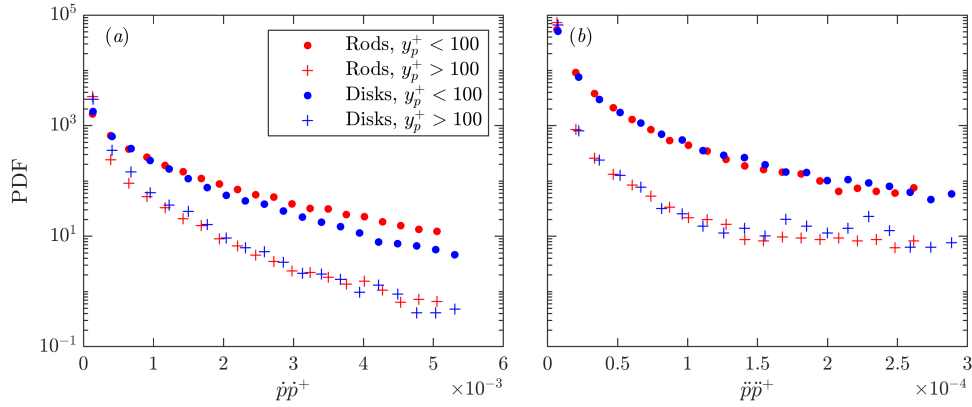


Figure 4.9: PDFs of particle squared tumbling rate (a) and squared tumbling acceleration (b) for rods (red) and disks (blue) with $y_p^+ < 100$ (circles) and $y_p^+ > 100$ (crosses).

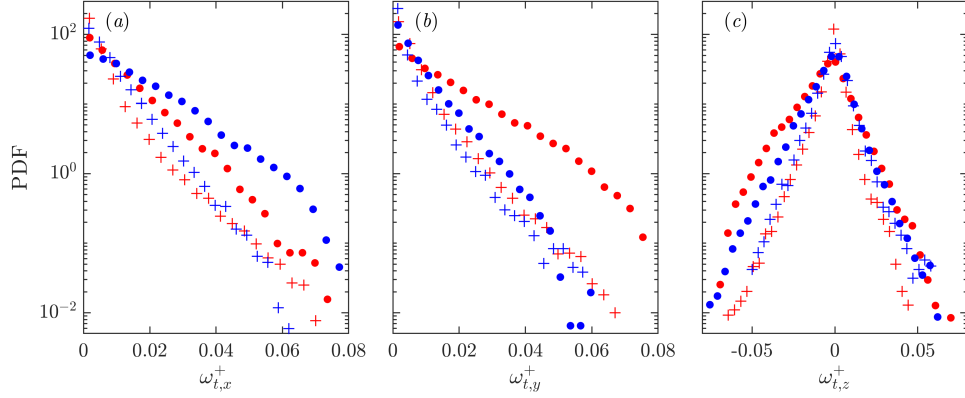


Figure 4.10: PDFs of tumbling angular velocity components, $|\omega_{t,x}|$ (a), $|\omega_{t,y}|$ (b), and $\omega_{t,z}$ (c) for rods (red) and disks (blue) with $y_p^+ < 100$ (circles) and $y_p^+ > 100$ (crosses).

component associated with rotation due to the mean shear, but the large PDF tails for the other components indicate that the particles are responsive to turbulent fluid motions acting in other directions.

By examining PDFs of tumbling angular acceleration components, we can better understand the influences behind particle tumbling (figure 4.11). The PDFs for particles with $y_p^+ > 100$, where the turbulence is weaker, are nearly the same for rods and disks. For the z component, the distribution of tumbling angular acceleration is also identical between particle shapes. Taken together with the PDF $\omega_{t,z}$ in figure 4.10c, rods appear to sustain a larger $\omega_{t,z}$, but not larger $\alpha_{t,z}$. This indicates the cause of the excess $\omega_{t,z}$ for rods is the mean shear, which would not be associated with particularly strong $\alpha_{t,z}$ events due to its steadiness. In contrast, the near-wall disk and rod particles show similar patterns in the tumbling acceleration PDF tails as in the tumbling rate PDFs, with rods having larger $|\alpha_{t,y}|$ than disks and disks having larger $|\alpha_{t,x}|$ than rods. That the trends show up in the tumbling acceleration as well as the tumbling rate indicates that the high tails are due to intermittent events, which could either be passing turbulent structures or interactions with the wall.

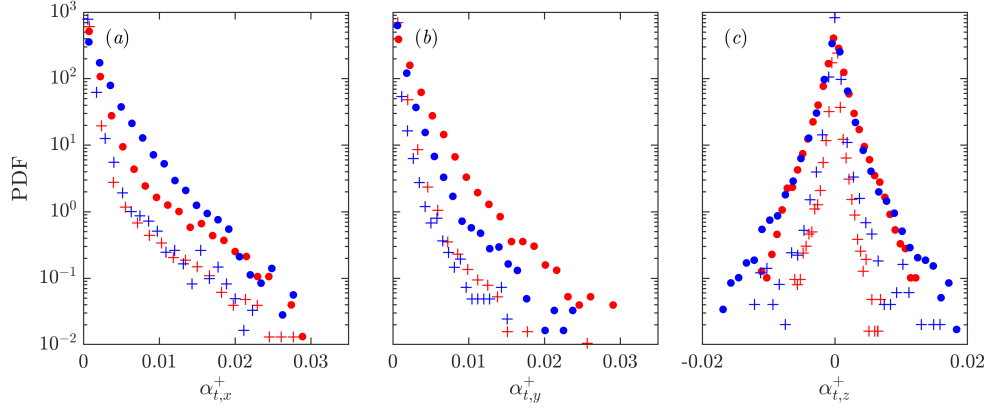


Figure 4.11: PDFs of tumbling angular acceleration components, $|\alpha_{t,x}|$ (a), $|\alpha_{t,y}|$ (b), and $\alpha_{t,z}$ (c) for rods (red) and disks (blue) with $y_p^+ < 100$ (circles) and $y_p^+ > 100$ (crosses).

4.2.3 Temporal coherence

We now consider the coherence of the particle orientation and tumbling in time using Lagrangian autocorrelations. Figure 4.12 shows the Lagrangian autocorrelations of particle p_x and p_y for rods and disks, calculated within in four logarithmically-spaced wall-normal bins. Overall, the autocorrelation curves of p_x and p_y for the rod particles are much more sensitive to wall-normal distance than for the disks, showing much more spread between bins close to and far from the wall compared to disks. This suggests that rods are more responsive to intermittent small-scale turbulent events occurring near the wall that induce tumbling. For p_y in particular, disks show a remarkable amount of temporal coherence, with very slowly decaying autocorrelations. This translates into relatively stable disk orientations across the channel depth in flat and level or slightly tilted configurations, whereas rods display stability in the freestream region but have more variable orientations nearer to the wall. This supports the findings in Marchioli *et al.* (2010) that prolate particles have a preferred streamwise orientation, but this orientation is unstable near the wall due to the wall-normal velocity gradient.

We then turn to the autocorrelations of spanwise tumbling rate $\omega_{t,z}$ (figure 4.13) to investigate the temporal coherence of tumbling motion. The disk autocorrelations

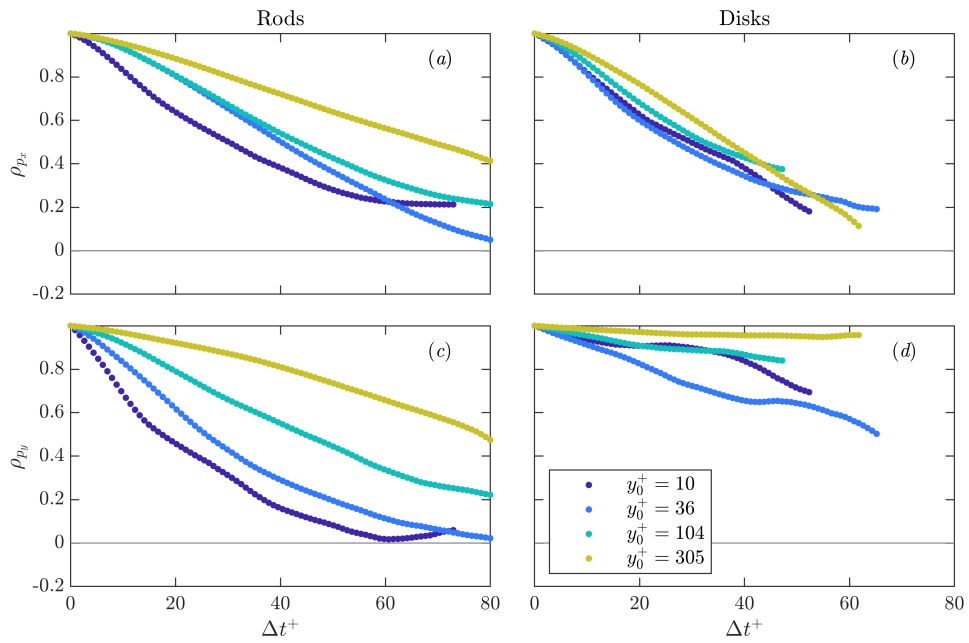


Figure 4.12: Lagrangian autocorrelations of p_x (a, b) and p_y (c, d) for rods (a, c) and disks (b, d) calculated within four wall-normal bins.

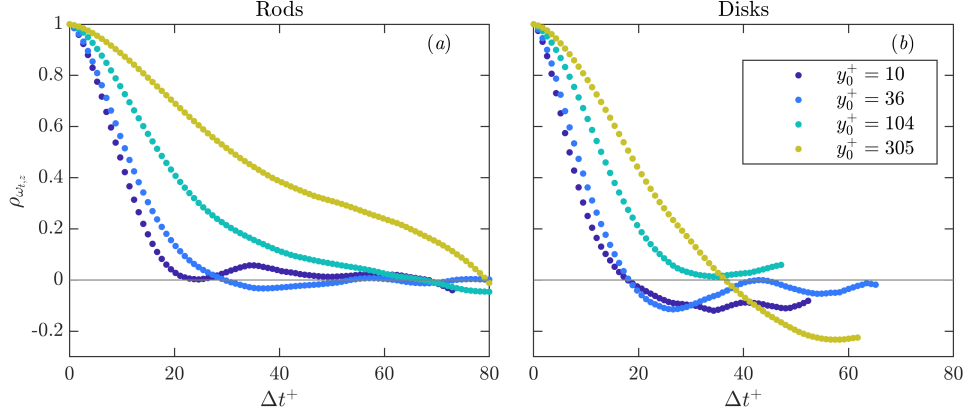


Figure 4.13: Lagrangian autocorrelations of $\omega_{t,z}$ for rods (a) and disks (b) calculated within four wall-normal bins.

are found to decay faster than those of rods at all wall-normal distances, which is the opposite of what was found in the autocorrelations of p_y . This confirms that disks tend to wobble about their preferential orientation, which causes their tumbling rate to vary over short time scales, rather than tumble end-over-end as the rods do. That the $\omega_{t,z}$ autocorrelations decay faster at lower y^+ implies that turbulence is still an important driver of both disk and rod tumbling motion.

4.2.4 Wall interactions

One mechanism for particle tumbling near the wall is particle interactions with the wall itself. Due to the particles' extended dimensions and finite slip velocity, friction due to contact or near-contact (lubrication) with the wall could exert significant torques on particles. To isolate the effect of wall contact, we consider particles located within one semimajor axis length from the wall and compare between those that are contacting the wall and those that are not. Wall contact is inferred when the lower edge of a particle coincides with the wall within measurement uncertainty. While this definition does not necessarily guarantee wall contact, it does capture particles that are close enough to the wall to feel its friction, either through contact or lubrication. Figure 4.14 shows PDFs of squared tumbling rate (a) and squared tumbling acceleration (b), compared

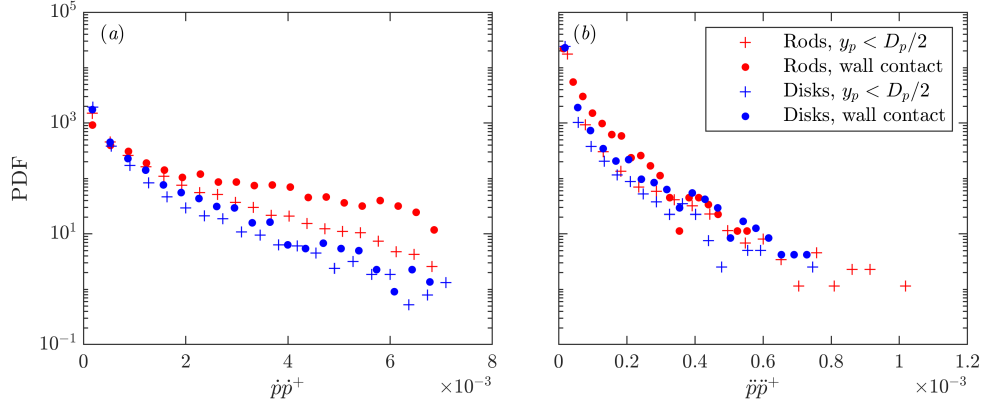


Figure 4.14: PDFs of squared tumbling rate (a) and squared tumbling acceleration (b) for rods (red) and disks (blue) within $D_p/2$ of the wall which are not contacting the wall (crosses) and are in contact with the wall (circles).

between wall-contacting and non-contacting disks and rods with $y_p < D_p/2$. A clear excess of extreme tumbling events is observed in the set of particles contacting the wall for both shapes. Rods have a greater increase in the frequency of extreme tumbling rate events for wall-contacting particles than do disks, suggesting that rods tumble more in response to wall friction. This makes sense if the resistive torque exerted by the fluid on the rods is less than that experienced by disks, which is expected since the disks have a much larger wetted area.

The above PDFs are then broken down into tumbling rate and acceleration components, and the same sets of particles are compared again to investigate the mechanics of wall-friction tumbling events (figure 4.15). As expected, extreme tumbling rates and accelerations of several components are more frequent for wall-contacting particles than non-contacting particles. However, the tumbling behavior about the various axes is not entirely expected. Wall-contacting rod particles are found to have strong tumbling rates and accelerations more frequently about the spanwise axis than non-contacting rods, but also about the wall-normal axis. This implies that wall interactions induce a tilted “pole-vaulting” or “kayaking” mode of tumbling in rod particles. This may be due to the influence of spanwise shear due to high- and low-speed streaks, as found by Wang *et al.* (2018). Disks in contact with the wall, on the other hand, show stronger tumbling

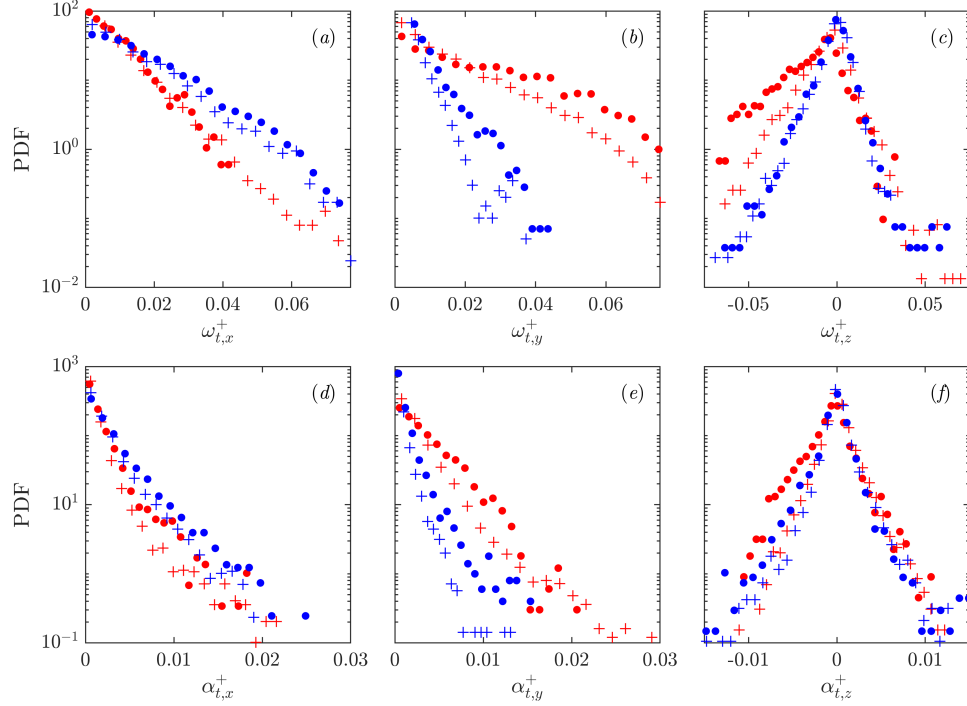


Figure 4.15: PDFs of tumbling rate (a-c) and tumbling acceleration (d-f) components for rods (red) and disks (blue) within $D_p/2$ of the wall which are not contacting the wall (crosses) and are in contact with the wall (circles).

about the wall-normal axis, and to a smaller degree the streamwise axis, but not the spanwise axis. This suggests that wall friction does not induce disks to tumble end-over-end, as it does rods. Instead, the mode of disk tumbling during wall interactions could be described as wobbling and precessing, like a top. This mode of tumbling is likely to result from the disks “nose-up” preferential orientation, which does not put the disks in a position to have their front edge contact the wall. Their point of contact is much more likely to be on the rear or side edges, which would produce a torque more in line with the x and y axes.

4.3 Particle spatial distribution and dispersion

4.3.1 Particle concentration profiles

Finally, we explore particle spatial distribution, transport, and dispersion. Concentration of heavy particles in turbulent boundary layers is determined by a balance between gravitational settling and turbulent resuspension. This balance can be derived from the Reynolds decomposition of the net particle flux, given by

$$\Phi = \langle C \rangle V_s + \langle C' v_p' \rangle \quad (4.2)$$

where Φ is the net wall-normal flux, C is the concentration, and V_s is the settling velocity of particles. The assumption of Fickian diffusion allows the balance to be written as the advection-diffusion model

$$\Phi = \langle C \rangle V_s - \varepsilon_p \frac{d\langle C \rangle}{dy} \quad (4.3)$$

where ε_p is the particle diffusivity. Assuming that: (i) equilibrium conditions are achieved ($\Phi = 0$), (ii) particles settle at their quiescent fluid terminal velocity ($V_s = V_t$), and (iii) the particle diffusivity is equal to the turbulent eddy diffusivity ($\varepsilon_p = \varepsilon_f = \kappa u_\tau y$), one can derive the following well-known concentration profile (Prandtl, 1952):

$$\frac{\langle C \rangle}{\langle C \rangle_{ref}} = \left(\frac{y}{y_{ref}} \right)^{-Ro} \quad (4.4)$$

where y_{ref} is an arbitrary reference height, $\langle C \rangle_{ref}$ is the corresponding concentration, and $Ro = -V_t/(\kappa u_\tau)$ is the Rouse number which quantifies the relative strength of gravitational settling and turbulent resuspension. Mean wall-normal profiles of particle concentration are shown in figure 4.16, compared with Rouse-Prandtl theory, and theoretical values of Ro as calculated above for each particle type are reported in table 4.1.

The spheres show a large deviation from the theoretical profile, which in Chapter 3 was attributed to their inertia and a near-wall settling velocity being less than V_t . In contrast, the concentration profiles for rods and disks agree with Rouse-Prandtl theory in the range $30 < y^+ < 200$, despite their finite size and inertia; above and below

Particle type	Spheres	Rods	Disks
Ro	1.83	1.13	1.62

Table 4.1: Theoretical particle Rouse numbers $Ro = -V_t/(\kappa u_\tau)$.

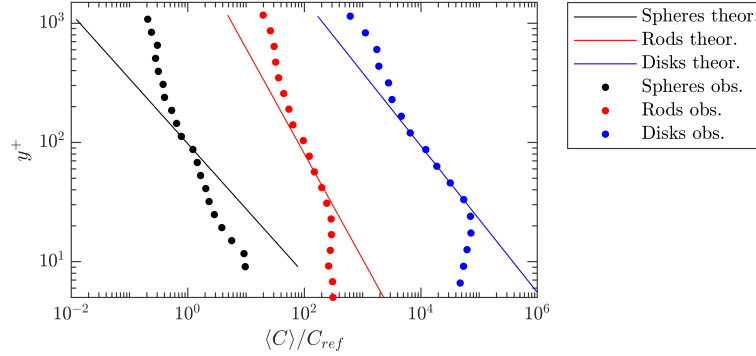


Figure 4.16: Wall-normal profiles of mean particle concentration for spheres (black), rods (red), and disks (blue) compared to the Rouse-Prandtl theory of equation 4.4 (lines). Concentration is normalized by its reference value at $y_p^+ = 100$. Each profile is shifted horizontally by a factor of 10^2 for clarity.

that range, however, the deviation becomes apparent. An assessment of Rouse-Prandtl theory for inertial spherical particles is explored in depth in Berk & Coletti (2020). The concentration profiles of disks and rods in the present experiment are similar to those of intermediate- Ro spherical particles ($Ro \sim 1$) in their study, with a concentration deficit near the wall and an excess in the freestream, while the concentration profile of the spheres in the present experiments corresponds with the higher- Ro particles ($Ro \sim 2$) in Berk & Coletti (2020). They showed that these deviations could be explained as a consequence of the particles' decreasing settling velocity approaching the wall and a small but non-zero net flux in the outer region, while the assumptions of Fickian diffusion and $\varepsilon_p = \kappa u_\tau y$ were tenable. We have already seen that the mean particle wall-normal velocity does decrease with wall-normal distance, lending confidence that the same arguments likely apply to rod and disk particles.

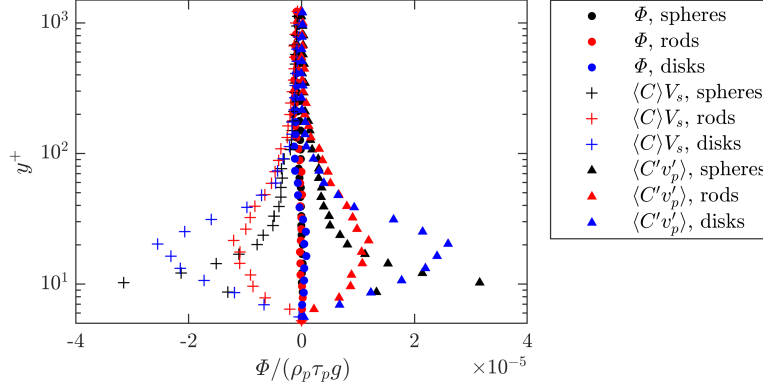


Figure 4.17: Wall-normal profiles of the particle flux terms in equation 4.2 for spheres (black), rods (red), and disks (blue). The net flux Φ is shown with circles, $\langle C \rangle V_s$ is shown with crosses, and $\langle C'v'_p \rangle$ is shown with triangles.

4.3.2 Particle flux and diffusivity

The above conclusions are confirmed further upon inspection of the wall-normal particle flux and direct estimation of the particle diffusivity. First, the three wall-normal flux terms from equation 4.2 are estimated. Φ is computed by counting particles as they cross horizontal planes spaced logarithmically in y , $\langle C \rangle V_s$ is calculated by directly multiplying the mean concentration profile by the particle terminal velocity, and $\langle C'v'_p \rangle$ was estimated as the difference of the two. These flux terms are shown as a function of y in figure 4.17. There is indeed a small but non-zero net flux in the outer region of the flow, as was the case in the experiments of Berk & Coletti (2020). The fluctuating flux term $\langle C'v'_p \rangle$ differs significantly between the particle shapes, with a much sharper peak for spheres which occurs closer to the wall than that of the rods and disks.

To investigate particle dispersion, we will estimate the diffusivity as a function of y in two different ways. The first way is to directly solve for ε_p in equation 4.3, relying on the assumption of Fickian diffusion. Solving for the diffusivity yields

$$\varepsilon_{p,flux}(y) = \frac{-\langle C'v'_p \rangle}{d\langle C \rangle/dy}. \quad (4.5)$$

This formula is applied only to the regions where the mean concentration decreases with

y . The second method does not rely on any diffusivity models. Instead, diffusivity is estimated from the integral timescale of the particles' wall-normal velocity autocorrelation T_{v_p} and the wall-normal velocity variance, using the theory of Taylor (1921):

$$\varepsilon_{p,ac}(y) = T_{v_p} \text{var}(v_p). \quad (4.6)$$

Due to the limited trajectory lengths of the particles, the integral timescale is estimated to be the e-folding time of an exponential function fitted to the autocorrelation (see figure 4.4). These particle diffusivity estimates are compared with two estimates of the fluid diffusivity: the first from Prandtl theory for a canonical boundary layer, given by

$$\varepsilon_{f,Pr} = \begin{cases} \kappa u_\tau y & \text{for } y < 0.2\delta_{99} \\ 0.09\delta_{99}u_\tau & \text{for } y > 0.2\delta_{99} \end{cases} \quad (4.7)$$

and the second a direct estimation of the eddy viscosity, given by

$$\varepsilon_{f,\nu_T} = \left| \frac{\langle u'v' \rangle}{d\langle u \rangle/dy} \right|. \quad (4.8)$$

The particle and fluid diffusivity profiles are presented in figure 4.18. The scatter of $\varepsilon_{p,flux}$ is very large, but it nevertheless is of the same order as the fluid diffusivity over the range where the mean concentration profile follows the theoretical prediction, $\langle C \rangle \propto y^{-Ro}$, in figure 4.16. On the other hand, the profiles of $\varepsilon_{p,ac}$ follow the fluid diffusivity profiles remarkably closely. The calculation of diffusivity from integral quantities instead of derivative quantities is less subject to measurement noise, making $\varepsilon_{p,ac}$ a more accurate estimator. It also does not rely on the Fickian assumption. This supports the assumption made in equation 4.4 that particle diffusivity is equal to the fluid diffusivity, at least for these particles which have $St^+ \sim O(10)$. The fact that the diffusivity calculated from the particle flux is somewhat similar to both $\varepsilon_{p,ac}$ and the fluid diffusivity within a limited range also implies that positing $\langle C'v_p' \rangle = -\varepsilon_p \frac{d\langle C \rangle}{dy}$ is reasonably justified and acts as an independent confirmation of the validity of the Fickian diffusion assumption over this range.

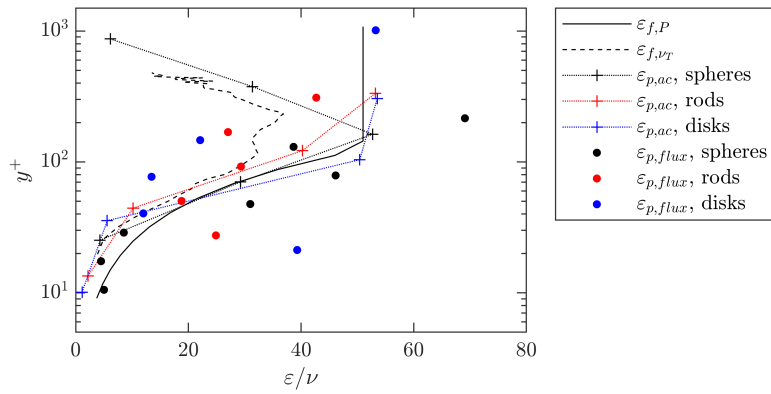


Figure 4.18: Wall-normal profiles of estimated fluid and particle diffusivities for spheres (black), rods (red), and disks (blue). Solid black line corresponds to Prandtl diffusivity, dashed black line to eddy viscosity, crosses to particle diffusivity based on the autocorrelation, and circles to particle diffusivity based on the particle flux.

Chapter 5

Conclusions

5.1 Spheres

We have investigated the transport of inertial particles suspended in a turbulent boundary layer through simultaneous fluid and particle velocity measurements. While the considered regime is especially relevant to geophysical water flows, we have taken a fundamental viewpoint and focused on the seemingly simple case of monodispersed spherical particles not depositing over the smooth wall. Leveraging the time-resolved, two-phase nature of the measurements, we documented in detail the particle-fluid dynamics and delved in several central aspects of this archetypical configuration. Given the richness of the flow physics, we chose to limit our attention to one specific regime, leaving parametric studies for the future.

We confirm that the particles travel at a lower mean velocity than the fluid, at least above the viscous sublayer. In the past, this has largely been attributed to the oversampling of slow velocity regions. While this is found to be the dominant factor in the logarithmic layer, closer to the wall the main cause for the mean velocity defect is the instantaneous particle slip from the surrounding fluid. Indeed, the expectation that particles would have a small instantaneous slip velocity is only tenable for small particle inertia and/or slow turbulence fluctuation, i.e., for small Stokes numbers. In the present regime ($St^+ = 15$), a significant portion of the fluid fluctuations experienced by the near-wall particles have shorter time scales than τ_p , and the inability of the particles to respond to them naturally translates in a sizeable slip velocity. By inspecting the

profiles conditioned on ascending and descending particles, it appears that the mean velocity lag is due to the ascending ones, thus it is not directly related to gravity. The mean vertical velocity of the particles is close to the quiescent-fluid terminal velocity in the freestream, but it becomes vanishingly small approaching the wall. This is an effect of oversampling upward turbulent fluctuations, which is opposite to the behavior in homogeneous turbulence.

The near-wall particle diffusivity in the streamwise direction is larger than the momentum eddy diffusivity, while the opposite is true in the wall-normal direction. This is one of the several instances in which the distinct (and competing) effects of gravity and inertia are on display. The dichotomy is highlighted here both by conditioning the statistics on ascending and descending particles, and by comparing outer and inner layers. This helps reconcile contrasting results in the literature and underscores the importance of both effects in realistic situations.

The near-wall particle transport is strongly linked to ejection events that promote resuspension, while the link with sweep events is weak. This suggests that turbophoresis, which is often considered a dominant feature according to studies where gravity is either absent or acting parallel to the wall, is at best a second-order effect when gravity is wall-normal. Under equilibrium between settling and turbulent suspension, the concentration profile follows a power-law with a much more gradual decrease from the wall than predicted by the Rouse–Prandtl theory (which neglects particle inertia), consistent with the observed reduction of settling velocity. While the particles in the inner layer do interact with the wall, the absence of bedload is reflected in the lack of a saltation layer in the mass flux profile.

Separating ascending and descending particles also helps us understand the root of the mean acceleration profile. Regions of positive and negative streamwise acceleration can be attributed to ascending and descending particles, respectively. Ascending particles find themselves surrounded by slower fluid which decelerates them (and more so because they are strongly associated with ejections); while descending particles are in the opposite condition, although this is due to gravity and not sweeps. By comparing with previous studies, we confirm that acceleration variance is larger for heavier particles, in stark contrast with the well-known trend in homogeneous turbulence. This is strictly a consequence of the crossing trajectories effect caused by gravitational drift,

rather than by inertia. Indeed, near the wall, where the gravitational drift is smaller and the local St_η is larger, the accelerations are much less intermittent than further away from the wall.

Contrasting the effects of gravity and inertia is important to estimate the trends in different regimes. If the same particles are suspended in a turbulent boundary layer at higher Reynolds numbers, for example, the near-wall turbulence time scales will become smaller. Thus, the Stokes number (encapsulating the effect of inertia) will grow; while the friction velocity will increase, and so the Rouse number (representing the relative importance of gravitational drift) will shrink. Our conclusions then provide indications on the expected trends in such a case: the particles would lag the fluid more markedly; the settling rate would decrease; the particle Reynolds stresses would be even larger than the fluid's; the particle diffusivity would increase (the streamwise component becoming increasingly larger than the eddy diffusivity, and the vertical component getting closer to it); the concentration profile would get flatter; and the acceleration variance and intermittency would decrease. Future parametric studies are warranted to verify these predictions.

The duration of the wall-particle contact follows an exponential distribution, suggesting an analogy with the waiting times between deposition and entrainment in sediment transport: after touch-down, the particles slide along the wall (possibly over a lubrication layer we cannot resolve) until fluid fluctuations of sufficient strength lift them back into the stream. When expressed in wall units, the time scale of wall contact (i.e., the inverse of the entrainment rate) is close to St^+ , in line with our interpretation of the process: a balance between particle inertia and fluid turbulence. The Lagrangian average along the trajectories before and after wall contact indicate that the particles descend more steeply towards the wall than they recede from it, due to a combination of gravity and Saffman lift. The latter is directed downward, because the particles in close proximity to the wall are faster than the fluid surrounding them. This also implies that the drag force opposes the particle streamwise motion. The impact velocity is well below the threshold for significant energy restitution, therefore there is effectively no rebound. The lift-off coincides with the particles meeting a fluid ejection, reaffirming the importance of these events in the particle transport. The particles accelerate after leaving the wall, even while they are still faster than the surrounding fluid; this is likely

an effect of added mass and fluid acceleration forces. Future experiments focused on the near-wall region with higher resolution and the ability to detect particle rotation are needed to determine the fluid velocity gradients surrounding the particles and assess the role of lubrication forces and rotation-induced lift.

Different configurations (e.g., particles of different size and density) will display different behaviors. In particular, the particle size is expected to have an important impact on the near-wall behavior, where the velocity gradients are sharper. The present results, however, paint a coherent picture of the multi-faceted problem, shed some new light on a series of long-standing issues, and isolate new questions that require an even deeper investigation. Moreover, inasmuch as we reported novel statistics for several previously undocumented quantities, the results should be useful for developing and validating numerical models.

5.2 Rods and disks

The mean particle velocity and acceleration statistics are largely similar between spherical and non-spherical particles. Disks and rods are both found to oversample high-speed fluid regions near the wall. The particle Reynolds stresses and RMS accelerations differ with particle shape, with the reduced RMS acceleration of disks implying that they have a greater effective inertia or resistance to turbulent fluid motion, and the increased RMS accelerations of the rods implying effectively less inertia. Although the particles have similar nominal Stokes numbers, the difference can be explained by their non-isotropic orientation, because the nominal St^+ are derived for isotropic orientation distributions.

Investigation of the particle orientation reveals that rods tend to align mostly in the streamwise direction, while disks strongly prefer to align their symmetry axis mostly normal to the wall. The near-wall disks also tend to adopt a slightly nose-up configuration. Tumbling is stronger near the wall than in the outer region for both disks and rods, reflecting the strong shear and turbulence in that region. Rods tend to undergo intense tumbling events about the y axis, and disks about the x axis. Both particles also tumble in the spanwise direction, reflecting the sense of the mean shear, but the spanwise tumbling of rods is stronger than that of disks in the near-wall region. Lagrangian autocorrelations of particle orientation confirm that p_y of the disks is coherent for long

time scales, indicating that their preferential wall-normal orientation is very stable. On the other hand, the autocorrelations of rod orientation components decay more quickly, and the decay rate has a strong dependence on wall-normal distance, indicating that shear and turbulence cause the rod orientation to be unstable. Strong tumbling events are found in the set of particles that come in contact with the wall, implicating wall friction as an additional tumbling mechanism.

Rod and disk mean concentration profiles are shown to follow Rouse-Prandtl theory in the range $30 < y^+ < 200$, despite their finite size and inertia. The deviations above and below that range are likely due to a small but non-zero wall-normal particle flux in the outer region and the variation of settling velocity on wall-normal distance. Particle diffusivity is shown to be reasonably well-approximated by the fluid eddy diffusivity, justifying the continued use of that assumption for non-spherical particles, at least for the range of parameters investigated here, i.e. $St^+ \sim O(10)$ and $D_p^+ \sim O(10-100)$.

The present study presents new insights on the behavior and dynamics of inertial, non-spherical particles in a turbulent boundary layer that were previously not measured experimentally. However, additional research effort is warranted to gain a more complete picture of the fluid-particle system. High-resolution PIV studies are needed to measure the detailed fluid velocity fields surrounding the particles, especially near the wall. In addition, the isolated effects of particle size, inertia, and aspect ratio, especially for disk particles, in boundary layer turbulence has yet to be explored experimentally. These unknowns provide several opportunities and motivation for future work.

References

- ADRIAN, R. J. & WESTERWEEL, J. 2011 *Particle image velocimetry*. Cambridge university press.
- ANCEY, C., BÖHM, T., JODEAU, M. & FREY, P. 2006 Statistical description of sediment transport experiments. *Phys. Rev. E* **74** (1), 011302.
- ANCEY, C., DAVISON, A. C., BÖHM, T., JODEAU, M. & FREY, P. 2008 Entrainment and motion of coarse particles in a shallow water stream down a steep slope. *J. Fluid Mech.* **595**, 83–114.
- AYYALASOMAYAJULA, S., GYLFASON, A., COLLINS, L. R., BODENSCHATZ, E. & WARHAFT, Z. 2006 Lagrangian measurements of inertial particle accelerations in grid generated wind tunnel turbulence. *Phys. Rev. Lett.* **97** (14), 144507.
- BAGNOLD, R. A. 1936 The movement of desert sand. *Proc. R. Soc. London, Ser. A* **157** (892), 594–620.
- BAGNOLD, R. A. 1941 *The physics of blown sand and desert dunes*. London: Methuen.
- BALACHANDAR, S., LIU, K. & LAKHOTE, M. 2019 Self-induced velocity correction for improved drag estimation in Euler–Lagrange point-particle simulations. *J. Comput. Phys.* **376**, 160–185.
- BEC, J., BIFERALE, L., BOFFETTA, G., CELANI, A., CENCINI, M., LANOTTE, A., MUSACCHIO, S. & TOSCHI, F. 2006 Acceleration statistics of heavy particles in turbulence. *J. Fluid Mech.* **550**, 349–358.

- BENDAT, J. S. & PIERSOL, A. G. 2011 *Random data: analysis and measurement procedures*, , vol. 729. John Wiley & Sons.
- BERK, T. & COLETTI, F. 2020 Transport of inertial particles in high-Reynolds-number turbulent boundary layers. *J. Fluid Mech.* **903**.
- BERNARDINI, M. 2014 Reynolds number scaling of inertial particle statistics in turbulent channel flows. *J. Fluid Mech.* **758**.
- BERNSTEIN, O. & SHAPIRO, M. 1994 Direct determination of the orientation distribution function of cylindrical particles immersed in laminar and turbulent shear flows. *J. Aerosol Sci.* **25** (1), 113–136.
- BRENNER, H. 1965 Effect of finite boundaries on the Stokes resistance of an arbitrary particle. *J. Fluid Mech.* **12** (1), 35–48.
- BRETHERTON, F. P. 1962 The motion of rigid particles in a shear flow at low Reynolds number. *J. Fluid Mech.* **14** (2), 284–304.
- CAMERON, S. M., NIKORA, V. I. & WITZ, M. J. 2020 Entrainment of sediment particles by very large-scale motions. *J. Fluid Mech.* **888**.
- CAPECELATRO, J. & DESJARDINS, O. 2013 An Euler–Lagrange strategy for simulating particle-laden flows. *J. Comput. Phys.* **238**, 1–31.
- CHALLABOTLA, N. R., ZHAO, L. & ANDERSSON, H. I. 2015 Orientation and rotation of inertial disk particles in wall turbulence. *J. Fluid Mech.* **766**.
- CHOI, J.-I., YEO, K. & LEE, C. 2004 Lagrangian statistics in turbulent channel flow. *Phys. Fluids* **16** (3), 779–793.
- CLIFT, R., GRACE, J. R. & WEBER, M. E. 2005 *Bubbles, drops, and particles*. Minneola, New York: Dover Publications.
- CROWE, C. T., SCHWARZKOPF, J. D., SOMMERFELD, M. & TSUJI, Y. 2011 *Multiphase flows with droplets and particles*. CRC press.
- CSANADY, G. T. 1963 Turbulent diffusion of heavy particles in the atmosphere. *J. Atmos. Sci.* **20** (3), 201–208.

- DE GRAAFF, D. B. & EATON, J. K. 2000 Reynolds-number scaling of the flat-plate turbulent boundary layer. *J. Fluid Mech.* **422**, 319–346.
- DO-QUANG, M., AMBERG, G., BRETHOUWER, G. & JOHANSSON, A. V. 2014 Simulation of finite-size fibers in turbulent channel flows. *Phys. Rev. E* **89** (1), 013006.
- EBRAHIMIAN, M., SANDERS, R. S. & GHAEMI, S. 2019 Dynamics and wall collision of inertial particles in a solid–liquid turbulent channel flow. *J. Fluid Mech.* **881**, 872–905.
- EINSTEIN, H. A. 1950 *The bed-load function for sediment transportation in open channel flows*. US Government Printing Office.
- ELGHOBASHI, S. & TRUESDELL, G. C. 1992 Direct simulation of particle dispersion in a decaying isotropic turbulence. *J. Fluid Mech.* **242**, 655–700.
- ESHGHINEJADFARD, A., HOSSEINI, S. A. & THÉVENIN, D. 2017 Fully-resolved prolate spheroids in turbulent channel flows: a lattice Boltzmann study. *AIP Adv.* **7** (9), 095007.
- FAN, N., SINGH, A., GUALA, M., FOUFOULA-GEORGIU, E. & WU, B. 2016 Exploring a semimechanistic episodic Langevin model for bed load transport: Emergence of normal and anomalous advection and diffusion regimes. *Water Resour. Res.* **52** (4), 2789–2801.
- FONG, K. O., AMILI, O. & COLETTI, F. 2019 Velocity and spatial distribution of inertial particles in a turbulent channel flow. *J. Fluid Mech.* **872**, 367–406.
- GERASHCHENKO, S., SHARP, N. S., NEUSCAMMAN, S. & WARHAFT, Z. 2008 Lagrangian measurements of inertial particle accelerations in a turbulent boundary layer. *J. Fluid Mech.* **617**, 255–281.
- GONDRET, P., LANCE, M. & PETIT, L. 2002 Bouncing motion of spherical particles in fluids. *Phys. Fluids* **14** (2), 643–652.
- GUALA, M., MANES, C., CLIFTON, A. & LEHNING, M. 2008 On the saltation of fresh snow in a wind tunnel: profile characterization and single particle statistics. *J. Geophys. Res. Earth Surf.* **113** (F3).

- GUALTIERI, P., PICANO, F., SARDINA, G. & CASCIOLA, C. M. 2015 Exact regularized point particle method for multiphase flows in the two-way coupling regime. *J. Fluid Mech.* **773**, 520–561.
- HEYMAN, J., BOHORQUEZ, P. & ANCEY, C. 2016 Entrainment, motion, and deposition of coarse particles transported by water over a sloping mobile bed. *J. Geophys. Res. Earth Surf.* **121** (10), 1931–1952.
- HORWITZ, J. A. K. & MANI, A. 2016 Accurate calculation of Stokes drag for point-particle tracking in two-way coupled flows. *J. Comput. Phys.* **318**, 85–109.
- VAN HOUT, R. 2011 Time-resolved PIV measurements of the interaction of polystyrene beads with near-wall-coherent structures in a turbulent channel flow. *Int. J. Multiphase Flow* **37** (4), 346–357.
- VAN HOUT, R. 2013 Spatially and temporally resolved measurements of bead resuspension and saltation in a turbulent water channel flow. *J. Fluid Mech.* **715**, 389.
- VAN HOUT, R., SABBAN, L. & COHEN, A. 2013 The use of high-speed PIV and holographic cinematography in the study of fiber suspension flows. *Acta Mech.* **224** (10), 2263–2280.
- HURTHER, D. & LEMMIN, U. 2003 Turbulent particle flux and momentum flux statistics in suspension flow. *Water Resour. Res.* **39** (5).
- IRELAND, P. J. & DESJARDINS, O. 2017 Improving particle drag predictions in Euler–Lagrange simulations with two-way coupling. *J. Comput. Phys.* **338**, 405–430.
- JEFFERY, G. B. 1922 The motion of ellipsoidal particles immersed in a viscous fluid. *Proc. R. Soc. London, Ser. A* **102** (715), 161–179.
- JOSEPH, G. G., ZENIT, R., HUNT, M. L. & ROSENWINKEL, A. M. 2001 Particle–wall collisions in a viscous fluid. *J. Fluid Mech.* **433**, 329–346.
- JUNG, J., YEO, K. & LEE, C. 2008 Behavior of heavy particles in isotropic turbulence. *Phys. Rev. E* **77** (1), 016307.

- KAFTORI, D., HETSRONI, G. & BANERJEE, S. 1995*a* Particle behavior in the turbulent boundary layer. I. Motion, deposition, and entrainment. *Phys. Fluids* **7** (5), 1095–1106.
- KAFTORI, D., HETSRONI, G. & BANERJEE, S. 1995*b* Particle behavior in the turbulent boundary layer. II. Velocity and distribution profiles. *Phys. Fluids* **7** (5), 1107–1121.
- KIDANEMARIAM, A. G., CHAN-BRAUN, C., DOYCHEV, T. & UHLMANN, M. 2013 Direct numerical simulation of horizontal open channel flow with finite-size, heavy particles at low solid volume fraction. *New J. Phys.* **15** (2), 025031.
- KIGER, K. T. & PAN, C. 2002 Suspension and turbulence modification effects of solid particulates on a horizontal turbulent channel flow. *J. Turbul.* **3** (19), 1–17.
- KOK, J. F., PARTELI, E. J. R., MICHAELS, T. I. & KARAM, D. B. 2012 The physics of wind-blown sand and dust. *Rep. Prog. Phys.* **75** (10), 106901.
- LAJEUNESSE, E., MALVERTI, L. & CHARRU, F. 2010 Bed load transport in turbulent flow at the grain scale: Experiments and modeling. *J. Geophys. Res. Earth Surf.* **115** (F4).
- LAVEZZO, V., SOLDATI, A., GERASHCHENKO, S., WARHAFT, Z. & COLLINS, L. R. 2010 On the role of gravity and shear on inertial particle accelerations in near-wall turbulence. *J. Fluid Mech.* **658**, 229–246.
- LEE, H. & BALACHANDAR, S. 2010 Drag and lift forces on a spherical particle moving on a wall in a shear flow at finite Re. *J. Fluid Mech.* **657**, 89–125.
- LEE, J. & LEE, C. 2015 Modification of particle-laden near-wall turbulence: Effect of Stokes number. *Phys. Fluids* **27** (2), 023303.
- LEE, J. & LEE, C. 2019 The effect of wall-normal gravity on particle-laden near-wall turbulence. *J. Fluid Mech.* **873**, 475–507.
- LI, J., WANG, H., LIU, Z., CHEN, S. & ZHENG, C. 2012 An experimental study on turbulence modification in the near-wall boundary layer of a dilute gas-particle channel flow. *Exp. Fluids* **53** (5), 1385–1403.

- LIN, Z.-W., SHAO, X.-M., YU, Z.-S. & WANG, L.-P. 2017 Effects of finite-size heavy particles on the turbulent flows in a square duct. *J. Hydrodyn.* **29** (2), 272–282.
- MARCHIOLI, C. 2017 Large-eddy simulation of turbulent dispersed flows: a review of modelling approaches. *Acta Mech.* **228** (3), 741–771.
- MARCHIOLI, C., FANTONI, M. & SOLDATI, A. 2010 Orientation, distribution, and deposition of elongated, inertial fibers in turbulent channel flow. *Phys. Fluids* **22** (3), 033301.
- MARCHIOLI, C. & SOLDATI, A. 2002 Mechanisms for particle transfer and segregation in a turbulent boundary layer. *J. Fluid Mech.* **468**, 283–315.
- MARCHIOLI, C., ZHAO, L. & ANDERSSON, H. I. 2016 On the relative rotational motion between rigid fibers and fluid in turbulent channel flow. *Phys. Fluids* **28** (1), 013301.
- MATHAI, V., LOEFFEN, L. A. W. M., CHAN, T. T. K. & WILDEMAN, S. 2019 Dynamics of heavy and buoyant underwater pendulums. *J. Fluid Mech.* **862**, 348–363.
- MAXEY, M. R. & RILEY, J. J. 1983 Equation of motion for a small rigid sphere in a nonuniform flow. *Phys. Fluids* **26** (4), 883–889.
- MORDANT, N., CRAWFORD, A. M. & BODENSCHATZ, E. 2004 Experimental Lagrangian acceleration probability density function measurement. *Physica D* **193** (1-4), 245–251.
- NEMES, A., DASARI, T., HONG, J., GUALA, M. & COLETTI, F. 2017 Snowflakes in the atmospheric surface layer: observation of particle–turbulence dynamics. *J. Fluid Mech.* **814**, 592–613.
- NI, R., KRAMEL, S., OUELLETTE, N. T. & VOTH, G. A. 2015 Measurements of the coupling between the tumbling of rods and the velocity gradient tensor in turbulence. *J. Fluid Mech.* **766**, 202–225.
- NIELSEN, P. 1993 Turbulence effects on the settling of suspended particles. *J. Sediment. Res.* **63** (5), 835–838.

- NIÑO, Y. & GARCIA, M. H. 1996 Experiments on particle–turbulence interactions in the near-wall region of an open channel flow: implications for sediment transport. *J. Fluid Mech.* **326**, 285–319.
- NISHIMURA, K. & HUNT, J. C. R. 2000 Saltation and incipient suspension above a flat particle bed below a turbulent boundary layer. *J. Fluid Mech.* **417**, 77–102.
- NJOBUNWU, D. O. & FAIRWEATHER, M. 2016 Simulation of inertial fibre orientation in turbulent flow. *Phys. Fluids* **28** (6), 063307.
- OUCHENE, R., POLANCO, J. I., VINKOVIC, I. & SIMOËNS, S. 2018 Acceleration statistics of prolate spheroidal particles in turbulent channel flow. *J. Turbulence* **19** (10), 827–848.
- PAPANICOLAOU, A. N., DIPLAS, P., EVAGGELOPOULOS, N. & FOTOPOULOS, S. 2002 Stochastic incipient motion criterion for spheres under various bed packing conditions. *J. Hydraul. Eng.* **128** (4), 369–380.
- PETERSEN, A. J., BAKER, L. & COLETTI, F. 2019 Experimental study of inertial particles clustering and settling in homogeneous turbulence. *J. Fluid Mech.* **864**, 925–970.
- PICANO, F., BREUGEM, W.-P. & BRANDT, L. 2015 Turbulent channel flow of dense suspensions of neutrally buoyant spheres. *J. Fluid Mech.* **764**, 463–487.
- POPE, S. B. 2000 *Turbulent Flows*. Cambridge, UK: Cambridge Univ. Press.
- PRANDTL, L. 1952 Essentials of fluid dynamics with applications to hydraulics, aeronautics, meteorology and other subjects .
- RABENCOV, B., ARCA, J. & VAN HOUT, R. 2014 Measurement of polystyrene beads suspended in a turbulent square channel flow: Spatial distributions of velocity and number density. *Int. J. Multiphase Flow* **62**, 110–122.
- REEKS, M. W. 1977 On the dispersion of small particles suspended in an isotropic turbulent fluid. *J. Fluid Mech.* **83** (3), 529–546.

- RICHTER, D. H. & SULLIVAN, P. P. 2014 Modification of near-wall coherent structures by inertial particles. *Phys. Fluids* **26** (10), 103304.
- RIGHETTI, M. & ROMANO, G. P. 2004 Particle–fluid interactions in a plane near-wall turbulent flow. *J. Fluid Mech.* **505**, 93–121.
- RIMON, Y. & CHENG, S. I. 1969 Numerical solution of a uniform flow over a sphere at intermediate Reynolds numbers. *Phys. Fluids* **12** (5), 949–959.
- ROBINSON, S. K. 1991 Coherent motions in the turbulent boundary layer. *Annu. Rev. Fluid Mech.* **23** (1), 601–639.
- ROUSE, H. 1937 Modern conceptions of the mechanics of fluid turbulence. *Trans. Am. Soc. Civ. Eng.* **102**, 463–505.
- ROUSON, D. W. I. & EATON, J. K. 2001 On the preferential concentration of solid particles in turbulent channel flow. *Journal of Fluid Mechanics* **428**, 149–169.
- SABBAN, L. & VAN HOUT, R. 2011 Measurements of pollen grain dispersal in still air and stationary, near homogeneous, isotropic turbulence. *J. Aerosol Sci.* **42** (12), 867–882.
- SAFFMAN, P. G. T. 1965 The lift on a small sphere in a slow shear flow. *J. Fluid Mech.* **22** (2), 385–400.
- SARDINA, G., SCHLATTER, P., BRANDT, L., PICANO, F. & CASCIOLA, C. M. 2012 Wall accumulation and spatial localization in particle-laden wall flows. *J. Fluid Mech.* **699**, 50–78.
- SHAIK, S., KUPERMAN, S., RINSKY, V. & VAN HOUT, R. 2020 Measurements of length effects on the dynamics of rigid fibers in a turbulent channel flow. *Phys. Rev. Fluids* **5** (11), 114309.
- SHAPIRO, M. & GOLDENBERG, M. 1993 Deposition of glass fiber particles from turbulent air flow in a pipe. *J. Aerosol Sci.* **24** (1), 65–87.
- SHIELDS, A. 1936 Anwendung der Aehnlichkeitsmechanik und der Turbulenzforschung auf die Geschiebebewegung. PhD thesis, Technical University Berlin.

- SMITS, A. J., MCKEON, B. J. & MARUSIC, I. 2011 High-Reynolds number wall turbulence. *Annu. Rev. Fluid Mech.* **43**.
- SQUIRES, K. D. & EATON, J. K. 1991 Measurements of particle dispersion obtained from direct numerical simulations of isotropic turbulence. *J. Fluid Mech.* **226**, 1–35.
- TANIÈRE, ANNE & ARCEN, BORIS 2016 Overview of existing Langevin models formalism for heavy particle dispersion in a turbulent channel flow. *Int. J. Multiphase Flow* **82**, 106–118.
- TANIÈRE, A., OESTERLÉ, B. & MONNIER, J. C. 1997 On the behaviour of solid particles in a horizontal boundary layer with turbulence and saltation effects. *Exp. Fluids* **23** (6), 463–471.
- TAYLOR, G. I. 1921 Diffusion by continuous movements. *Proc. Lond. Math. Soc.* **s2-20** (1), 196–212.
- TAYLOR, G. I. 1923 Experiments on the motion of solid bodies in rotating fluids. *Proc. R. Soc. London, Ser. A* **104** (725), 213–218.
- TEE, Y. H., BARROS, D. & LONGMIRE, E. K. 2020 Motion of finite-size spheres released in a turbulent boundary layer. *Int. J. Multiphase Flow* **133**, 103462.
- VOTH, G. A., LA PORTA, A., CRAWFORD, A. M., ALEXANDER, J. & BODENSCHATZ, E. 2002 Measurement of particle accelerations in fully developed turbulence. *J. Fluid Mech.* **469**, 121–160.
- VOTH, G. A. & SOLDATI, A. 2017 Anisotropic particles in turbulence. *Annu. Rev. Fluid Mech.* **49**, 249–276.
- WANG, G., ABBAS, M. & CLIMENT, É 2017 Modulation of large-scale structures by neutrally buoyant and inertial finite-size particles in turbulent Couette flow. *Phys. Rev. Fluids* **2** (8), 084302.
- WANG, G., ABBAS, M., YU, Z., PEDRONO, A. & CLIMENT, E. 2018 Transport of finite-size particles in a turbulent Couette flow: The effect of particle shape and inertia. *Int. J. Multiphase Flow* **107**, 168–181.

- WANG, G., FONG, K. O., COLETTI, F., CAPECELATRO, J. & RICHTER, D. H. 2019 Inertial particle velocity and distribution in vertical turbulent channel flow: a numerical and experimental comparison. *Int. J. Multiphase Flow* **120**, 103105.
- WANG, L.-P. & MAXEY, M. R. 1993 Settling velocity and concentration distribution of heavy particles in homogeneous isotropic turbulence. *J. Fluid Mech.* **256**, 27–68.
- WANG, L.-P. & STOCK, D. E. 1993 Dispersion of heavy particles by turbulent motion. *J. Atmos. Sci.* **50** (13), 1897–1913.
- WELLS, M. R. & STOCK, D. E. 1983 The effects of crossing trajectories on the dispersion of particles in a turbulent flow. *J. Fluid Mech.* **136**, 31–62.
- WESTERWEEL, J. & SCARANO, F. 2005 Universal outlier detection for PIV data. *Exp. Fluids* **39**, 1096–1100.
- YUAN, W., ANDERSSON, H. I., ZHAO, L., CHALLABOTLA, N. R. & DENG, J. 2017 Dynamics of disk-like particles in turbulent vertical channel flow. *Int. J. Multiphase Flow* **96**, 86–100.
- YUAN, W., ZHAO, L., ANDERSSON, H. I. & DENG, J. 2018a Three-dimensional Voronoï analysis of preferential concentration of spheroidal particles in wall turbulence. *Phys. Fluids* **30** (6), 063304.
- YUAN, W., ZHAO, L., CHALLABOTLA, N. R., ANDERSSON, H. I. & DENG, J. 2018b On wall-normal motions of inertial spheroids in vertical turbulent channel flows. *Acta Mech.* **229** (7), 2947–2965.
- ZAMANSKY, R., VINKOVIC, I. & GOROKHOVSKI, M. 2011 Acceleration statistics of solid particles in turbulent channel flow. *Phys. Fluids* **23** (11), 113304.
- ZHANG, H., AHMADI, G., FAN, F.-G. & MCLAUGHLIN, J. B. 2001 Ellipsoidal particles transport and deposition in turbulent channel flows. *Int. J. Multiphase Flow* **27** (6), 971–1009.
- ZHAO, L., CHALLABOTLA, N. R., ANDERSSON, H. I. & VARIANO, E. A. 2015 Rotation of nonspherical particles in turbulent channel flow. *Phys. Rev. Lett.* **115** (24), 244501.

- ZHAO, L., CHALLABOTLA, N. R., ANDERSSON, H. I. & VARIANO, E. A. 2019 Mapping spheroid rotation modes in turbulent channel flow: effects of shear, turbulence and particle inertia. *J. Fluid Mech.* **876**, 19–54.
- ZHAO, L. H., ANDERSSON, H. I. & GILLISSEN, J. J. J. 2010 Turbulence modulation and drag reduction by spherical particles. *Phys. Fluids* **22** (8), 081702.
- ZHU, H.-Y., PAN, C., WANG, J.-J., LIANG, Y.-R. & JI, X.-C. 2019 Sand-turbulence interaction in a high-Reynolds-number turbulent boundary layer under net sedimentation conditions. *Int. J. Multiphase Flow* **119**, 56–71.